2017-08-11

Towards Bio-Inspired Cementitious Materials: The Effect of Organic Polymeric Materials on the Nanostructure and Nanomechanical Properties of Calcium-Silicate-Hydrate

Mahsa Kamali
University of Miami, mahsa1991kamali@gmail.com

Follow this and additional works at: https://scholarlyrepository.miami.edu/oa_dissertations

UNIVERSITY OF MIAMI

TOWARDS BIO-INSPIRED CEMENTITIOUS MATERIALS: THE EFFECT OF ORGANIC POLYMERIC MATERIALS ON THE NANOSTRUCTURE AND NANOMECHANICAL PROPERTIES OF CALCIUM-SILICATE-HYDRATE

By

Mahsa Kamali

A DISSERTATION

Submitted to the Faculty
of the University of Miami
in partial fulfillment of the requirements for
the degree of Doctor of Philosophy

Coral Gables, Florida

August 2017

UNIVERSITY OF MIAMI

A dissertation submitted in partial fulfillment of
the requirements for the degree of
Doctor of Philosophy

TOWARDS BIO-INSPIRED CEMENTITIOUS MATERIALS:
THE EFFECT OF ORGANIC POLYMERIC MATERIALS ON THE
NANOSTRUCTURE AND NANOMECHANICAL PROPERTIES
OF CALCIUM-SILICATE-HYDRATE

Mahsa Kamali

Approved:

_____
Ali Ghahremaninezhad, Ph.D.
Assistant Professor of Civil Engineering

_____
James Giancaspro, Ph.D.
Associate Professor of Civil Engineering

_____
Antonio Nanni, Ph.D.
Professor of Civil Engineering

_____
Qingda Yang, Ph.D.
Associate Professor of Mechanical
Engineering

_____
Edward A. Dauer, M.D.
Research Associate Professor of
Biomedical Engineering

_____
Guillermo Prado, Ph.D.
Dean of the Graduate School

KAMALI, MAHSA   (Ph.D., Civil Engineering)
<u>Towards Bio-Inspired Cementitious Materials:</u>   (August 2017)
<u>The Effect of Organic Polymeric Materials on the Nanostructure</u>
<u>and Nanomechanical Properties of Calcium-Silicate-Hydrate</u>

Abstract of a dissertation at the University of Miami.

Dissertation supervised by Dr. Ali Ghahremaninezhad.
No. of pages in text. (119)

This study aims to obtain a fundamental understanding of the effect of polymeric materials with distinct functional groups on the nanostructure and nanomechanical response of calcium-silicate-hydrate (C-S-H). Nature has created biological materials with hierarchical microstructure and superior mechanical and functional properties. This is achieved in nature through certain biopolymers with specific structures and functionalities directing growth, microstructure and macroscopic performance of biological materials. C-S-H comprises the primary component of the cement hydration product and plays a fundamental role in determining the mechanical and long-term characteristics of cement-based materials. The different size and molecular structure of polymers, and the complex structure and chemical functionalities of biopolymers permit a wide range of interactions including electrostatic, hydrogen bonding and hydrophobic with C-S-H. The ability to modify the characteristics of C-S-H through a specific combination of interactions with biopolymers permits a pathway to manipulate the structure, and the physical and mechanical properties of C-S-H. The primary contribution of this study is to explore a bio-inspired approach as a new paradigm in controlling microstructure design to achieve

desired properties in infrastructure materials. In pursuit of the objectives of this study, this dissertation aims to obtain a fundamental understanding of the interaction of polymers and biopolymers with C-S-H, to discover the effect of polymers and biopolymers on the atomic structure and morphology of C-S-H, and to elucidate how polymers and biopolymers affect the Young's modulus of C-S-H. This study shows that C-S-H can be used in biomimetic nanocomposites made of inorganic and organic compounds. For the first time a C-S-H/polymer nanocomposite with the aim of investigating the mechanical properties was fabricated using the layer-by-layer (LBL) technique. Because of the presence of inorganic compounds in the structure of the C-S-H/polymer nanocomposite, it has the potential to exhibit much more flexibility than pure C-S-H which is highly desired in construction materials. The outcome of this study can be seen as a first step towards the formation of bio-inspired construction materials.

Acknowledgment

I would like to thank my dissertation advisor Dr. Ghahremaninezhad for his academic guidance. He was with me at every phase of the learning process, patiently watching over my progress. The door to his office was always open whenever I had a question about my research. I would also like to thank the members of my doctoral committee for their advice on my dissertation.

The XRD experiments were carried out in the Advanced Materials Engineering Research Institute (AMERI) at Florida International University. The FTIR experiments were performed in the Chemistry Department at University of Miami. Patricia Blackwelder is acknowledged for taking the SEM images.

I would like to thank my lab mates Khashayar Farzanian and Jessica Flores for their assistance and support throughout the past years.

I must express my very profound gratitude to my parents and my friends, Maryam and Donia for their unfailing emotional support. This accomplishment would not have been possible without them.

Table of Content

List of Figures

List of Tables

Chapter 1

1. Introduction

Concrete is the most widely used infrastructure material and its production is expected to increase at a rate of 5% annually [1]. Concrete is traditionally made of aggregates, cement and water. Portland cement was invented in 1824 by Joseph Aspdin and since then it started to be widely used in concrete construction materials. Reinforcing with reinforcing-bars (re-bars), and introducing chemical admixtures to the concrete are the two great breakthroughs in the history of concrete after the invention of Portland cement. Concrete is the only building material that in the journey of its development in the twentieth century, not only transformed the lives of human beings, but also represented the needs of society for change [2]. Now, more than ever, we need to make a difference in the way that we treat the environment. Taking immediate action to manage environmental resources is necessary in order to build a future that ensures both human progress and human survival [3]. The term "sustainable development" was defined to help to address the global challenge of building the future of the earth, which is the future of human beings. Sustainable development is defined as meeting the needs of the present without compromising the ability of future generations to meet their own needs [3]. The concept of sustainability is incorporated in different aspects of development. In the area of construction, increased demand makes it necessary to look for sustainable solutions for the future of the construction industry [4]. As developments in concrete have always represented the needs of society [2], it is not surprising to see the footprints of sustainability in the concrete industry. Among the numerous paths to achieve sustainability, because it provides a different perspective, nanotechnology is gaining increased attention [5–10]. In

concrete, nanotechnology is used to develop innovative approaches to manipulate the structure of cementitious materials at the nano to microscale as a way to improve the macroscale properties [11–19]. Improving the mechanical and durability performance of concrete is a way to increase sustainability in infrastructure [20,21]. Cement acts as a binder in concrete, and controls its mechanical properties. At a smaller scale, calcium silicate hydrate (C-S-H) is the primary product of cement hydration and provides the binding strength; thus, it plays a crucial role in the mechanical properties and durability of concrete [22–25]. Modifications on the microstructure of cementitious materials affect the nucleation and structure of C-S-H. Researchers have employed several strategies to modify the microstructure of cementitious materials. The incorporation of nanoparticles [20,26–29] and the introduction of polymeric additives to cementitious materials [14,30,31] are two different approaches of particular interest.

Figure 1.1 The oldest concrete street in America built in 1891 by George Bartholomew in Bellefontaine, Ohio (Image from www.trover.com).

1.1. Objectives

The objective of this study is to explore the effect of polymers and biomolecules on the microstructure and nanomechanical properties of C-S-H. The fundamental findings of this study can set the stage for an innovative approach to engineer modern infrastructure materials. In pursuit of the objective of this study, this dissertation aimed:

- To obtain a fundamental understanding of the interaction between organic compounds with different functional groups and C-S-H.

- To explore the effect of the interactions between the organic compounds and C-S-H on the atomic structure and morphology of C-S-H.

- To elucidate how the microstructural modification of C-S-H with organic compounds influences its nanomechanical properties.

- To fabricate C-S-H/polymer nanocomposites using the layer-by-layer technique and investigate their morphology, and measure their elastic modulus using nanoindentation.

1.2. Structure of C-S-H

The heterogeneity in the microstructure of concrete ranging from macroscale to nanoscale is shown in Figure 1.2. At the macroscale, concrete consists of aggregates, macropores, and a cement paste binder (Figure 1.2a). At the microscale, the cement paste binder is a multiphase system consisting of unhydrated cement, capillary pores and hydrated cement primarily made of calcium-silicate-hydrate (C-S-H) and calcium hydroxide ($Ca(OH)_2$) (Figure 1.2b). At the mesoscale, the C-S-H composite is comprised of disordered stacks of up to ten or even hundreds of nanolayers, and pores, referred to as

gel pores [23,32,33] (Figure 1.2c and Figure 1.2d). There are several studies on the stoichiometry of C-S-H, suggesting various models to describe its chemical structure [25,34,35]. However, it is generally acknowledged that C-S-H in hydrated cement systems does not have a specific chemical formula and its stoichiometry varies in a range of calcium to silicate ratio (C/S ratio) of 0.6 to 2.3. In low C/S ratios, each C-S-H nanolayer is composed of a CaO sheet sandwiched between silicate chains. Ideally the repeating unit of the silicate chain consists of three silicate tetrahedra, two facing the CaO sheet (pairing tetrahedra), and one facing the interlayer region (bridging tetrahedron). This type of structure is similar to that of a natural mineral called tobermorite; however, in the structure of C-S-H some of the bridging tetrahedra are missing (Figure 1.2e).
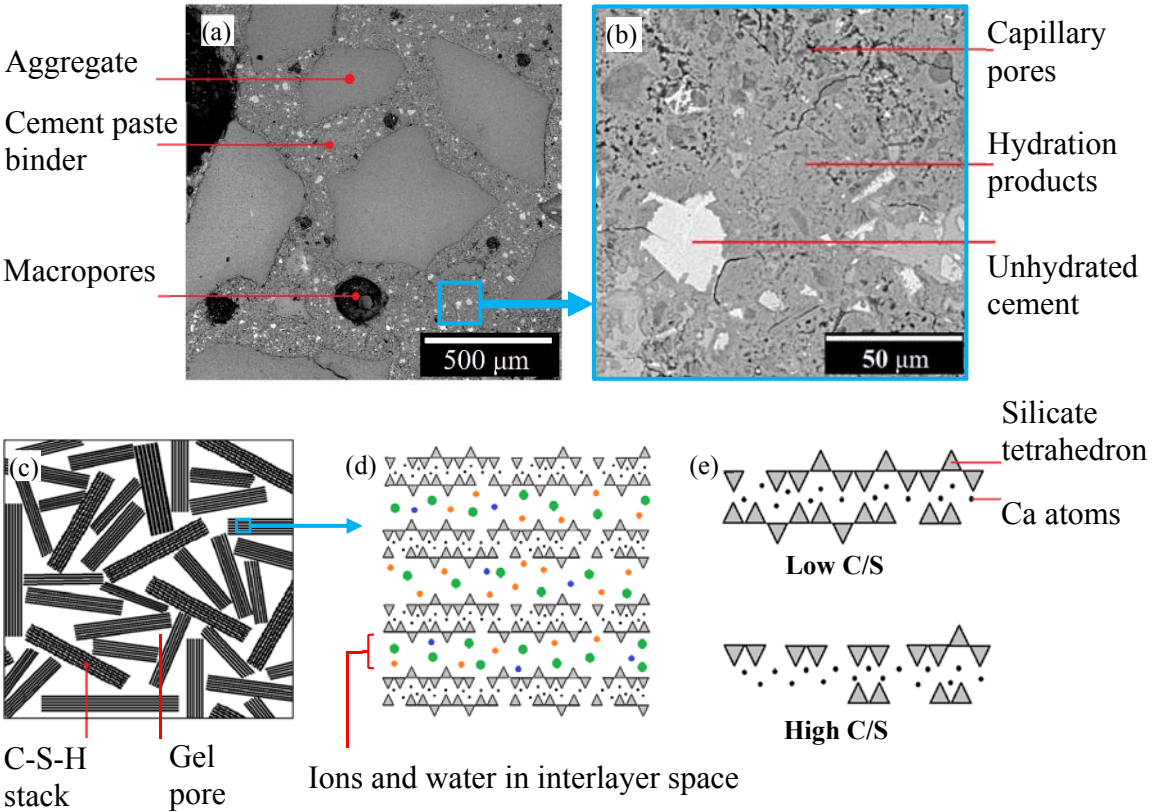
Figure 1.2 Heterogeneity in the structure of concrete from macro scale to nano scale.

1.3. Microstructural Modifications Using Polymers

In nature, certain nanocomposites with superior mechanical properties, such as nacre, are composed of inorganic pellets bound together with an organic glue, forming a layer-by-layer structure. The lamellar microstructure of nacre is shown in Figure 1.3. The inorganic aragonite (a crystallographic form of calcium carbonate) pellets are glued together by proteins and polysaccharides in a brick-and-mortar structure [36]. The hierarchical microstructure of nacre - consisting of 95% hard aragonite and 5% organic compound – is responsible for enhanced mechanical properties achieving a fracture toughness value of 3 to 9 times higher than that of aragonite [36].
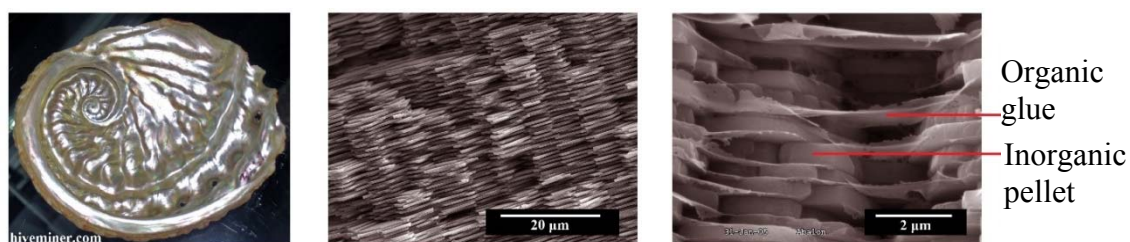
Figure 1.3 The lamellar microstructure of nacre (images from hiveminer.com).

The idea of modifying C-S-H nanoparticles with polymers is inspired by the structure of nacre and other biological nanocomposites in order to learn from millions of years of evolution and achieve new perspectives to design new materials with superior engineering properties [37]. As for the first step, a deep understanding of the different mechanisms by which polymers interact with C-S-H is necessary. Several interaction mechanisms have been suggested among which surface adsorption and intercalation are the most common ones [16]. These two mechanisms are depicted in Figure 1.4. In surface absorption, the polymer is grafted at the surface of the C-S-H stack. This mechanism does not change the

structure of C-S-H. The adsorbed polymer decreases the packing density of the system and consequently, affects its mechanical properties [15]. In intercalation, however, polymers intercalate into the interlayer space of C-S-H layers and increase the interlayer distance. Intercalation is expected to affect the mechanical properties of the C-S-H system. As suggested by previous studies, the interaction mechanism between C-S-H and polymers depends on both C-S-H stoichiometry and polymer structure [11,13,38]. The C/S ratio of C-S-H, the functional groups present in the structure of polymer, and the conformation of the polymer molecule and its molecular weight, are determining factors that need to be investigated.
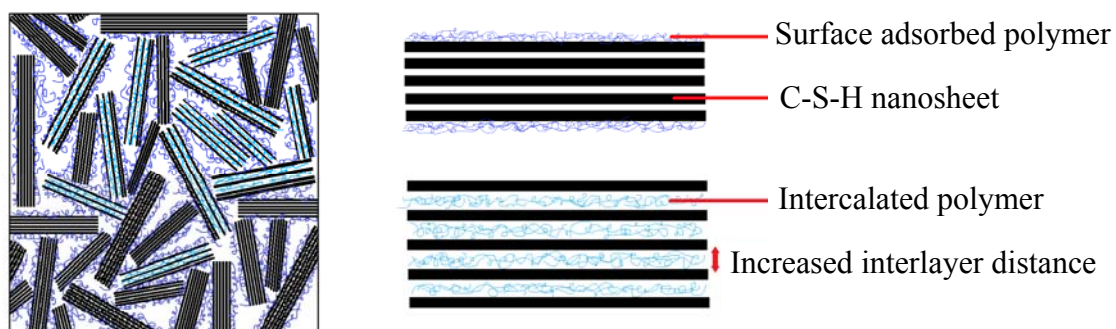
Figure 1.4 Different mechanisms of interaction between polymers and C-S-H nanoparticles.

Polymers, both synthetic and natural, are composed of repeated molecules with different structures. The variation in the number and chemical structure of the monomers provides polymers with a broad range of physical and chemical properties that make them suitable for a variety of applications [39]. The functional groups in the structure of polymers determine the way they interact with inorganic materials. These functional groups are classified into three categories: charged, polar, and non-polar. The nature of interaction between charged functional groups and inorganic materials is electrostatic.

Polymers with polarized functional groups are capable of forming secondary bonds with inorganic solids. These secondary bonds are stronger when the functional group is N-H or O-H and are called hydrogen bonds. The intermolecular bonds in polymers with non-polar functional groups are extremely weak and limited to occasional polarity due to valence electrons movements [40]. These polymers are generally hydrophobic.

Block copolymers are a class of polymers where two or more different blocks of monomers unite together in a linear and/ or radial order to form the polymer molecule. Copolymers can have any of the charged, hydrogen bonding and hydrophobic functional groups in their structure which provide them with an ability to interact with various types of materials. Amphiphilic copolymers possess both hydrophilic and hydrophobic properties and have the ability to be used as surfactants. This makes them a good candidate as a structural-directing agent for synthesis of inorganic structures where a high level of control on the shape and size of the particles is desired [41–44] . The self-assembly of the block copolymers both in bulk and in solution has been the focus of many studies [45–47]. Block copolymers can aggregate into various complex and hierarchical structures and morphologies including spheres, hexagonally packed cylinders, lamellae and etc. [45,48]. When the concentration of the amphiphilic block copolymers in the solvent is higher than a critical concentration – called the critical micellization concentration (CMC) – the block copolymers undergo a micellization process in which the polymer chains assemble themselves in the form of micelles, vesicles or cylinders [48,49]. A schematic of micelle formation in amphiphilic block copolymers is shown in Figure 1.5.
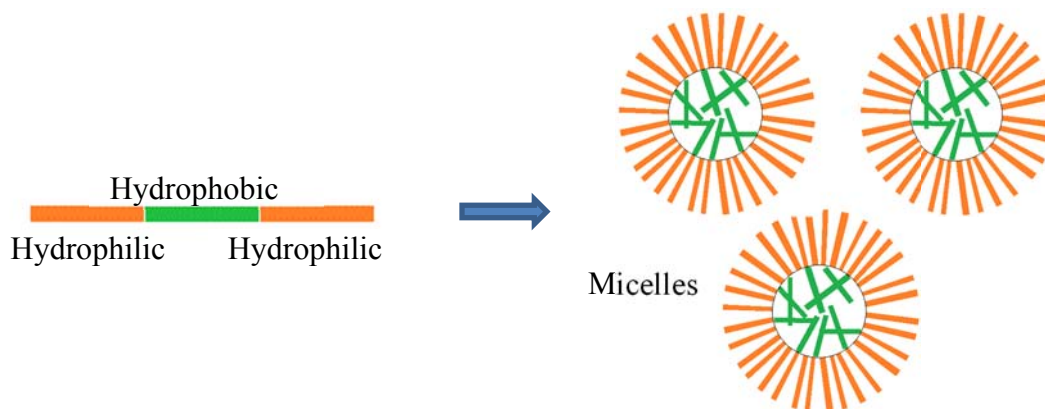
Figure 1.5 Schematic of micellization in amphiphilic block copolymers.

The addition of polymeric additives to cementitious materials can affect their microstructure and can influence their physical and chemical properties by changing the interfaces and surface chemistry of cement particles during the hydration process [31,50,51]. The use of organic materials to modify the microstructure of cementitious materials can also be studied in the concept of organic/inorganic nanocomposites. This approach is inspired by the microstructure of biomaterials. Certain biological nanocomposites, such as bones, teeth, nacre of abalone shells, exhibit superior mechanical and physical performance unmatched by engineering materials [11,15,17,19,52,53]. Inspired by nature, there have been intense research efforts to understand the underlying mechanisms for high mechanical and physical properties of biological nanocomposites. A major goal of these studies is to enable synthesis of materials with improved mechanical and functional properties exceeding those of the traditional materials. It has been shown that the high mechanical performance of bio-composites is attributed to the interaction between organic and inorganic materials governing their microstructure [52,54–56]. The intricate microstructure of certain bio-composites achieved when inorganic reinforcements are glued together by an organic polymeric compound results in a combination of high

strength and high toughness for bio-composites [52]. Verho et al. [55] produced a bio-inspired nanocomposite of nanoclay and poly(vinyl alcohol) and investigated its mechanical response in different humidity levels. Wang et al. [57,58] reported an improvement in mechanical properties of a polymer matrix when it was reinforced with nanolayered silicate clays to form nanocomposites with intercalated or exfoliated structures. Rodríguez Hernández et al. [59] used nanosilica with different weight percentages in a polymer matrix and reported an improvement in the stiffness value of the matrix. In cementitious materials, the incorporation of polymers as an organic compound is promising because it has the potential to enhance the mechanical performance of C-S-H. However, there has been differences of opinion over the feasibility of intercalating the polymers between the C-S-H stacks. Matsuyama et al. [11–13] were the first to investigate the possibility of intercalation of polymers with different charges into the structure of C-S-H with various calcium to silicate ratios. Although they did not report a successful intercalation of small sized polymer molecules, they claimed that polymers with higher molecular size can intercalate between the C-S-H layers. Based on their findings, the intercalation of cationic polymers between C-S-H layers are more favorable at low C/S ratios. However, anionic polymers are more likely to intercalate at high C/S ratios. They also reported a possible intercalation of non-ionic poly(vinyl alcohol) which was related to the interaction of the polymer with C-S-H, facilitated though the partial ionization of the polymer molecule at the high pH of the synthesis. Merlin et al. [17] claimed that the intercalation of the polymer between the C-S-H stacks is hard to achieve. They did not have any success in intercalation of polymers into C-S-H structure by pozzolanic reaction method or precipitation method. However, they reported the interaction of polymers with

the C-S-H stacks which facilitated the adsorption of the polymer onto the surface of the stacks or in the void space between the stacks. According to Popova et al. [30] large amount of polymers can be adsorbed onto the C-S-H particles. However, the adsorbed polymer does not change the structure of C-S-H through intercalation. Pelisser et al. [19] claimed that a lower molecular weight poly(vinyl alcohol) has the potential to intercalate between the C-S-H layers. In another study, Pelisser at al. [15] investigated the interaction of poly(diallyldimethylammonium chloride) with C-S-H. According to their findings, at C/S of 0.8, some poly(diallyldimethylammonium chloride) intercalated between the C-S-H layers. However, the rest of the polymer was adsorbed on the surface of C-S-H and decreased the elastic modulus and hardness of the C-S-H complex by decreasing its packing density. Alizadeh et al. [16] synthesized C-S-H with aniline and then polymerized the monomer to achieve C-S-H/polyaniline nanostructures. They reported a potential increase in the silicate polymerization at various C/S levels in polyaniline modified C-S-H. Khoshnazar et al. [18] investigated the effect of low molecular size nitrobenzoic acid on the structure of C-S-H and reported a possible intercalation at a low polymer concentration. Minet at al. [60] showed that small molecular sized organic molecules are able to intercalate between the C-S-H layers without changing the structural framework of C-S-H. However, phase separation occurred for the C-S-H/polymer complexes when the polymer molecule was large in size or highly hydrophobic. In another study [61], they reported a successful synthesis of C-S-H with polymers directly bonded to its structure via covalent bonds.

1.4. Microstructural Modifications Using Biomolecules

Biomolecules are the organic compound in certain biological nanocomposites that exhibit enhanced engineering properties and therefore they can be used as promising compounds to modify the microstructure of bio-inspired materials. The ability to achieve biomaterials with superior mechanical properties in nature is facilitated by the interactions between biopolymers, such as amino acids and their polymers, and inorganic materials [53,62]. Nature has mastered biopolymer sequencing to provide complex interactions between biopolymers and inorganic materials; it is this complexity in the structure and functionality of biopolymers that controls biomineralization in a specific direction.

Amino acids are natural compounds that contain both amine and carboxyl functional groups as well as a side chain (except glycine) that is unique for each amino acid. The structure of amino acids is shown in Figure 1.6. Amino acids based on the functional group of their side chain are classified into three different categories: charged, polar (hydrogen bonding) and non-polar (hydrophobic) [63,64]. A chain of amino acids are joined together to form peptides through peptide bonds. Peptide bonds are covalent bonds formed by the reaction between the amino group of one amino acid and the carboxylic group of another amino acid. Peptides are the building block of proteins [65].
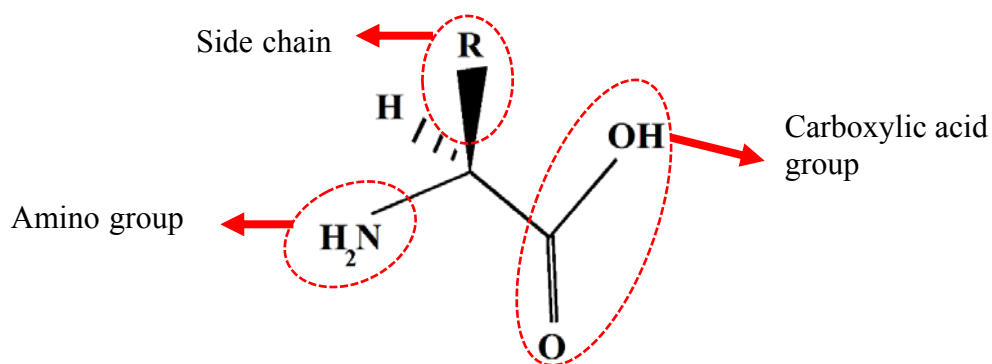
Figure 1.6 The structure of amino acids.

Picker et al. [66] performed phage display on C-S-H samples with different calcium to silicate ratios and pH levels providing various interacting surface properties to shed light on the possible interactions occurring between the C-S-H and peptides in the multi-component system of cement during the hydration. Phage display is a screening technique to study proteins and other macromolecules. In this method large random sequences of peptides or proteins are expressed to a chosen surface. Libraries of a large number of members are studied to specify the sequences that strongly bind to the surface [67]. The outcomes of their study [66] revealed the role of hydrophobic functional groups of biomolecules in interaction with C-S-H. They showed that an organic additive should contain all three charged, H-donating and hydrophobic functional groups to adsorb strongly onto C-S-H. This suggests that proteins with their ability to interact with other molecules through different functional groups can be considered a promising organic compound to manipulate the properties of C-S-H/polymer systems.

1.5. Microstructural Modifications Using Nanomaterials

Nanomaterials have the potential to revolutionize the construction industry by enhancing the performance of construction materials and introducing new properties to construction materials [26–29]. Some of the applications of nanotechnology in cementitious materials are listed as follows [68]:

- Improving the mechanical properties through microstructural densification, enhancing the cement hydration, improving the aggregate-paste bonding strength, self-healing of micro-cracks, and developing stress-sensing properties in concrete.

- Enhancing the durability properties by reducing the permeability and improving the shrinkage properties.

- Developing sustainable and safe concrete materials such as self-cleaning concrete and sustainable cement.

The addition of nanomaterials with high surface/volume ratios to cementitious materials improves their microstructural characteristics, and as a result, their performance and durability properties [20]. Nanoparticles improve the performance of cementitious materials through various mechanisms. One mechanism is that the uniformly dispersed nanoparticles in the cement paste provide nucleation sites for deposition of cement hydration products. Thus the incorporation of nanoparticles in the cementitious matrix improves and accelerates the cement hydration process [68–70]. Some nanoparticles such as carbon nanofibers and carbon nanotubes with a high aspect ratio can uniformly disperse in the cement mixture and interrupt the microcracks during the propagation with a bridging mechanism [71]. Another mechanism is that the nanoparticles with pozzolanic properties react with calcium hydroxide and produce more C-S-H [68,72–74]. Researchers have previously studied the use of silica nanoparticles [75–77], carbon nanotubes [71,78–80], TiO_2 nanoparticles [81–87], and clay nanoparticles [88–91] in cementitious materials. Lackhoff et al. [81], Lee et al. [85] and Zhang et al. [86] reported an increase in the compressive strength of cementitious materials containing TiO_2. Graphene oxide (GO) nano platelets which have a sheet-like structure and obtain functional groups during the oxidation process are also a promising additive for cementitious materials and polymers [20]. Previous studies have shown that the use of GO nanosheets can improve the mechanical properties of cement paste at macroscale by modifying the formation and regulating the microstructure of C-S-H [92–94].

1.6. Layer by Layer Assembly

Layer-by-Layer (LBL) assembly is a widely used "bottom-up" nanofabrication technique that has applications in fabrication of various types of coatings and free standing thin films and hierarchical nanostructures [95–100]. Bottom-up nanofabrication is a novel manufacturing strategy in which the component molecules are self-assembled to build the desired nanostructure [101]. LBL assembly technique allows different types of polymers and nanoparticles to be incorporated in the structure of thin films through electrostatic and other interaction [102]. The mechanism of LBL assembly is depicted in Figure 1.7. In this technique, the thickness of the layers can be highly controlled, and this facilitates tailoring the structure of composites at a small scale. The continuous assembly of the layers facilitated through the charge reversion after the deposition of each layer, makes it possible to fabricate thin films with desired number of layers [101]. LBL has numerous applications in the design of light-emitting diodes [103,104], non-linear optics [105], metal composites [106,107], biomedical microcapsules [108,109] and tissue engineering [110,111]. Inorganic materials such as colloidal particles, graphene oxide [112] and nanoclay have been successfully incorporated in LBL fabricated thin films.
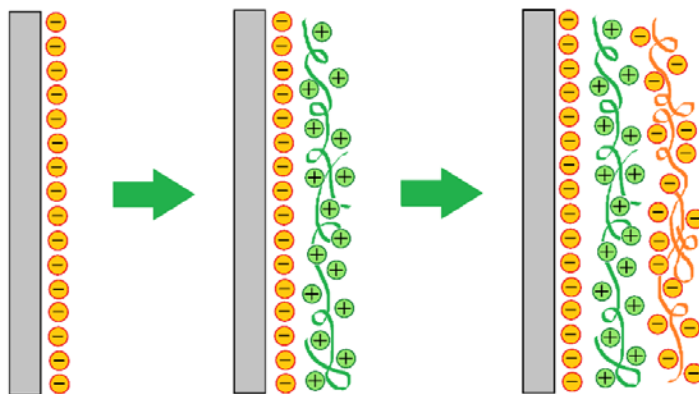
Figure 1.7 Fabrication of thin film using layer by layer assembly.

Guo et al. [98,99] used C-S-H as the inorganic unit in LBL assemblies to fabricate super-hydrophilic and antireflective coatings. Two polymer/ion complexes, one with calcium ions and one with silicate ions, were deposited layer by layer on a substrate. Precipitation of C-S-H between the layers was provided through the reaction of calcium and silicate ions.

Due to the ability of the LBL method to produce nanocomposites with a nanoscale control, this technique is useful in the fundamental study of C-S-H/polymer nanocomposites. This technique permits to investigate the effect of various relevant parameters including the polymer molecular structure and charge, C-S-H composition, pH, and others on the microstructure and mechanical properties of C-S-H/polymer nanocomposites at the nanoscale. In addition, since the surface characteristics including surface roughness of C-S-H/polymer nanocomposite can be tuned to achieve a very low roughness suitable for nanoindentation, the LBL technique can provide an alternative approach to fabricating samples for use in nanomechanical characterization of this kind of nanocomposites.

1.7. Chapters Overview

In chapter 2 of this dissertation, a detailed description of the experimental methods used for characterizing the structure, investigating the morphology, and elucidating the mechanical properties of the composites is provided. Different materials used in this study including polymers, copolymers and biomolecules, are introduced, and sample preparation procedures for different test methods are described in this chapter.

In order to investigate the feasibility of using copolymers with distinct functional groups to manipulate the structure and mechanical performance of cementitious systems, Chapter 3 examines the composition-structure-property relations of C-S-H/polymers and C-S-H/copolymers systems. In this chapter, polymers with different charges and copolymers, with various structures, molecular sizes and functionalities are used to synthesize C-S-H/polymers and C-S-H/copolymers complexes. The characterization methods are used to study the structure and morphology of the complexes and the mechanical properties are examined using AFM nanoindentation.

Chapter 4 aims to investigate the effect of biomolecules on the microstructure and nanomechanical behavior of C-S-H. Amino acids with different functional groups, and proteins with different sizes and structures are used to synthesize C-S-H/biomolecules complexes. Experimental methods are utilized to investigate the possibility of adsorption of biomolecules onto C-S-H. Characterization methods are used to study the atomic structure of the complexes. Nanomechanical properties are examined using AFM nanoindentation.

In Chapter 5, C-S-H/polymer composites are synthesized using the LBL method and their morphology and mechanical properties are investigated. Nanocomposites are made using different sets of polymers to produce different morphologies and properties. In addition, GO nanosheets are used in the LBL assembly to elucidate the interaction between GO nanosheets and C-S-H/polymers and their effects on the morphology of the nanocomposites. GO nanosheet with a sheet like structure and functional groups obtained during the oxidation process are considered a promising additive for cementitious materials [20,113]. It is shown that use of GO nano sheets can improve the mechanical properties of

cement paste at macroscale by modifying the formation and regulating the microstructure of C-S-H [92–94]. Therefore, GO nanosheets are incorporated in the LBL fabricated C-S-H/polymer nanocomposite to obtain insight into their effect on the nanocomposite. The planar shape of GO is well suited to study its interaction with C-S-H in LBL fabricated nanocomposites.

The fundamental knowledge obtained from this research can set the stage for a new design paradigm to engineer innovative infrastructure materials. The primary hypothesis pursued here is based on the premise that polymers and biomolecules can provide diverse interaction pathways with the nanostructure of C-S-H, which, in turn, can be exploited to direct the microstructure and mechanical properties of C-S-H. The ability to tune the properties of C-S-H by the means of versatile polymers and biomolecules will open a new paradigm in the design of bio-inspired cementitious materials with superior mechanical properties to address critical needs for innovation in civil infrastructure materials. The cement and concrete industry is entitled to new developments and inventions in order to preserve the progressive nature of concrete [2]. Concrete continues to reflect the needs of society and in the present our need is to implement strategies for achieving sustainable developments in order to build our prosperous, just and secure future [3].

Chapter 2

2. Experiments

In this chapter some of the test methods used to study the atomic structure, morphology and mechanical properties of the C-S-H complexes are introduced. It is important to note that a combination of these test methods are often required to obtain a conclusive understanding of the structure and properties of the complexes, as each test method has its own limitations. The materials used in this study as well as synthesis procedures followed to prepare the C-S-H composites are also described in this chapter.

2.1. Test Methods
2.1.1. Total Organic Carbon (TOC) Measurement

TOC is an analytical technique that measures the amount of organic molecules and contaminants in water, and can be used as an indicator of water quality [114]. There are two types of TOC analyzers. One type measures the amount of organic carbon by the differential method and the other type works by the direct method. In the differential method, the amount of both inorganic carbon and total carbon is measured. Then the amount of organic carbon is calculated by subtracting the organic carbon from the total carbon. In the direct method, solutions are acidified with a concentrated H_3PO_4 to convert all inorganic carbon to carbon dioxide. The carbon dioxide is removed from the sample by purging the solution using a purified gas. Then, the sample is injected into a combustion tube and the amount of total carbon present in the solution is measured by the device. In this study the TOC method was used to measure the amount of adsorption of the biomolecules onto C-S-H. A Shimadzu TOC5000 Analyzer was used for TOC measurements.

2.1.2. X-Ray Diffractometry (XRD)

XRD is an analytical technique which is used to characterize crystalline materials. X-ray diffractometers consist of an X-ray tube, a sample holder and an X-ray detector. X-rays are generated in a cathode ray tube by heating a filament to produce electron beams. These beams are filtered and directed toward the sample. Diffracted beams are collected and analyzed to investigate the structure of the sample. In a crystalline material, the atoms are located in a repeating order as is shown in Figure 2.1. Since the wavelength of X-ray is the same order of magnitude as the spacing between the planes in crystals, a significant diffraction is produced once the X-ray beams hit the parallel layers. This facilitates the measurement of the distance between the planes in the structure of a crystalline material. The interlayer distance of samples is calculated using Bragg's equation [115]:

$$2dSin\,\theta = n\lambda \tag{2.1}$$

where d is the interlayer distance (Å), θ is the peak angle (degrees), n equals 2 and λ is 1.5418 (Å) for the Cu source .
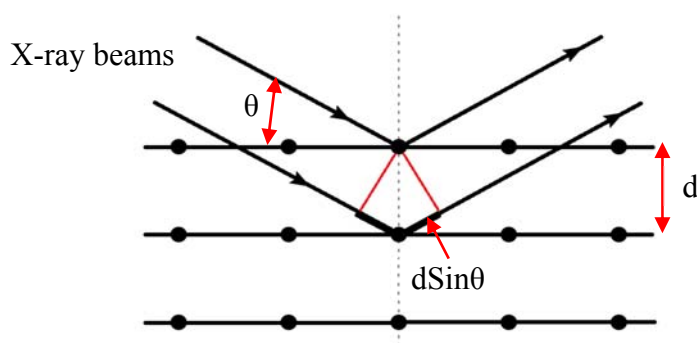
Figure 2.1 X-ray diffraction for crystalline materials.

XRD which is particularly effective in characterizing materials with a layered structure has been successfully utilized in studying cement-based materials [16,25,116]. The XRD spectrum of a cement paste powder after 28 days of aging is shown in Figure 2.2.

In this study, the change in the interlayer distance of C-S-H nanolayers was evaluated by measuring the change in the reflection peak corresponding to the 002 basal spacing in the XRD spectrum. A Siemens XRD was used to conduct the experiments.
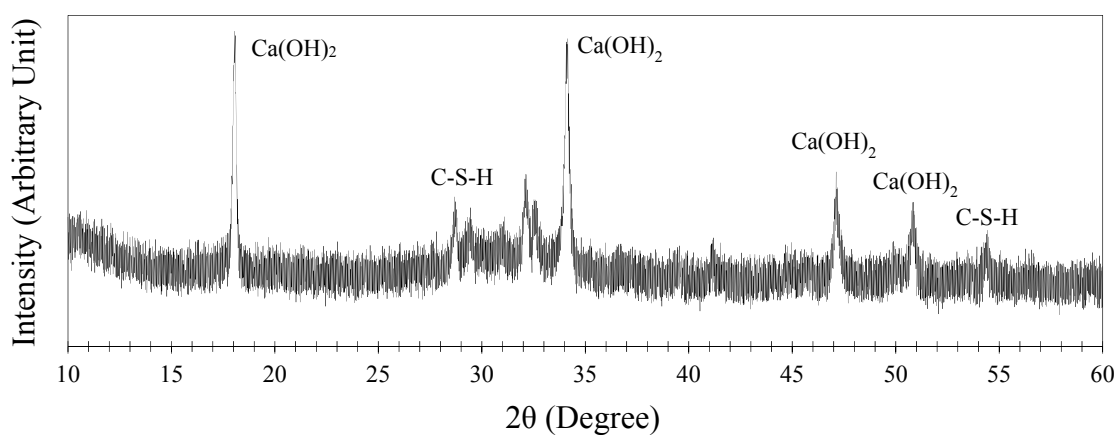
Figure 2.2 XRD spectrum of a cement paste powder after 28 days of aging.

2.1.3. Fourier Transform Infrared Spectroscopy (FTIR)

FTIR spectroscopy is an analytical method for detecting functional groups and characterizing chemical bonds, and has a variety of applications in chemistry, especially in the field of polymers and organic compounds. In this technique, an infrared spectrum of absorption or emission of the sample is produced. The chemical bonds in molecules of the sample can be identified by analyzing this spectrum. The produced infrared spectrum is a distinctive molecular fingerprint which is unique to each material [117].

In this study, FTIR was used to study the polymerization of silicate chains in C-S-H nanolayers. In this method, the characteristic stretching vibrations of Si-O bonds was used to identify different silicate bonds present in C-S-H [15,16,118]. The presence and intensity of the middle chain silicate tetrahedra (Q^2) and end chain silicate tetrahedra (Q^1) can be detected using the FTIR spectra (Figure 2.3). An increase in the (Q^2/Q^1) ratio is usually an indication of an increase in the polymerization of silicate chains. The degree of silicate chain polymerization is dependent on the composition and C/S ratio [119]. The FTIR analysis was conducted using a Perkin Elmer Paragon 1000 FTIR.
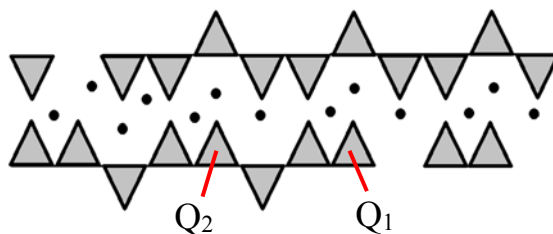
Figure 2.3 Middle chain silicate tetrahedra (Q^2) and end chain silicate tetrahedra (Q^1) in C-S-H.

2.1.4. Zeta Potential

Zeta potential is defined as the electrokinetic potential in colloidal dispersions. There is no direct method of measuring zeta potential but it can be calculated using indirect methods. When an electric field is applied to the electrically charged particles of a colloidal suspension, they exhibit different effects called the electrokinetic effects [120]. For example, the applied electric filed can affect the movement of colloidal particles in the suspension. Under the influence of an applied electric filed, the charged particles in the liquid move toward the electrode of opposite charge. Once the electric forces on the particles are in balance with the viscous forces, particles move with a constant velocity.

The velocity of the colloidal particles under the influence of the electric field is called the electrophoretic mobility. The zeta potential can be calculated by determining the electrophoretic mobility and applying Henry equation as follows [120]:

$$U_E = \frac{2\varepsilon z f(\kappa a)}{3\eta}$$
(2.2)

where, z is the zeta potential, U_E is the electrophoretic mobility, ε is the dielectric constant, η is the viscosity and $f(\kappa a)$ is the Henry's function which is approximated to be either 1 or 1.5.

In this study, a Malvern Zetasizer was used to measure the charge and size of polymers, polymer complexes and C-S-H particles.

2.1.5. Scanning Electron Microscopy (SEM)

A scanning electron microscope is a type of electron microscope that uses a focused high-energy beam of electrons to scan the surface of a solid sample. Once the beam hits the sample, electrons interact with atoms in the surface of the sample, and electrons and X-rays are ejected by the sample as is shown in Figure 2.4. Secondary electrons, backscattered electrons and X-rays ejected from the sample are detected by the microscope detector and converted into signals. These signals are analyzed to obtain information about the morphology and composition of the sample. Secondary electrons are emitted when atoms on the surface of the sample are excited by the electron beam. Secondary electrons are detected to provide information about the morphology and topography of the sample. Once excited electrons return to lower energy shells, they emit X-rays. Wavelengths of the X-rays are dependent on differences between energy levels of electrons which is unique to each element. The emitted X-rays are detected by the microscope to characterize

component elements of the sample. Backscattered electrons provide information regarding the composition of multiphase systems. They are detected and analyzed to illustrate the variation in the composition by a varying contrast. In this study, the morphological characteristics of C-S-H was examined using a FEI XL-30 Field Emission ESEM/SEM.
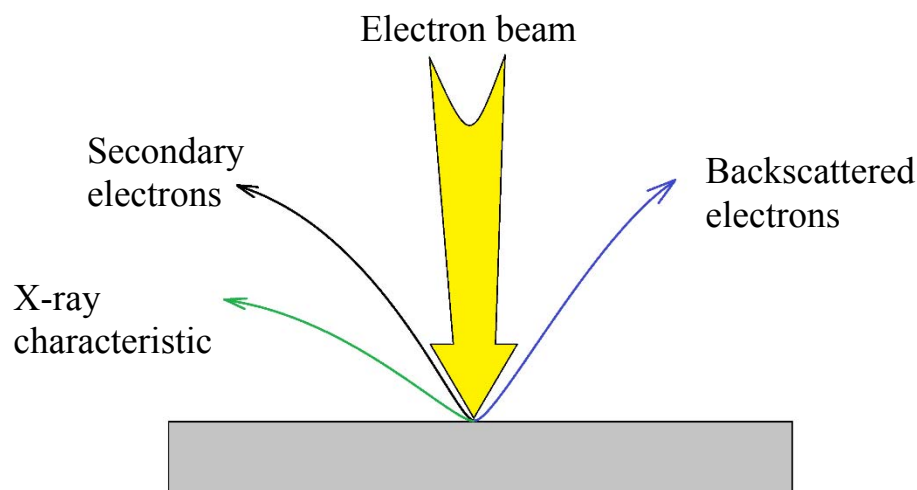
Figure 2.4 Emitted signals once an electron beam interacts with the surface of the sample.

2.1.6. Atomic Force Microscopy

An atomic force microscope is a type of scanning probe microscope which is primarily designed for imaging at the nano and micro scale and measuring the fundamental interaction forces between different materials [121]. In AFMs, a sharp probe assembled on a cantilever raster scans a small area of the sample. The vertical and lateral deflections of the cantilever are measured by an optical lever which collects a laser beam reflected off the back of the cantilever as is shown in Figure 2.5. AFMs can operate in contact or non-contact mode. The morphology of the samples were studied using a TT-AFM from AFMWorkshop. A silicon probe from AppNano with a cantilever length and width of 225

µm and 40 µm, a tip radius of less than 10 nm and spring constant of 36-90 N/m was used

for imaging. Images of each sample were taken in the non-contact mode
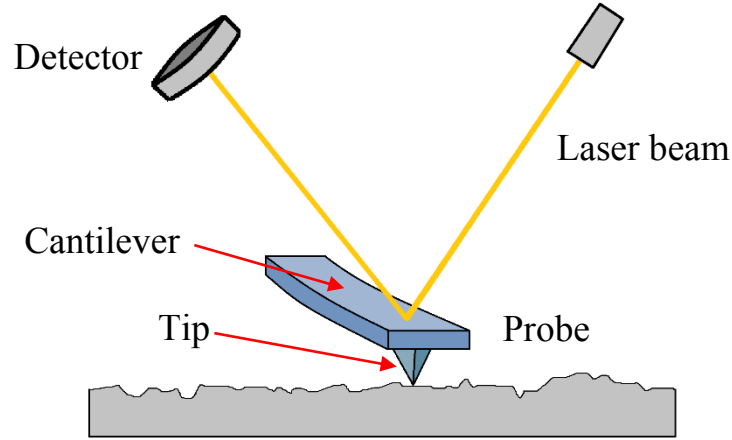
Figure 2.5 Basic components of light lever AFM detection system.

AFM is shown to be useful in the determination of the Young's modulus of materials

with mechanical properties changing over a nanoscale [24,122] making it a promising

method for mechanical characterization of cementitious materials [24].

In AFM indentation test a probe with a known cantilever stiffness comes into contact

with the material, indents up to a certain depth and then retracts from the surface as is

shown in Figure 2.6a. The deflection of the beam versus vertical position of the tip is

recorded by the instrument. Deflection data is logged as an electrical signal in volts units

that needs to be converted to length unit using a sensitivity factor. Sensitivity is calculated

as the slope of a linear fit to voltage-distance curve when the same probe is pushed against

a relatively hard surface compared to the material to be tested so that the indentation depth

can be assumed to be negligible. Deflection is converted to force using the spring constant

of the cantilever and Hooke's law to obtain the force-distance curves. The amount of

deflection corresponding to the cantilever response obtained from the test on the hard

surface with no penetration is subtracted from the total deflection to generate force-indentation distance curves.

In this study, the force-indentation distance of the unloading curves were fitted to Hertz model using the following formula [123] in a Matlab code:

$$F = \frac{4}{3} M R^{0.5} \delta^{1.5}$$ (2.3)

where F is the force in nN, R is the tip radius in nm and M is calculated with the following expression:

$$\frac{1}{M} = \frac{1 - v_1^2}{E_1} + \frac{1 - v_2^2}{E_2}$$ (2.4)

where v_1 and E_1 are the Poisson's ratio and Young's modulus (GPa) of the material and v_2 and E_2 are the Poisson's ratio and Young's modulus (GPa) of the AFM tip. Since a diamond probe was used in this study and the value of the Young's modulus of diamond is much higther than that of the material being tested, the above-mentioned expression was simplified as follows:

$$\frac{1}{M} = \frac{1 - v_1^2}{E_1}$$ (2.5)

In this study, a cube corner diamond probe (DNISP from Bruker) with a spring constant of 291 N/m and a tip radius of 40 nm based on the specification provided by the manufacturer was used for AFM indentation. The deflection sensitivity was calibrated using a sapphire substrate purchased from Bruker.
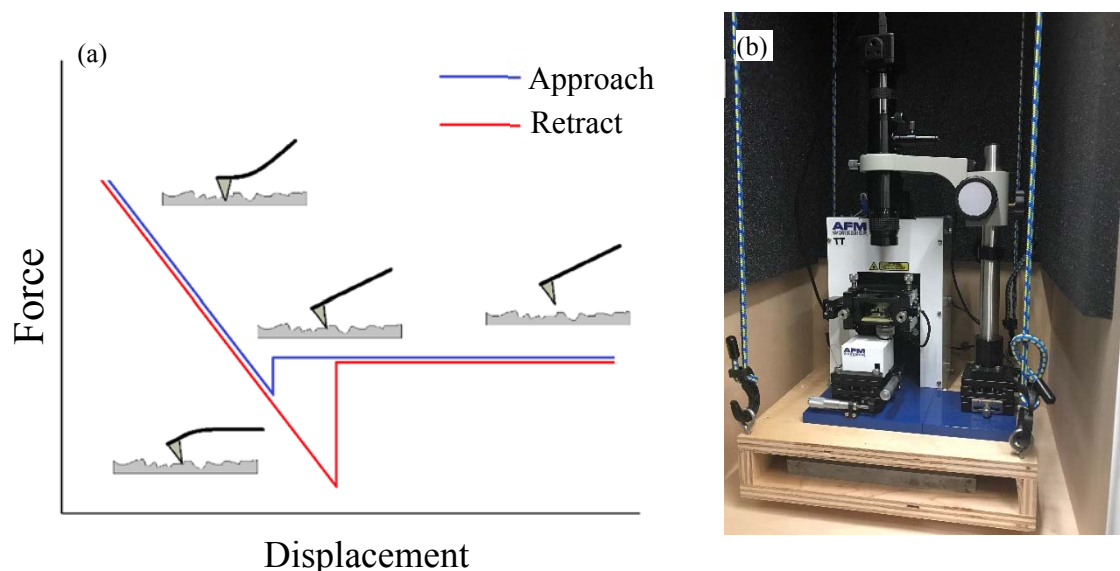
Figure 2.6 (a) Interaction of the cantilever tip with the surface of the sample in AFM nanoindentation, (b) image of the AFM device.

2.2. Materials
2.2.1. C-S-H Composites

In this study, a set of cationic, anionic and polar polymers, a set of amphiphilic copolymers, four types of amino acids and three types of proteins were used. The name and properties of the polymers are listed in Table 2.1. The structure of these polymers is depicted in Figure 2.7. Polyvinyl alcohol (PVA) is a water-soluble polymer that has hydroxyl groups in the monomers and capable of hydrogen bonding. Poly(diallyldimethylammonium chloride) (PDDA) contains strong cationic groups. Because of its charge stability at high pH, PDDA is used to stabilize the negatively charged matters in waste water [124]. Poly(acrylic acid) (PAA) is an anionic polymer that has carboxyl groups on every two carbon atoms of the main chain. PAA is one of the most commonly used water-soluble anionic polymers for different applications such as dispersing agent, superabsorbent polymer, ion-exchange resin and etc. [125–127].

Name	Abbreviation	Mw (g/mol)	Charge
Polyvinyl alcohol	PVA	1900	Non-charged
Poly(diallyldimethylammonium chloride)	PDDA	8000	Positive
Poly(acrylic acid)	PAA	16000	Negative

Table 2.1 List of cationic, anionic and polar polymers used in this study.
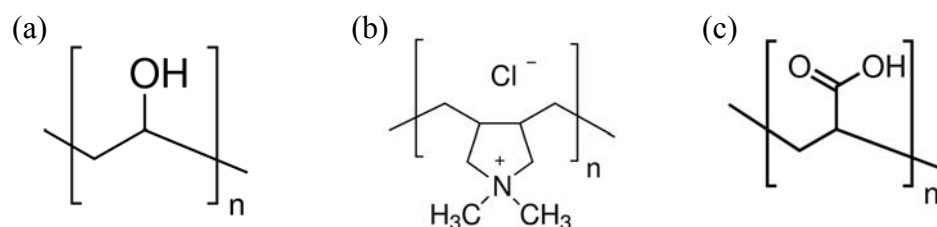
Figure 2.7 Chemical structure of (a) PVA, (b) PDDA and (c) PAA.
(Structures are from SigmaAldrich website).

The name and properties of copolymers are listed in Table 2.2. The structure of the copolymers is shown in Figure 2.8. Poly(ethylene glycol) (PEG) is a polymer with unique properties that has numerous applications in polymer and surfactant technology. PEG with 1 oxygen atom and 2 methylene groups in the backbone is water-soluble. However, structurally similar polymers with 1 or 3 methylene groups in their backbone are hydrophobic and insoluble in water. The properties of PEG have been shown to be dependent on molecular weight of the polymer [128]. Triblock copolymers of PEG and poly(propylene glycol) (PPG) are one group of extensively used polymeric surfactants. PPG acts as the hydrophobic part in the amphiphilic structure of PEG-PPG block copolymers. The mass ratio of PEG to PPG as well as the sequence of the blocks play an important role in the way they behave in water [129]. PEG-PPG-PEG block copolymers

and PPG-PEG-PPG block copolymers are two groups of PEG-PPG block copolymers that have been studied by researchers [129–132] .

PEG-PPG-PEG with three different molecular weights was used to elucidate the effect of size of copolymers on the structure and properties of C-S-H. PPG-PEG-PPG and O,O′-Bis(2-aminopropyl) PPG-PEG-PPG are two other copolymers of PEG and PPG with the comparable molecular sizes. The latter has 2 polar functional groups of aminopropyl groups at two ends of its chain while the former has no any additional functional groups. Poly(1-vinylpyrrolidone-co-2-dimethylaminoethyl methacrylate) was used as the very high molecular weight amphiphilic copolymer.

Name	Abbreviation	M_n (g/mol)	PEG Content (%)
Poly(ethylene glycol)-block-poly(propylene glycol)-block-poly(ethylene glycol)	PEG-PPG-PEG1900	1900	50
Poly(ethylene glycol)-block-poly(propylene glycol)-block-poly(ethylene glycol)	PEG-PPG-PEG8000	8000	80
Poly(ethylene glycol)-block-poly(propylene glycol)-block-poly(ethylene glycol)	PEG-PPG-PEG16000	16000	82.5
Poly(propylene glycol)-block-poly(ethylene glycol)-block-poly(propylene glycol)	PPG-PEG-PPG	3300	10
O,O′-Bis(2-aminopropyl) poly(propylene glycol)-block-poly(ethylene glycol)-block-poly(propylene glycol)	Aminopropyl PPG-PEG-PPG	2100	50
Poly(1-vinylpyrrolidone-co-2-dimethylaminoethyl methacrylate)	PVP-DMEMA	1000000	-

Table 2.2 List of copolymers used in this study.

(a)

(b)

(c)

(d)
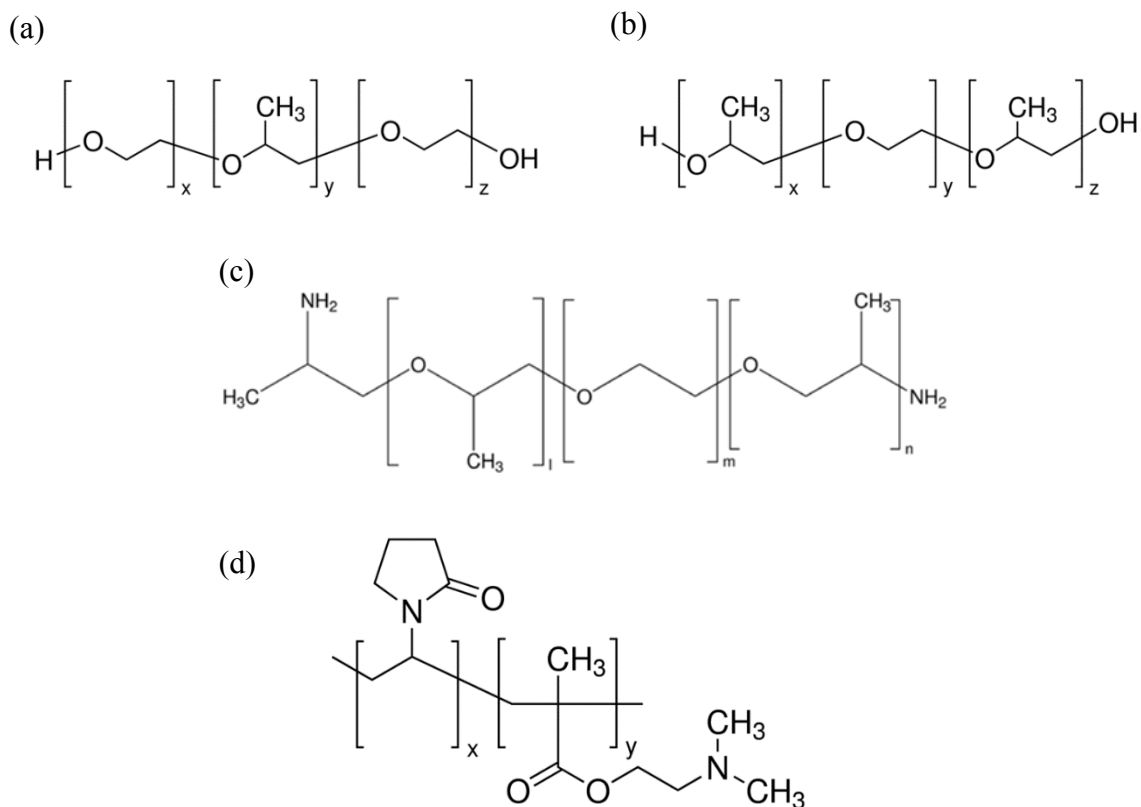
Figure 2.8 Chemical structure of (a) PEG-PPG-PEG, (b) PPG-PEG-PPG, (c) Aminopropyl PPG-PEG-PPG and (d) PVP-DMEMA (Structures are from www.sigmaaldrich.com).

Biomolecules used in this study including four amino acids with different functional groups and proteins are listed in Table 2.3. Because of their small size as well as their simple chemical structure, the possible interactions between amino acids and C-S-H is anticipated to be only related to their functional groups. Charged amino acids included arginine and glutamic acid, H-bonding amino acid was glutamine, and hydrophobic amino acid was leucine. The structure of the amino acids is shown in Figure 2.9.

Name	Charge	Description
Arginine	Positive	Natural amino acid
Glutamine	Polar	Natural amino acid
Leucine	Nonpolar	Natural amino acid
Glutamic acid	Negative	Natural amino acid
Lysozyme	-	From chicken egg white
Albumin	-	Bovine serum albumin (BSA)
Hemoglobin	-	Human hemoglobin

Table 2.3 List of biomolecules used in this study.
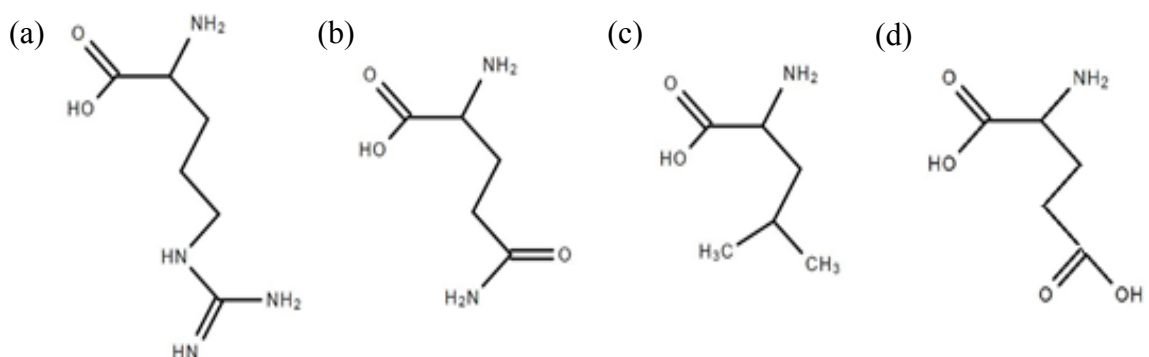
Figure 2.9 Structure of (a) arginine, (b) glutamine, (c) leucine and (d) glutamic acid.

Three proteins including lysozyme, albumin, and hemoglobin were also studied. The structure and estimated isoelectric point (PI) of the proteins are shown in Table 2.4. The structure is extracted from an online resource powered by the Protein Data Bank Archive [133–141]. The PI value is estimated using H++ 3.0, an automated system that computes PI values of ionizable groups in biomolecules at a specified pH [142–145]. Albumin has the largest size among the proteins. The percentage of amino acid residues with different pK_a values present in the structure of the proteins is shown in Figure 2.10. pK_a is an index that determines the acidity of materials. It is evident that a higher number of amino acid residues with higher pK_a values are present in the structure of lysozyme.
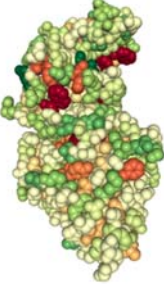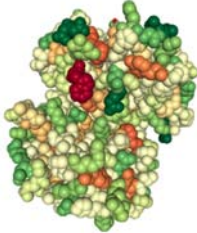
Name	Lysozyme	Albumin	Hemoglobin
Structure			
Diameter (nm)	4	5.5	5
Number of ionizable amino acid residues	86	440	87
PI	10.6	5.47	7.96

Table 2.4 Specification of the proteins used in this study.
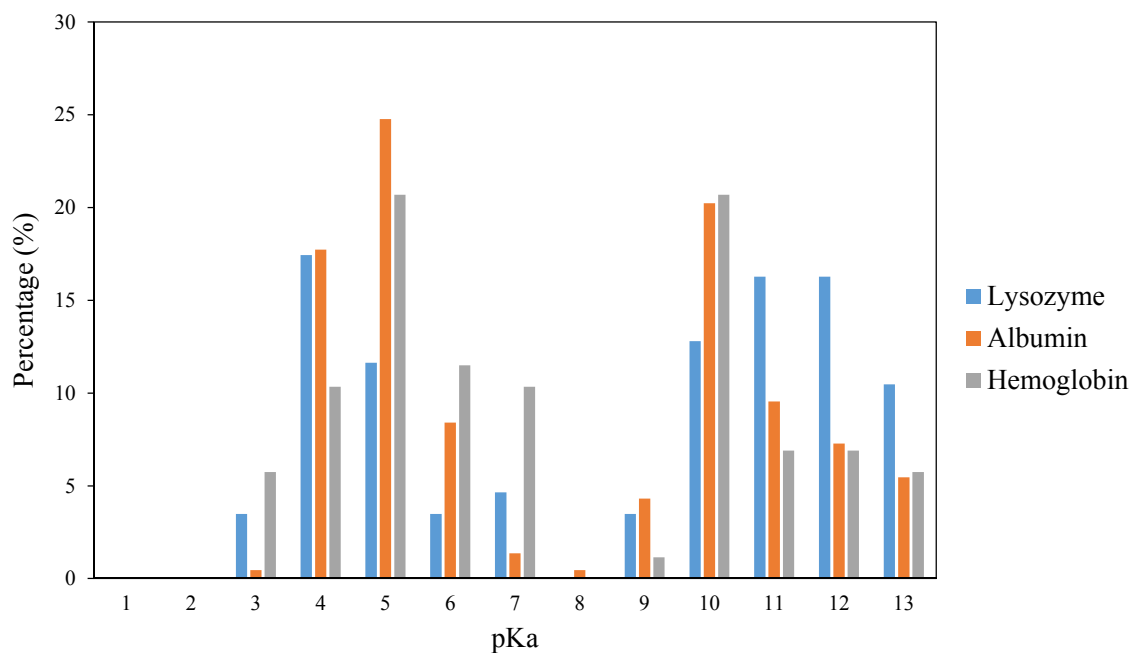
Figure 2.10 Percentage of ionizable amino acid residues with different pK_a values in the structure of the proteins.

2.2.2. Layer-by-Layer Fabrication

To prepare the C-S-H/polymer composite using LBL method, calcium acetate, sodium silicate, two types of cationic polymer, and two type of anionic polymer were used. Cationic polymers were poly(ethyleneimine) (PEI) with a molecular weight of $M_w = 750$ k g/mol and poly(diallyldimethylammonium chloride) (PDDA) with a molecular weight of $M_w = 200$-350 k g/mol. PEI contains amino groups but PDDA is a quaternary ammonium polyelectrolyte [146]. Anionic polymers included poly(sodium 4-styrenesulfonate) (PSS) with $M_w = 70$ k g/mol and poly(acrylic acid) (PAA) with $M_w = 250$ k g/mol.

Graphene oxide (GO) was used in preparing GO/C-S-H/polymer composites and purchased in the form of a dispersion with a concentration of 5 mg/ml. To measure the thickness and size of the GO nanosheets a diluted solution of the dispersion was placed on the surface of a freshly cleaved mica and rinsed after a few minutes. The surface of the mica was scanned by AFM. The AFM scan of the mica surface is shown in Figure 2.11. It is seen that the GO nanosheets are about 1 nm in thickness and 1-2 μm in the planar dimensions.
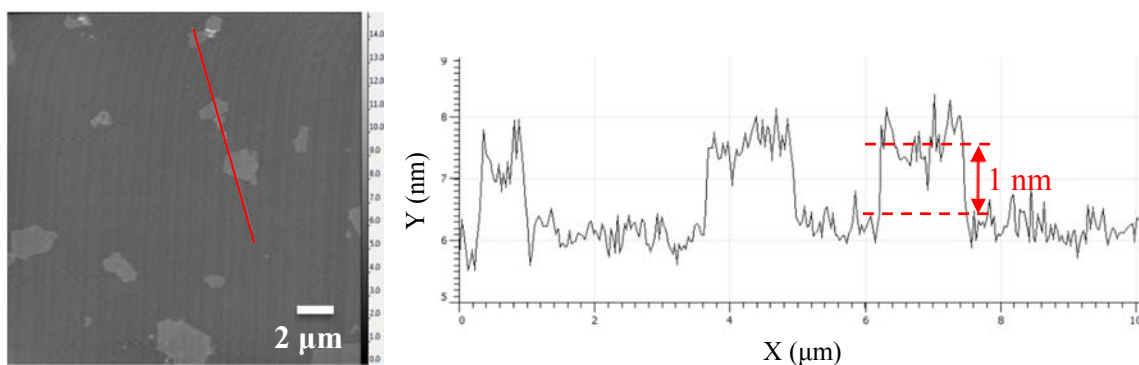
Figure 2.11 AFM scan of GO nanosheets adsorbed on the mica substrate.

2.3. Sample Preparation

C-S-H can be produced from the direct reaction of lime and silica in an excess of water through pozzolanic reaction [11]. Another way to synthesize C-S-H is through precipitation, when a calcium salt and silicate solution react with each other [147]. The amount of crystalline C-S-H produced in pozzolanic method is more than that of precipitation method. However, the pozzolanic reaction has been observed to be slower than precipitation. In this study, C-S-H with varied C/S ratios was synthesized in the form of powder using direct precipitation by the reaction of calcium and silicate ions in an aqueous solution. A 1 M $CaCl_2$ solution was gradually added to a 0.22 M Na_2SiO_3 solution and stirred for seven days on a hot plate at 60ºC in a CO_2 free glovebox in order to prevent carbonation. The synthesis set up is shown in Figure 2.12a. The solutions were filtered and washed with deionized water and acetone and then dried under vacuum for three days and then passed through a #60 sieve to obtain a fine powder. The fine powders were stored in the CO_2 free glovebox and were only taken out for performing experiments to minimize the amount of exposure to air. The sample powders for SEM, XRD and FTIR were transferred in sealed glass vials.
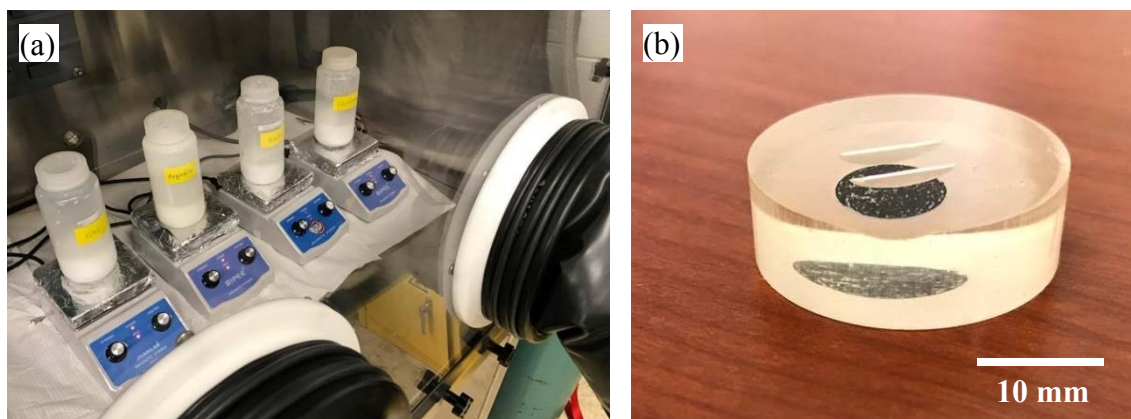
Figure 2.12 (a) Synthesis of C-S-H samples in a CO_2 free glove box, (b) C-S-H pellet set in epoxy for nanomechanical testing and AFM scanning.

The preparation of the C-S-H samples modified with organic compounds was the same as the control C-S-H sample, except that the organic compounds were pre-dissolved in the Na_2SiO_3 solution before the addition of $CaCl_2$ solution. Polymers with concentrations corresponding to 0.5 g of polymer to 1 g of calcium salt, copolymers with concentrations corresponding to 0.025 g of copolymers to 1 g of calcium salt, and biomolecules with concentrations corresponding to 0.025 g of biomolecule to 1 g of calcium were added to the Na_2SiO_3 solution. The pH value of the Na_2SiO_3 and polymer, and Na_2SiO_3 and copolymer solutions was increased to 13.3 by addition of the required amount of a 5 M NaOH solution. In preparation of C-S-H samples with biomolecules the pH was not increased with NaOH in order to avoid deprotonation of the biomolecules.

For mechanical testing the C-S-H powder was placed into a stainless steel mold and compacted using a loading machine to a pressure of 30 ksi to obtain a pellet with a diameter of 0.5 in. The pellets were cast in epoxy and then the surface of the samples were polished using SiC sand papers with grit numbers of 80, 180, 320, 600 and 1200, respectively. Isopropyl alcohol was used as a lubricating medium instead of water. Final polishing was performed using a diamond paste containing abrasive particles with a size of 1 μm. Samples were ultrasonically cleaned in isopropyl alcohol for 30 min to remove the polishing residues. The polished samples were used in performing nanoindentation and AFM scanning (Figure 2.12b).

For total organic carbon (TOC) measurement 6.66 ml of a 1g/l amino acid or protein solution was mixed with 31.5 ml of a 3.7 mM sodium silicate solution. 4 ml of a 30 mM calcium chloride solution was added gradually to the continuously stirring biomolecule and sodium silicate solution. The resulting solution had a C to S ratio of 1, and grams of

biomolecule to grams of calcium salt ratio of 0.5. The solutions were stirred for 3 days and then filtered. Reference samples containing only amino acids or proteins were also prepared and used in determining the amount of adsorption of the biomolecules onto C-S-H.

To prepare the C-S-H/polymer composite using LBL method, 0.4 g of polymer was dissolved in 200 g of deionized (DI) water. The various amounts of sodium silicate and calcium acetate were added to the negatively charged polymer solutions and positively charged polymer solutions, respectively, to achieve the desired C/S ratios and calcium ion concentrations. A glass slide was used as the substrate for LBL deposition. Substrates were cleaned with acetone and treated with a hot piranha solution until they stopped bubbling followed by rinsing with DI water. Piranha solution wipes off any organic residues and provides a negatively charged surface on glass slide. First, the substrate was dipped into a solution of positively charged polymer without calcium acetate for 20 min and then rinsed with DI water. Second, the substrate was dipped into a solution of negatively charged polymer without sodium silicate for 20 min followed by rinsing with DI water. These two layers served as a cap layer to facilitate the adhesion of the following layers. The LBL deposition was followed by dipping the substrate in the positively charged polymer solution with calcium acetate, rinsing with DI water, dipping the substrate in the negatively charged polymer solution with sodium silicate, rinsing with DI water and repeating these steps until the desired number of bi-layers formed on the substrate. Samples with three bi-layers were made for morphological study. For the nanomechanical testing, samples with 25 bi-layers were made to provide sufficient thickness for AFM nanoindentation. For the FTIR scanning, a polyacrylonitrile (PAN) substrate was used rather than a glass slide. No

piranha solution was used for preparing the PAN substrate. Instead, it was hydrolyzed in a 2 M NaOH solution for an hour and then rinsed thoroughly with deionized water before the layer by layer assembly.

For the nanocomposites made with GO, a 166 mg/l solution of GO in DI water was prepared. The solution was ultrasonicated for an hour to ensure the dispersion of GO nanosheets. After assembling the cap layer as previously explained, the substrate was dipped in the positively charged polymer solution with calcium acetate for 20 min, rinsed with DI water, dipped in the GO solution for 20 min, rinsed with DI water, dipped in the negatively charged polymer solution with sodium silicate for another 20 min and rinsed with DI water to form a trilayer. This procedure was repeated until the desired number of trilayers were assembled.

Chapter 3

3. C-S-H/Polymer and C-S-H/Copolymer Nanocomposites

In this chapter, cationic, anionic and polar polymers and amphiphilic copolymers were used to synthesize C-S-H. The effect of these polymers and copolymers on the structure and mechanical properties of C-S-H was investigated. Characterization methods including XRD and FTIR were used to study the structure of C-S-H. Morphological examination was performed using AFM. AFM indentation technique was used to investigate the nanomechanical properties of the C-S-H samples.

3.1. XRD Results

The XRD spectra for the control C-S-H and C-S-H samples modified with PVA, PDDA and PAA at a C/S of 0.8 and 1.5 are shown in Figure 3.1a and Figure 3.1b, respectively. The 2θ range of 3° to 10° corresponds to the peak of the d_{002} basal spacing reflection. As explained in Chapter 2, Bragg's equation was used to calculate the interlayer distance of the samples. The calculated interlayer distance for different C-S-H samples modified with the polymers is shown in Table 3.1.

At C/S of 0.8, it can be observed that in the C-S-H samples modified with PVA and PDDA the interlayer distance has increased compared to the control C-S-H sample. However, the change for the sample modified with PAA is insignificant. Statistical testing cannot be performed to confirm this statement because just one data point for each sample was obtained. The XRD results indicate the intercalation of PVA and PDDA into the C-S-H layers at this C/S ratio. At low C/S ratios each C-S-H nanolayer is composed of a CaO sheet sandwiched between silicate chains. Ideally the repeating unit of the silicate chain consists of three silicate tetrahedra, two facing the CaO sheet (pairing tetrahedral) and one

facing the interlayer region (bridging tetrahedron) similar to the structure of a natural mineral called tobermorite; however, in the structure of C-S-H some of the bridging tetrahedra are missing. C-S-H particles carry a negative net charge at C/S lower than 0.83 [11]. By increasing the C/S bridging tetrahedral are removed from the structure changing the charge of the C-S-H particles. The variability in the charge and structure of C-S-H as the C/S ratio changes, is responsible for the different mechanisms of interaction between polymers and C-S-H. The intercalation of the cationic PDDA between the negatively charged C-S-H layers at C/S of 0.8 can be explained by the electrostatic interaction in presence of silanol groups in the interlayer region. In case of PVA, hydrogen bonding to Ca-OH groups is the underlined mechanism of interaction [11]. At C/S of 1.5, no significant change was observed in the interlayer distance of the samples modified with PVA and PDDA. Statistical testing cannot be performed to confirm this statement because just one data point for each sample was obtained. The basal reflection peak in the sample modified with PAA is almost missing. The broad and flattened basal reflection peak in C-S-H sample modified with PAA has been observed in previous studies [11]. The binding of Ca^{2+} ions present in the C-S-H solution due to the complex formation in presence of anionic PAA has a retardation effect of the C-S-H formation [147]. The steric effect of the carboxylate groups in PAA keeps the particles apart from each other. It is expected for C-S-H to partially precipitate with a poorly crystalline structure in the presence of PAA.

	C/S = 0.8		C/S = 1.5	
	2θ	d (Å)	2θ	d (Å)
Control	5.8	15.3	6.2	14.3
PVA	5.4	16.4	6.3	14.1
PDDA	5.3	16.7	6.2	14.3
PAA	5.7	15.5	-	-

Table 3.1 The basal diffraction angle and interlayer distance detected in the XRD spectra of the control C-S-H powders and the samples modified with polymers.

Figure 3.1 XRD spectra of the Control C-S-H and C-S-H samples modified with polymers at C/S of (a) 0.8 and (b) 1.5.

The XRD spectra for the control C-S-H and C-S-H samples modified with the amphiphilic copolymers at a C/S of 0.7 and 1.5 are shown in Figure 3.2a and Figure 3.2b, respectively. The calculated interlayer distance for different C-S-H samples is shown in Table 3.2. At C/S of 0.7, no significant difference is observed in the interlayer distance of the C-S-H samples modified with three types of PEG-PPG-PEG. The statistical testing to

confirm this statement is provided in Table A.1. At C/S of 1.5, an increase in the interlayer distance can be observed for the C-S-H samples modified with lower molecular weight of PEG-PPG-PEG indicating the interaction of the copolymers with C-S-H particles and possible intercalation of them between the C-S-H layers. An increase in the interlayer distance of the C-S-H samples modified with PPG-PEG-PPG and aminopropyl PPG-PEG-PPG was observed at C/S of 0.7 indicating the intercalation of the polymers between the C-S-H layers. Such an increase in the interlayer distance is seen to be less pronounced at C/S of 1.5. This trend is the opposite of the trend observed in the C-S-H samples modified with PEG-PPG-PEG. The increased influence of PPG-PEG-PPG on the interlayer distance of C-S-H seems to be related to higher concentration of hydrophobic PPG block in PPG-PEG-PPG compared to PEG-PPG-PEG copolymers. The properties of the PEG-PPG-PEG copolymers consisting of the two blocks of PEG and one block of PPG are mainly governed by the polar PEG segment. The lone pair electrons on the oxygen atom in PEG can electrostatically bind to positively charged Ca^{2+} [148]. However, in PEG-PPG-PEG copolymers the hydrophobic PPG segment is dominant.

At low C/S ratio, the silanol groups of C-S-H are deprotonated and gain negative charges on C-S-H surface. With an increase in C/S ratio, Ca^{2+} are attracted to the negatively charged surface of C-S-H during nucleation and growth of C-S-H shielding the C-S-H surface. The presence of Ca^{2+} on the C-S-H surface provides an interaction pathway with PEG block through electrostatic interactions. The ability of PEG to form a complex with Ca^{2+} has been proposed in previous studies [148]. The above explanation provides a rationale for the increased influence of PEG-PPG-PEG on the atomic structure of C-S-H at high C/S ratio. The more pronounced effect of PPG-PEG-PPG with a higher

concentration of hydrophobic block at lower C/S highlights the importance of other interaction mechanisms other than electrostatic interaction in polymer/C-S-H systems. As shown later in Chapter 4, the interaction between hydrophobic functional groups and C-S-H is also evident in the amino acids/C-S-H systems. A more detailed discussion of the effect of amino acids with distinct functional groups on C-S-H is provided in Chapter 4.
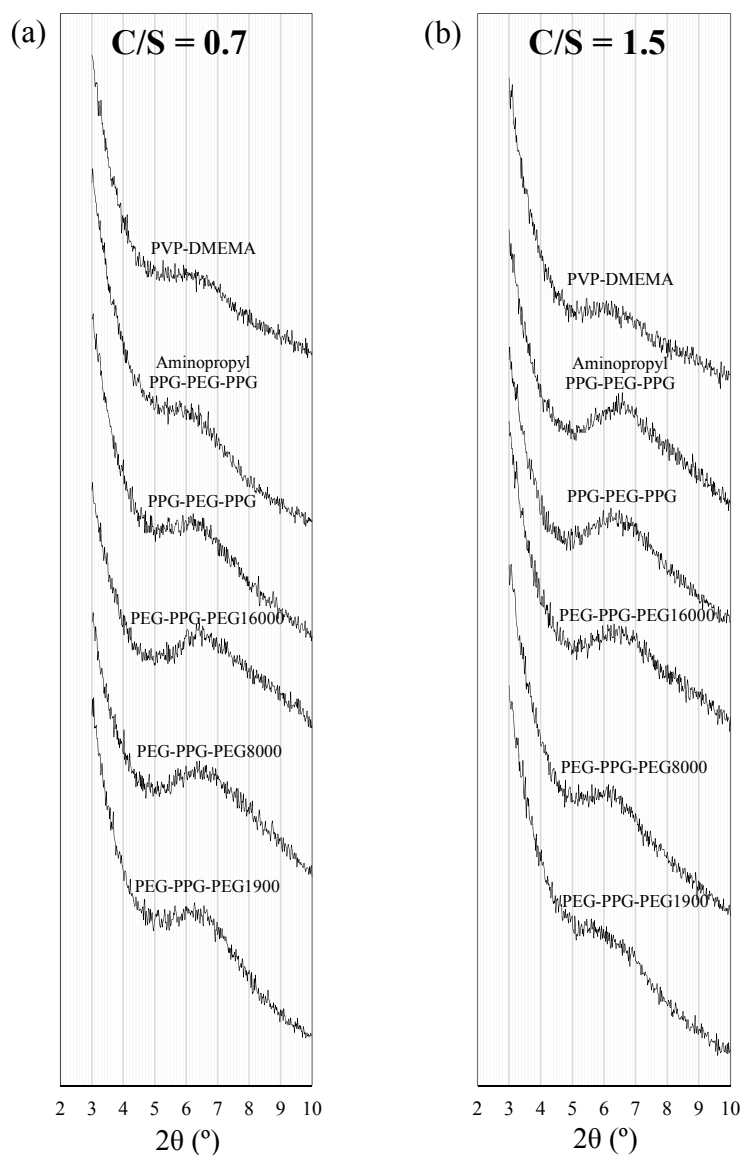
Figure 3.2 XRD spectra of the C-S-H samples modified with copolymers at C/S of (a) 0.7 and (b) 1.5.

The amount of intercalation and consequently the increase in the interlayer distance of C-S-H in the sample modified with aminopropyl PPG-PEG-PPG was observed to be higher than that of PPG-PEG-PPG at low C/S. This can be attributed to presence of the polar functional groups of aminopropyl in aminopropyl PPG-PEG-PPG that can interact through H-bond as well as ionic exchange with the negatively charged silanol groups of C-S-H at low C/S [149].

It is seen the samples with PVP-DMEMA show a modest increase in the interlayer distance at C/S of 0.7, but this increase becomes more at the higher C/S ratio. It is also observed that XRD spectra of the C-S-H samples modified with PVP-DMEMA have a broader and less intense basal reflection peak compared to the control sample. (2-dimethylamino) ethyl methacrylate becomes hydrophobic in the temperature range of 32-53 °C, which is below the temperature used for sample preparation of C-S-H powders [150]. Thus, PVP-DMEMA is expected to behave as an amphiphilic copolymer in the C-S-H/copolymer system being studied here. The main motivation to study this amphiphilic copolymer was to investigate the effect of a high molecular weight copolymer on C-S-H characteristics. The observed effect of this amphiphilic copolymer on increasing the interlayer distance is not agreement with the trend observed in PEG-PPG-PEG triblock copolymers where the influence of the copolymers with higher molecular weight appeared to be negligible. Thus, this indicates that the size of amphiphilic copolymers is not necessary the main factor affecting the influence of these polymer on C-S-H. More investigations are necessary to decouple the effect of size and hydrophobic/hydrophilic

compositions in the amphiphilic copolymers on the behavior of C-S-H/polymer nanocomposites.

	C/S = 0.7		C/S = 1.5	
	2θ	d (Å)	2θ	d (Å)
Control	6.55	13.5	6.6	13.4
PEG-PPG-PEG1900	6.4	13.8	6	14.8
PEG-PPG-PEG8000	6.5	13.6	6.2	14.3
PEG-PPG-PEG16000	6.5	13.6	6.5	13.6
PPG-PEG-PPG	6.3	14.1	6.5	13.6
Aminopropyl PPG-PEG-PPG	6	14.8	6.5	13.6
PVP-DMEMA	6.3	14.1	6.1	14.5

Table 3.2 The basal diffraction angle and interlayer distance detected in the XRD spectra of the C-S-H modified with amphiphilic copolymers.

3.2. FTIR Results

The FTIR spectra for the control C-S-H and C-S-H samples modified with polymers at C/S of 0.8 and 1.5 are shown in Figure 3.3a and Figure 3.3b, respectively. The location of Si-O stretching vibrations of the Q^2 tetrahedra is listed in Table 3.3. Q^2 corresponds to the bridging silicate tetrahedral.

According to Table 3.3, the shifts in the FTIR bands corresponding to Q^2 cannot be observed for PVA and PDDA at C/S of 0.8. However at C/S of 1.5, there is a shift to higher frequencies for the PVA sample and to lower frequencies for the PDDA sample. As explained in XRD section, the mechanism of reaction between the polymers and C-S-H is different for PVA and PDDA. The presence of cationic PDDA at C/ S of 1.5 where the C-S-H particles carry a positive net charge keeps the particles away from each other and leads to depolymerization of the C-S-H.

The significant change in FTIR spectra can be seen in the sample modified with PAA. The Si-O stretching band at 780 cm^{-1} corresponding to Q^1 is clearly seen in the samples with PAA but it is almost missing in other samples. Q^1 represents the end silicate tetrahedra. The sharper Q^1 band in samples with PAA compared to the other samples indicates the lower degree of polymerization in this mix design. In samples with PAA, Q^2 bands occur at higher frequencies. This difference can be attributed to presence of SiO_2 gel in this mixture. As mentioned before, PAA has a retarding effect on the nucleation of C-S-H. The silicate solution mixed with PAA requires more calcium salt solution and more time in order to facilitate C-S-H nucleation, otherwise the sample would be a mix of silicate gel, C-S-H in early polymerization stage and surface adsorbed polymer [147]. Other bands in PAA samples at 1408 cm^{-1}, 1562 cm^{-1} and 1453 cm^{-1} correspond to PAA at high pH [151]. The presence of polymer in the sample after multiple times washing with water and acetone can be because of surface adsorption on the particles.

	Q^2 (cm^{-1})	
	C/S = 0.8	C/S = 1.5
Control	985	996
PVA	984	1000
PDDA	985	975
PAA	1034	1068

Table 3.3 The wavelength numbers corresponding to Q^2 silicates in the FTIR spectra of the control sample and C-S-H samples modified with polymers.
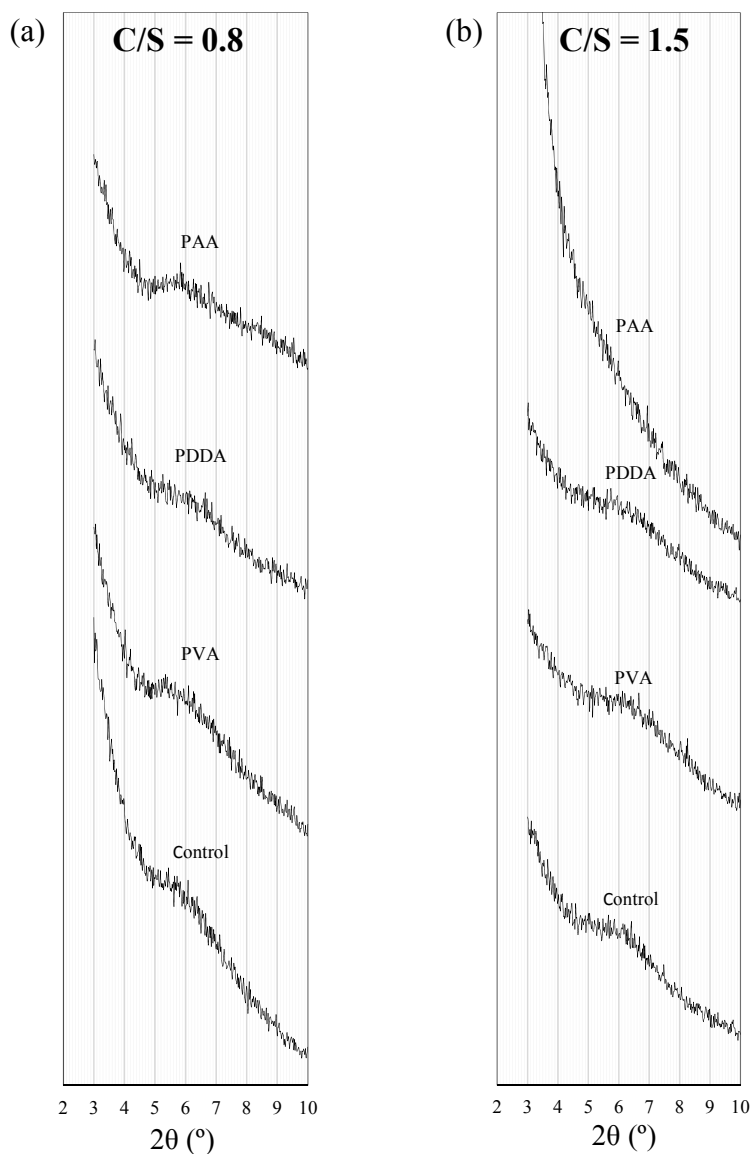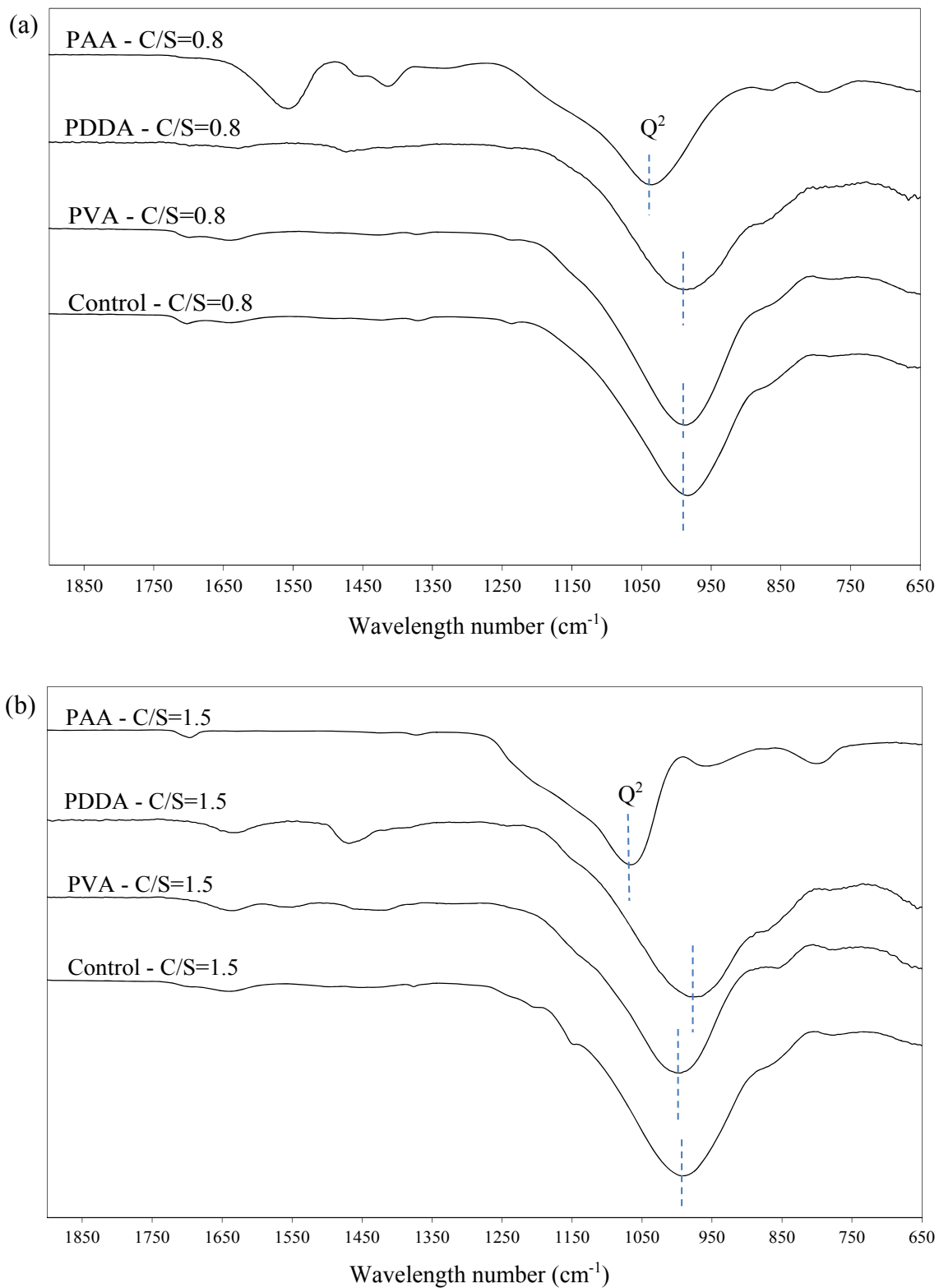
Figure 3.3 FTIR spectra of the control C-S-H and C-S-H samples modified with polymers at (a) C/S of 0.8 and (b) C/S of 1.5.

The FTIR spectra for the C-S-H samples modified with copolymers at C/S of 0.7 and 1.5 are shown in Figure 3.4 and Figure 3.5, respectively. The location of Si-O stretching vibrations of the Q^1 and Q^2 tetrahedra for different C-S-H samples are listed in Table 3.4. The intensity ratio of Q^2 to Q^1 is a measure of polymerization of silicate chains in C-S-H which is shown in Table 3.4. It is seen that samples modified with PEG-PPG-PEG all experienced an increase in Q^2/Q^1 indicating increased silicate polymerization compared to the control samples. In the samples modified with PEG-PPG-PEG, increasing the C/S from 0.7 to 1.5, resulted in a small decrease in the C-S-H silicate polymerization, which is in agreement with the prior studies in literatures [119]. It is noted that PEG-PPG-PEG16000 sample, exhibited a lower Q^2/Q^1 value than PEG-PPG-PEG1900 and PEG-PPG-PEG8000. The reduced influence of PEG-PPG-PEG copolymers with increasing molecular weight appears to be in general agreement with the influence of these polymers on the interlayer distance of C-S-H as evidenced from the XRD results presented in Figure 3.2. It is also observed that the C-S-H samples modified with lower molecular weight of PEG-PPG-PEG has a broader and less intense basal reflection peak compared to the control sample. It should be noted that the length of PEG block in the PEG-PPG-PEG with the lowest molecular weight is much smaller than that of PEG-PPG-PEG with higher molecular weights. It has been observed that the lower molecular weight PEG at lower concentration rates facilitates particle adhesion while the higher molecular weight PEG makes the particles repel [128,152]. Thus, it is expected to see intercalation and increased silicate polymerization in the C-S-H samples modified with smaller PEG-PPG-PEG and decreased silicate polymerization in the C-S-H samples modified with higher molecular weight PEG-PPG-PEG.

It is seen that Q^2/Q^1 ratio in both samples with PPG-PEG-PPG and aminopropyl PPG-PEG-PPG showed an increase compared to the control sample and this increase is slightly higher in PPG-PEG-PPG than aminopropyl PPG-PEG-PPG copolymers. The FTIR results of the sample modified with PVP-DMEMA also show an increase in polymerization at both C/S of 0.7 and C/S of 1.5. The increase in Q^2/Q^1 is more noticeable at C/S of 0.7 than at C/S of 1.5 as seen from Table 3.4. It should be noted that the more pronounced effect of this copolymer on silicate polymerization of C-S-H at the higher C/S ratio differs from the effect of this copolymer on interlayer distance. This highlights the different ways in which copolymers can affect the atomic structure of C-S-H.

	C/S = 0.7			C/S = 1.5		
	Q^2 (cm^{-1})	Q^1 (cm^{-1})	Q^2 / Q^1	Q^2 (cm^{-1})	Q^1 (cm^{-1})	Q^2 / Q^1
Control	996	779	3.70	1000	776	3.58
PEG-PPG-PEG1900	996	782	3.86	1004	779	3.83
PEG-PPG-PEG8000	997	776	3.99	1009	778	3.86
PEG-PPG-PEG16000	996	782	3.83	1002	779	3.78
PPG-PEG-PPG	996	781	3.91	1005	785	3.89
Aminopropyl PPG-PEG-PPG	995	778	3.85	998	778	3.78
PVP-DMEMA	996	778	3.98	1008	783	3.73

Table 3.4 The wavelength numbers corresponding to Q^2 and Q^1 silicates in the FTIR spectra of the C-S-H powders modified with the copolymers.
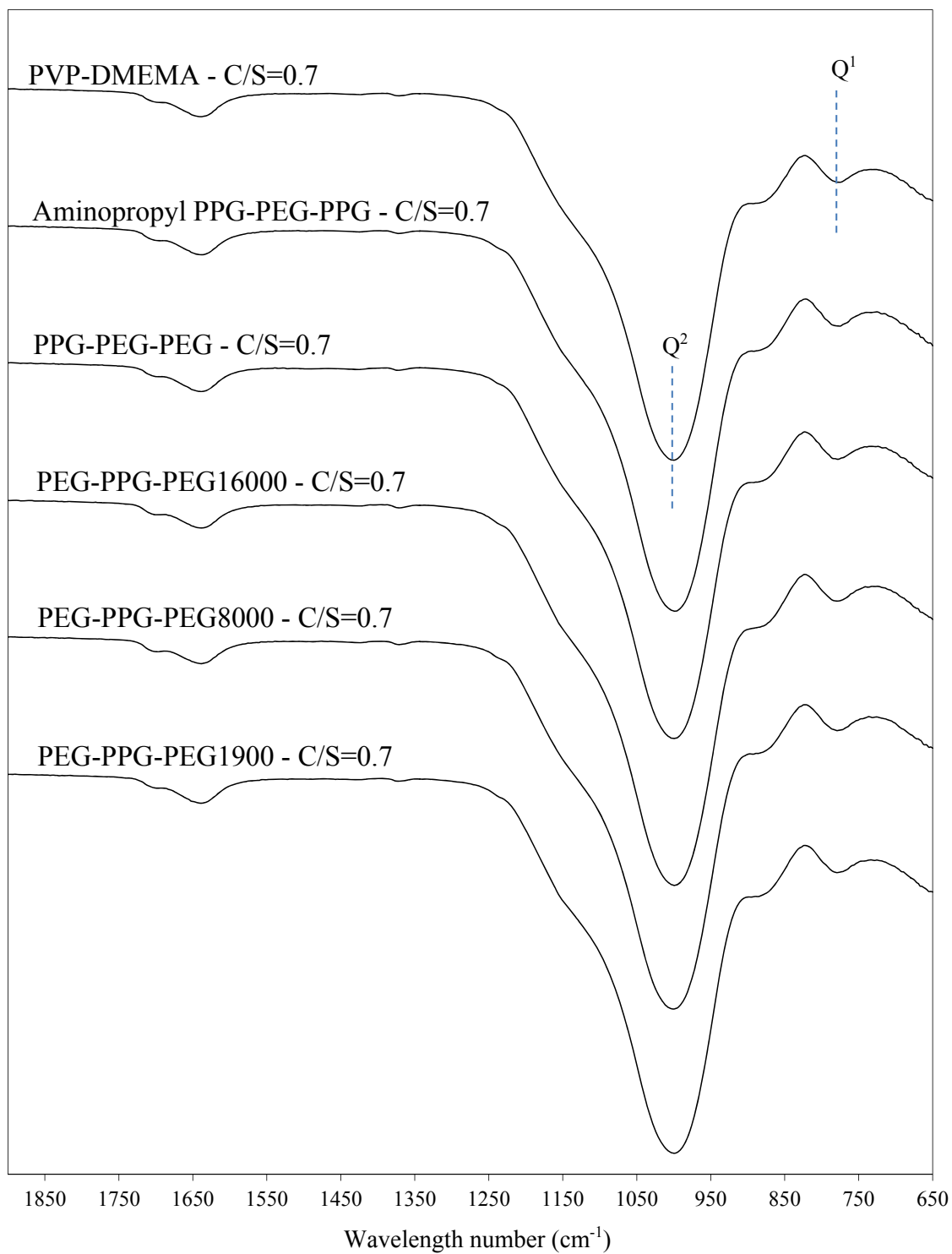
Figure 3.4 FTIR spectra of the C-S-H samples modified with amphiphilic copolymers at C/S of 0.7.

PVP-DMEMA - C/S=1.5

Q^1

Aminopropyl PPG-PEG-PPG - C/S=1.5

Q^2

PPG-PEG-PEG - C/S=1.5

PEG-PPG-PEG16000 - C/S=1.5

PEG-PPG-PEG8000 - C/S=1.5

PEG-PPG-PEG1900 - C/S=1.5

1850   1750   1650   1550   1450   1350   1250   1150   1050   950   850   750   650

Wavelength number (cm^{-1})
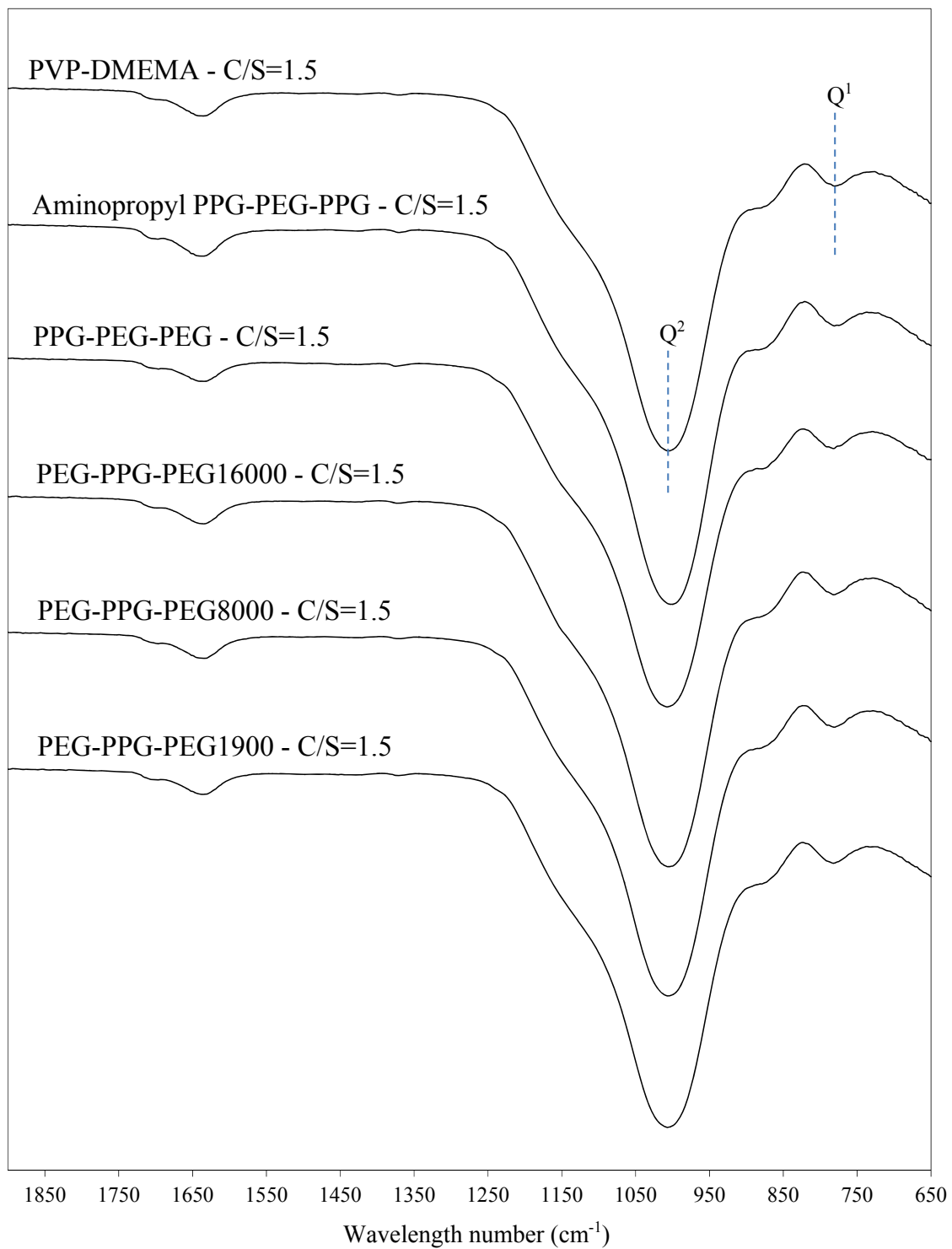
Figure 3.5 FTIR spectra of the C-S-H samples modified with amphiphilic copolymers at C/S of 1.5.

3.3. Morphology

The AFM images of the C-S-H samples modified with PVA, PDDA and PAA at C/S of 1 are shown in Figure 3.6. There is no noticeable difference in the morphology of the C-S-H samples modified with different polymers. The globular morphology with a size of 20 nm to 100 nm can be observed in all C-S-H samples.
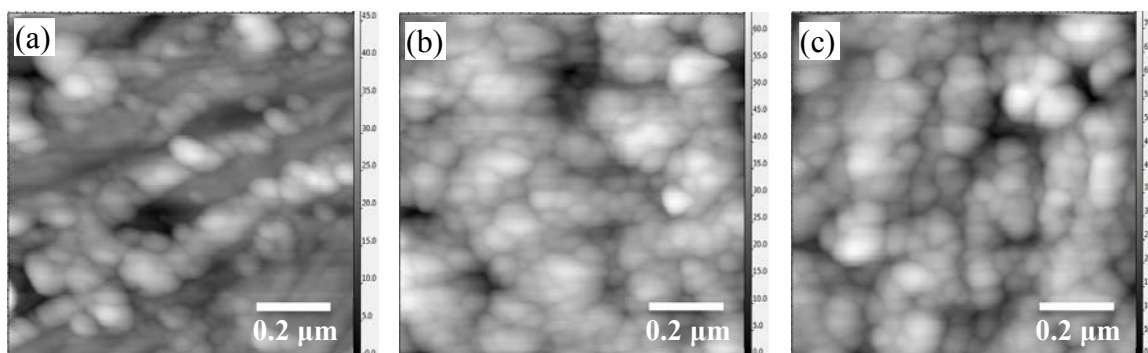
Figure 3.6 AFM morphology of the modified C-S-H with (a) PVA, (b) PDDA and (c) PAA at C/S of 1.

3.4. Mechanical Properties

3.4.1. Effect of C/S Ratio on Mechanical Properties of C-S-H

It has been shown that the intrinsic elastic modulus of C-S-H is independent of C/S ratio and degree of silica polymerization [153]. However, the packing density of the particles is a determining factor in calculation of mechanical properties. It has been confirmed that two types of C-S-H with different density levels and consequently different elastic modulus values tend to form in cementitious materials [154]. The volume fraction of these two types of C-S-H determines the overall mechanical properties of the C-S-H.

The multi-peak analysis of the nanoindentation results of the control C-S-H samples with C/S of 0.7, 1 and 1.5 are shown in Figure 3.7a, Figure 3.7b and Figure 3.7c,

respectively. The average value corresponding to each peak is calculated in Table 3.5. The peaks with an average value of 15.4 GPa and 15.2 GPa for C/S or 1 and 1.5, respectively, are attributed to the very low density C-S-H. The peaks with an average value of 21.2 GPa and 23.2 GPa for C/S or 0.7 and 1.5, respectively, are attributed to the low density C-S-H. In the sample with C/S of 1, the peak for low density C-S-H is missing giving a lower average value for the elastic modulus of C-S-H at this C/S rate compared to C/S of 0.7 and 1.5. These results are comparable to the previous studies [155]. The increased volume of low density C-S-H in the C-S-H sample with C/S of 1.5 compared to the one with C/S of 1 is attributed to the higher water content of the C-S-H at higher C/S. The higher water content increases the compatibility of the C-S-H and consequently the packing density of the particles [155]. The explanation for higher fraction of low density C-S-H at C/S of 0.7 compared to C/S of 1 is yet to be investigated. Some studies attributed that to the higher degree of polymerization of C-S-H at low C/S ratio [155]. However, it is established in other studies that the mechanical properties of C-S-H is independent of C/S ratio [153].

C/S	Average Young's Modulus (GPa)			
	Very Low Density C-S-H (VLD)	Low Density C-S-H (LD)	Calcium Hydroxide (CH)	
0.7	-	21.2	37.7	52.2
1	15.4	-	-	-
1.5	15.2	23.2	37.3	-

Table 3.5 The average elastic modulus values of the peaks corresponding to different phases in the control C-S-H samples at different C/S rates.
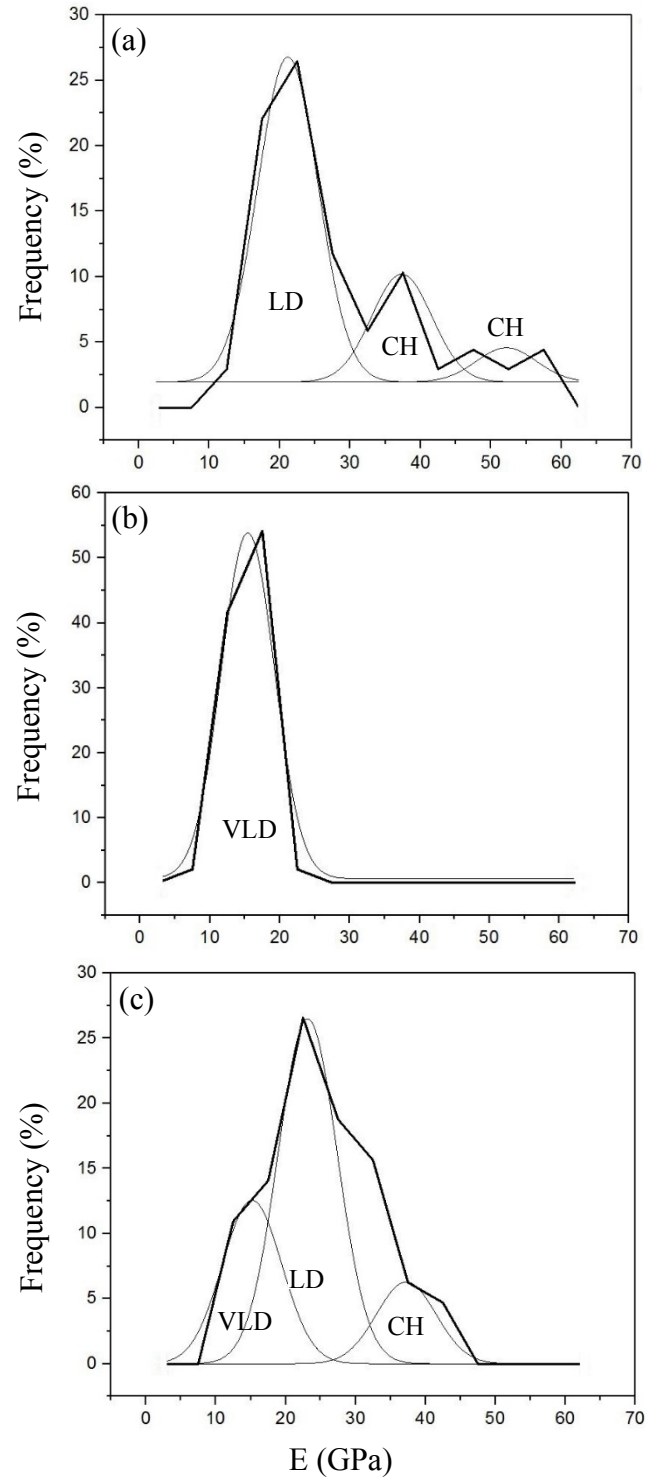
Figure 3.7 Multi-peak fitting of nanoindentation results for the control C-S-H samples at (a) C/S = 0.7, (b) C/S = 1 and (c) C/S = 1.5.

3.4.2. Effect of Polymers and Copolymers on Mechanical Properties of C-S-H

The elastic modulus values of the control C-S-H and C-S-H samples modified with PVA, PDDA and PAA at C/S of 1 are shown in Figure 3.8. At C/S of 1, the C-S-H modified with polymers showed lower values of Young's modulus compared to that of the control sample. The decrease in the value of elastic properties indicates the presence of these polymers adsorbed on the surface or in the voids between the C-S-H particles and consequently the less dense packing of the C-S-H sample. These results are comparable with previous studies [15,19]. The C-S-H sample modified with PDDA showed multiple peaks which is attributed to existence of different phases in the sample.

The elastic modulus values of the C-S-H samples modified with copolymers at C/S of 0.7 is shown in Figure 3.9. The Young's modulus value for the sample modified with PEG-PPG-PEG8000 was observed to be higher than that of the samples modified with PEG-PPG-PEG1900 and PEG-PPG-PEG16000. As explained before the mechanism of interaction of PEG polymer is highly dependent of the molecular weight and observed to be different in the PEG-PPG-PEG1900 and PEG-PPG-PEG16000 samples. The higher elastic modulus value of the PEG-PPG-PEG8000 sample might be attributed to the transitional properties which facilitate the optimum compaction in the C-S-H sample. More in depth investigation is needed to elucidate the underlying mechanism of interaction of the PEG-PPG-PEG copolymers. The C-S-H modified with PVP-DMEMA showed lower values of Young's modulus compared to the other samples. This is attributed to the decreased packing density of the particles in presence of adsorbed high molecular weight copolymer molecules.
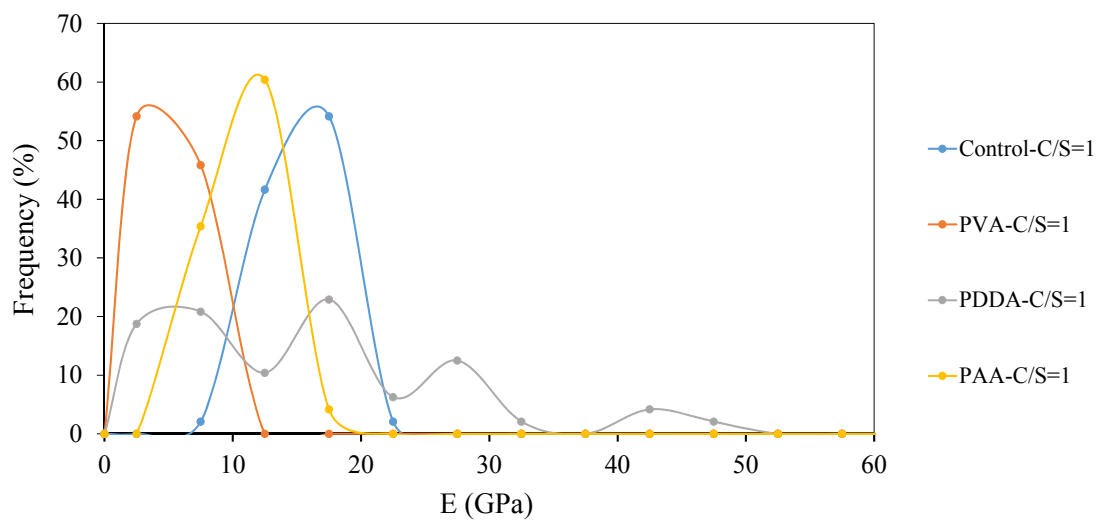
Figure 3.8 Elastic modulus values of the control C-S-H and C-S-H samples modified with polymer at C/S of 1.
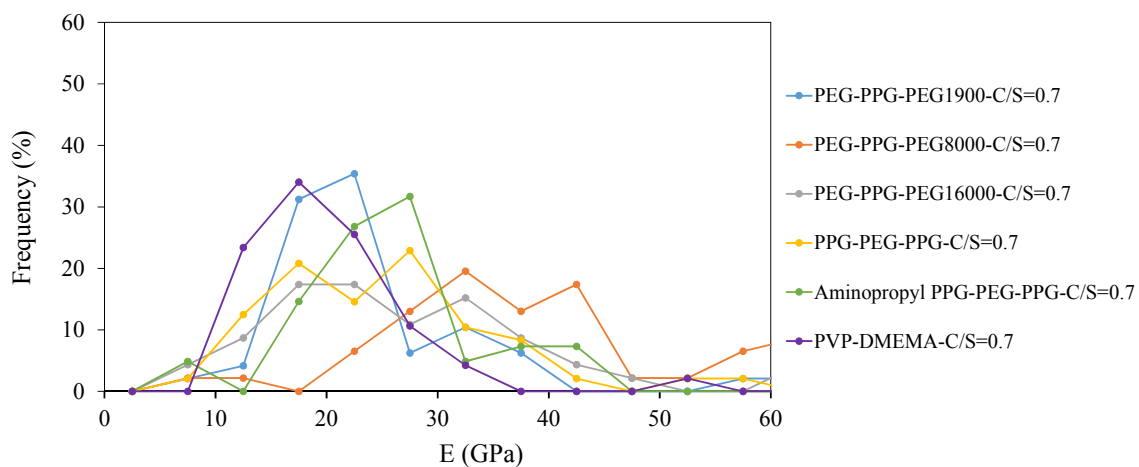
Figure 3.9 Elastic modulus values of the C-S-H samples modified with copolymer at C/S of 0.7.

Chapter 4

4. C-S-H/Biomolecule Composites

Inspired by nature, this chapter investigates the effect of biomolecules, such as amino acids and proteins, on the atomic structure and mechanical stiffness of C-S-H. Amino acids with distinct functional groups, and proteins with different structures and compositions were used in the synthesis of the C-S-H nanocomposite. The atomic structure was examined using XRD and FTIR. The adsorption of biopolymers onto C-S-H particles was examined using TOC measurement. The morphology was investigated using SEM. Atomic AFM nanoindentation was used to evaluate the Young's modulus of modified C-S-H.

4.1. TOC

The percentage of adsorption of amino acids and proteins onto C-S-H measured by TOC are shown in Figure 4.1. The values for glutamic acid and albumin were not valid and thus are not included. It is observed that the amount of adsorption for amino acids is one order of magnitude lower than that of proteins. Amino acids molecules are smaller in size compared to proteins. Therefore at the same concentration of biomolecules, the TOC sample solution of the amino acids contain higher number of biomolecules compared to that of protein samples. This explains the lower amount of adsorption for amino acids. Another potential explanation is that the proteins molecules are comprised of numerous amino acids which provides them with various functional groups and a larger molecular size. This facilitates the adsorption of proteins onto C-S-H particles through multiple binding mechanisms which could result in a higher rate of adsorption for proteins compared to amino acids. The larger size of proteins compared to amino acids could also contribute to increased adsorption of proteins than amino acids. This is supported by previous studies

where larger molecular sized polymers were shown to have a higher adsorption to C-S-H particles compared to polymers with smaller molecular sizes [11].
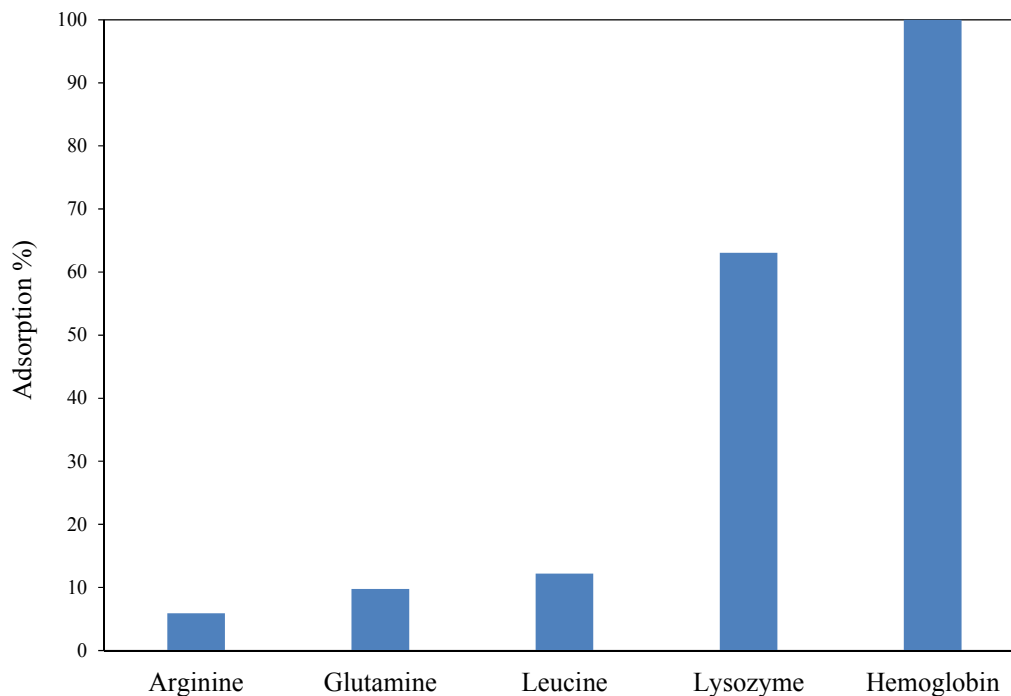
Figure 4.1 Percentage of adsorption of biomolecules onto C-S-H measured by TOC. (The values for glutamic acid and albumin were not valid).

4.2. XRD Results

There are several studies on the stoichiometry of C-S-H, suggesting various models to describe its chemical structure [25,34,35]. It is generally acknowledged that C-S-H does not have a specific chemical formula and stoichiometry [11,13,17,30]. However, C-S-H stacks with their limited lateral extension, follow an ordered structure in localized regions. In this type of structure, the volume fraction of interlayer distance is significantly lower than that of the pores between the C-S-H stacks referred to as gel pores [17]. The XRD spectra for the control C-S-H and C-S-H samples modified with amino acids at a C/S of

0.7 and 1.5 are shown in Figure 4.2a and Figure 4.2b, respectively. The 2θ range of 3º to 10º correspond to the peak of the d_{002} basal spacing reflection. The interlayer distance for all the samples is calculated using Bragg's equation as explained in Chapter 2.

The calculated interlayer distance for different C-S-H samples is shown in Table 4.1. At C/S of 0.7, C-S-H samples modified with arginine (positively charged), leucine (non-polar) and glutamine (H-bond forming) show a broader and less intense peak compared to that of the control sample. In the spectra of arginine and leucine multiple peaks (marked with * in Figure 4.2a) are observed. There is no change in the intensity of the peak in the C-S-H sample modified with glutamic acid. The presence of other peaks at lower angles in addition to the main peak in the spectra of C-S-H samples modified with leucine and arginine can be attributed to a partial intercalation of amino acids between the C-S-H layers increasing the interlayer distance in some of the C-S-H stacks. It is noted that the interlayer distance has slightly increased in the C-S-H samples modified with glutamine which could be attributed to possible adsorption of glutamine between C-S-H layers. It is seen that there is no indication of intercalation in the C-S-H samples modified with glutamic acid (negatively charged) as the interlayer distance has not increased compared to the control sample. This is in general agreement with the results of adsorption using phage display of peptides performed by Picker et al. [66] on C-S-H sample with C/S of 0.66. Based on their results at low C/S, positively charged, polar (H-bond forming) and hydrophobic amino acids adsorb onto the C-S-H. Their study showed that negatively charged amino acids have the lowest adsorption at this C/S ratio. The deprotonated silanol groups of C-S-H with negative surface charges favor the electrostatic interactions with the positively charged

amino acid arginine, H-bond formation with the polar amino acid glutamine and van der Waals interaction with hydrophobic amino acids [66].

The interlayer distance of the control C-S-H sample with C/S of 1.5 is lower than that of the control sample with C/S of 0.7. This is due to the decreased polymerization of silicate chains at higher C/S and is in agreement with previous studies [11,115]. At C/S of 1.5, the C-S-H samples modified with glutamine (H-bond forming) and glutamic acid (negatively charged) show broader peaks compared to that of the control sample. It is seen that the interlayer distance increased in the samples modified with arginine and leucine indicating the intercalation of amino acids in C-S-H. In the C-S-H sample modified with glutamine the interlayer distance has slightly increased compared to the control sample indicating the potential intercalation of glutamine in the interlayer space of C-S-H. In the sample modified with glutamic acid another peak in addition to the main peak appeared at a lower angle. This could imply the intercalation of glutamic acid at this C/S ratio, compared to C/S of 0.7, where no such adsorption was observed. An explanation for the increased influence of negatively charged glutamic acid on the C-S-H structure can be sought in the structural properties of C-S-H. As mentioned previously at low C/S of 0.7, the surface of C-S-H carries negative charges due to the deprotonation of silicate groups; the negatively charged glutamic acid is less likely to interact with C-S-H. With increasing C/S to 1.5, the concentration of Ca^{2+} is increased and as a result, Ca^{2+} bonds to negatively charge surface of C-S-H and shields the surface against positively charged amino acids. In this case, the adsorption of negatively charged amino acid, glutamic acid, onto C-S-H surface is facilitated through bridging with Ca^{2+} [66,147].
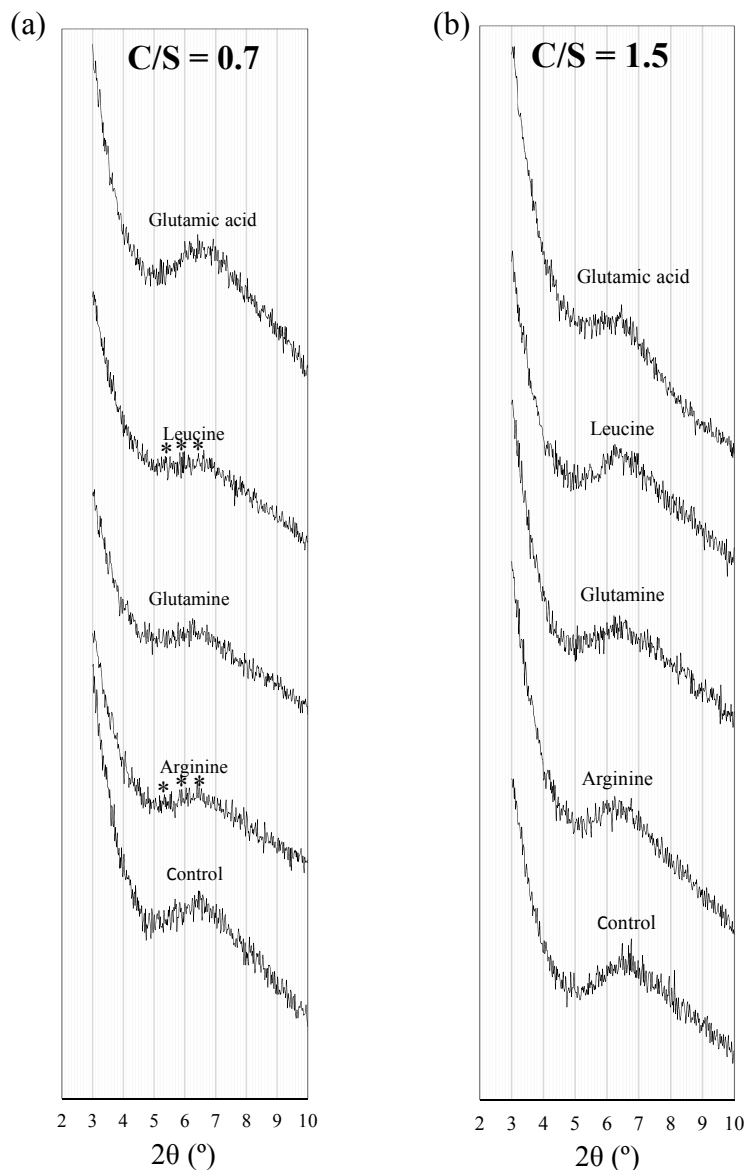
Figure 4.2 XRD spectra of C-S-H modified with the amino acids at C/S of (a) 0.7 and (b) 1.5.

The XRD spectra of the control C-S-H and C-S-H samples modified with different proteins are shown in Figure 4.4a and Figure 4.4b. There is no significant change in the interlayer distance of the samples modified with proteins at C/S of 0.7. The statistical testing to confirm this statement is provided in Table A.1. However, at C/S of 1.5, the peak corresponding to the C-S-H sample modified with lysozyme has broadened and shifted toward lower angles. As shown in Table 4.1 the interlayer distance of the C-S-H samples

modified with lysozyme has increased compared to the control sample. There is not a significant change in intensity of the basal reflection peak and interlayer distance of the samples modified with albumin and hemoglobin. The statistical testing to confirm this statement is provided in Table A.1. The observed influence of lysozyme can be attributed to the specific conformation and composition of this protein.

The pH value of the C-S-H solutions right after mixing was measured to be 11.0 and 10.0 at C/S of 0.7 and 1.5, respectively. The proteins at their stable and active state (called the native state) fold into the most thermodynamically favorable structure and tend to take a globular shape [156]. In this state, the hydrophobic residues tend to be located in the interior of the protein molecules and the hydrophilic residues are exposed at the exterior of the protein molecule. The hydrophobic interaction at the interior and hydrophilic interaction at the exterior are both responsible for stabilizing the protein molecules at their native stage.

	C/S = 0.7		C/S = 1.5	
	2θ	d (Å)	2θ	d (Å)
Control	6.55	13.5	6.6	13.4
Arginine	6.4	13.8	6.2	14.3
Glutamine	6.3	14.1	6.4	13.8
Leucine	6.5	13.6	6.3	14.1
Glutamic acid	6.6	13.4	6.4	13.8
Lysozyme	6.4	13.8	6.2	14.3
Albumin	6.4	13.8	6.5	13.6
Hemoglobin	6.6	13.4	6.5	13.6

Table 4.1 The basal diffraction angle and interlayer distance detected in the XRD spectra of the control C-S-H sample and C-S-H samples modified with biomolecules.

The change in the pH interferes with the stabilizing interactions and forces the protein molecules to unfold [157–161]. A schematic of how the proteins unfold at high pH is shown in Figure 4.3. This makes the hydrophobic residues to become exposed and as a result allows additional mechanisms of interaction through hydrophobic functional groups of the protein molecule and C-S-H. Lysozyme with the highest value of PI can bind to the C-S-H particles with a different mechanism compared to albumin and hemoglobin. The observed influence of lysozyme on the interlayer distance of C-S-H at C/S of 1.5 indicates the specificity of this biomolecule to affect C-S-H. The specificity of biomolecules in their interaction with inorganic surfaces has been observed and studied in prior investigations [162,163]. In albumin and hemoglobin most of the functional groups have deprotonated at the pH level of the C-S-H solution, leaving the structure with a high negative net charge. However, at C/S of 1.5 where the pH of the freshly mixed solution is around 10, lysozyme with a PI value of 10.6 can adsorb onto the forming C-S-H particles with the un-deprotonated functional groups.
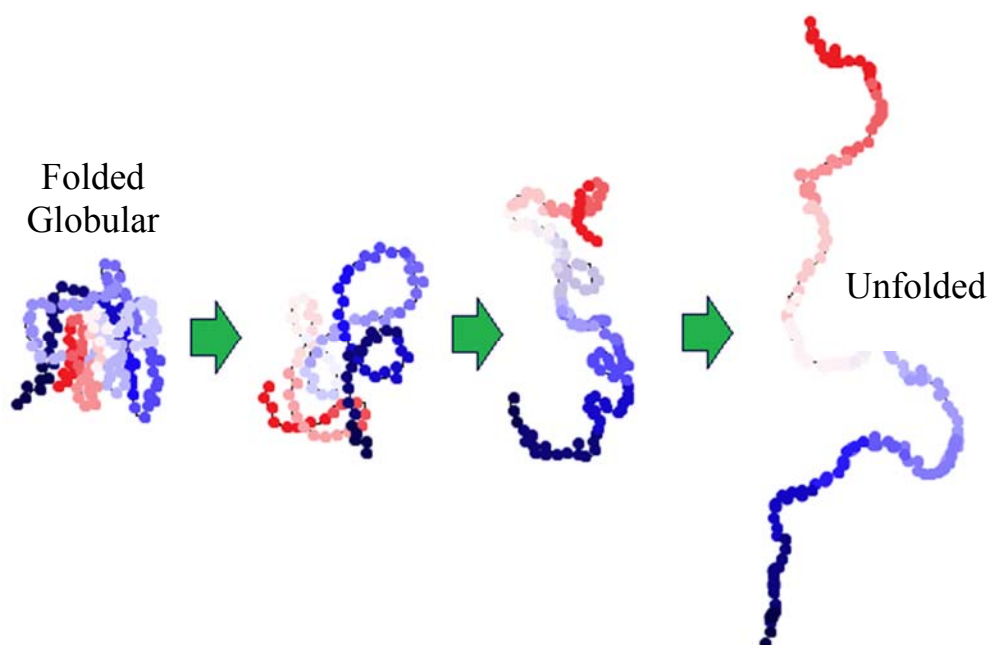
Figure 4.3 Schematic of how proteins undergo conformational changes with increasing pH
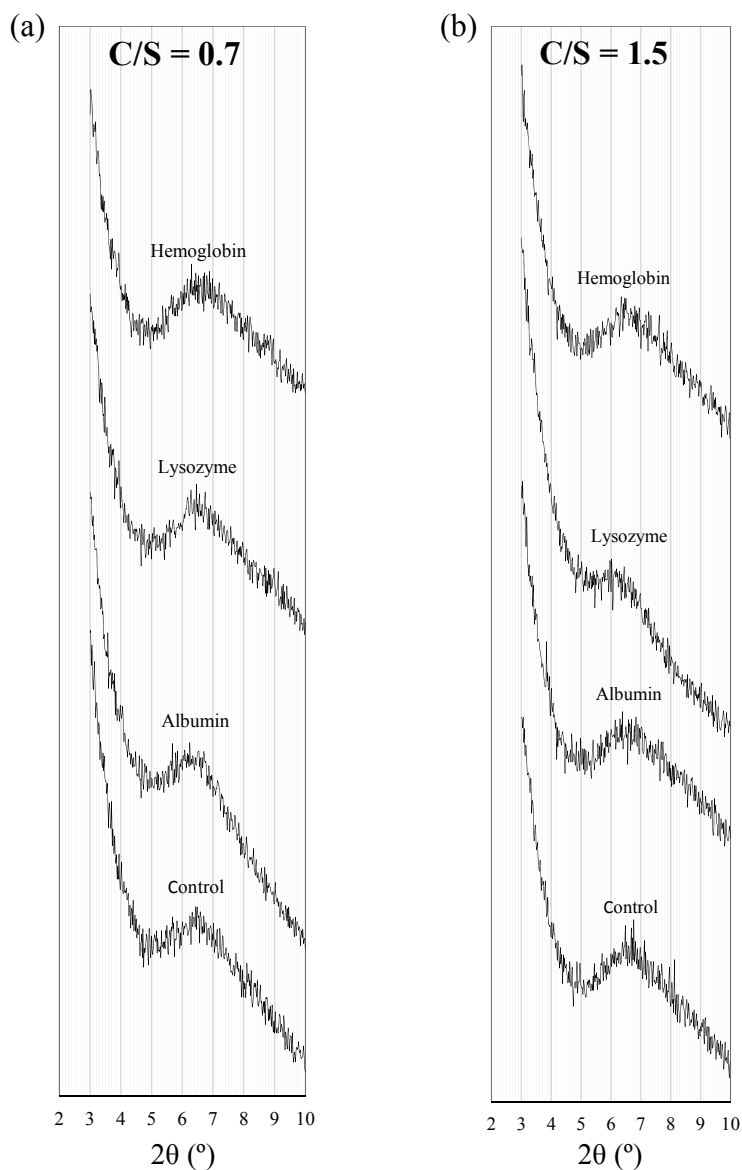
Figure 4.4 XRD spectra of C-S-H modified with the proteins at C/S of (a) 0.7 and (b) 1.5.

4.3. FTIR Results

The FTIR spectra for the control C-S-H and C-S-H samples modified with amino acids and proteins at C/S of 0.7 and 1.5 are shown in Figure 4.5 and Figure 4.6, respectively. The frequencies of the Si-O stretching vibrations of the Q^1 and Q^2 tetrahedra for different C-S-H samples are listed in Table 4.2. Q^1 represents the end silicate tetrahedra and Q^2

corresponds to the bridging silicate tetrahedra. The intensity ratio of Q^2 to Q^1 is a measure of polymerization of silicate chains in C-S-H and is shown in Table 4.2.

It is observed that the location of the Q^2 band is shifted towards higher frequencies in the control sample with a reduction in C/S. This is an indication of increased polymerization in the control sample with a C/S of 0.7 compared to the sample with C/S of 1.5 as it is also evident from the higher intensity ratio of Q^2 to Q^1 at the lower C/S ratio [16,119]. It is seen that the location of the Q^2 band in arginine sample at C/S of 0.7 is lower than that of the control C-S-H, suggesting a reduction in polymerization as a result of interaction between arginine and C-S-H at this C/S ratio. The intensity ratio of Q^2/Q^1 in the sample modified with arginine is also lower than that of the control C-S-H. The Q^2 peak frequency of the C-S-H with other amino acids except arginine did not change at C/S of 0.7. At C/S of 1.5, the Q^2 peak of arginine shows a similar frequency to the control C-S-H. It is interesting to note the shift to higher frequencies of Q^2 in the C-S-H modified with glutamic acid at this C/S ratio, which indicates the interaction of glutamic acid with C-S-H and maybe the increased polymerization in C-S-H modified with glutamic acid; however the intensity ratio Q^2/Q^1 appears to remain unchanged in this sample. The reduction in the influence of arginine and an increase in influence of glutamic acid with increasing C/S ratio is consistent with the XRD results discussed earlier.

In the samples modified with proteins, at C/S of 0.7 there is a shift to lower frequencies in the Q^2 peak of the C-S-H modified with hemoglobin. The corresponding Q^2 peak frequency of the C-S-H modified with albumin and lysozyme is unchanged. With increasing C/S from 0.7 to 1.5 the Si-O stretching band corresponding to Q^2 shifted to higher frequencies in C-S-H samples modified with proteins. This trend is not similar to

that of the control C-S-H sample and C-S-H modified with amino acids. One explanation is the calcium binding effect of proteins. The proteins can bind the added calcium ions so the actual C/S ratio is lower than what is expected [12,164]. To investigate the calcium binding effect of proteins, electrical resistivity measurement was utilized. The binding between proteins and Ca^{2+} reduces the concentration of free Ca^{2+} in the solution, which results in an increase in electrical resistivity of the solution. A solution of 0.2 gr of each protein in 40 ml of DI water was prepared. The pH of the solution was increased by adding a 5 M NaOH solution to account for the effect of high pH on the interaction between the proteins and Ca^{2+}. Required amounts of a 4.7 M solution of $CaCl_2$ solution was added to the protein solutions to obtain solutions with calcium ion concentrations of 0.35 M and 0.7 M which approximately represent the concentration of Ca^{2+} in prepared solutions of C-S-H with C/S of 0.7 and 1.5. Control solutions of calcium chloride were also prepared for comparison. Two electrodes consisting of stainless steel strips with a width of 10 mm were inserted inside a glass beaker with a dimeter of 25 mm. In each measurement 10 ml of the solution was placed in the beaker. The electrical resistivity of the solution was measured using a Reference Gamry 600 potentiostat/galvanostat with a 20 mV AC signal and a frequency range of 10^6 to 10 Hz. The electrical resistivity of 0.35 M and 0.70 M solutions of Ca^{2+} with and without proteins are shown is Table 4.3. The difference between the electrical resistivity values of the control solution and the solution with the proteins is less than 8%. This observation may be used to hint that the Ca^{2+} binding effect of the proteins used in this study is not significant. The second explanation for the notable shift in the Q^2 frequencies of C-S-H with all proteins at C/S of 1.5 could be the incomplete nucleation of C-S-H particles at C/S of 1.5. Consequently, the solution has a high content of unreacted

silicate gel and surface adsorbed proteins [147]. The presence of the bands corresponding to amide I and amide II at around 1640 cm^{-1} and 1530 cm^{-1} respectively, indicates the high content of protein in the modified C-S-H samples [165,166]. The shift in the Q^2 frequencies of C-S-H with all proteins, can also be viewed as an indication of increased polymerization in the C-S-H samples and suggest the influence of the proteins on silicate polymerization of C-S-H. While the influence of lysozyme on C-S-H is also observed from the XRD results, such an influence of albumin and hemoglobin on C-S-H structure is not evident from the XRD analysis.

	C/S = 0.7			C/S = 1.5		
	Q^2 (cm^{-1})	Q^1 (cm^{-1})	Q^2 / Q^1	Q^2 (cm^{-1})	Q^1 (cm^{-1})	Q^2 / Q^1
Control	1004	778	3.70	999	777.5	3.58
Arginine	999.5	779.5	3.55	999.5	777	3.51
Glutamine	1003	782.5	3.77	999.5	777.5	3.42
Leucine	1004	781	3.85	999.5	777.5	3.41
Glutamic acid	1003.5	781.5	3.57	1004	780	3.46
Lysozyme	1003	779	3.59	1008	775	3.62
Albumin	1003	779	3.7	1015.5	775.5	3.68
Hemoglobin	999	779	3.41	1004	776.5	3.44

Table 4.2 The wavelength numbers corresponding to Q^2 and Q^1 silicates in the FTIR spectra of the control and modified C-S-H powders.

	Control	Lysozyme	Albumin	Hemoglobin
0.35 M Ca^{2+}	23.6	23.1	23.1	25.1
0.70 M Ca^{2+}	13.8	13.8	14.1	14.9

Table 4.3 The electrical resistivity (Ω) of 0.35 M and 0.70 M solutions of Ca^{2+} with and without proteins.
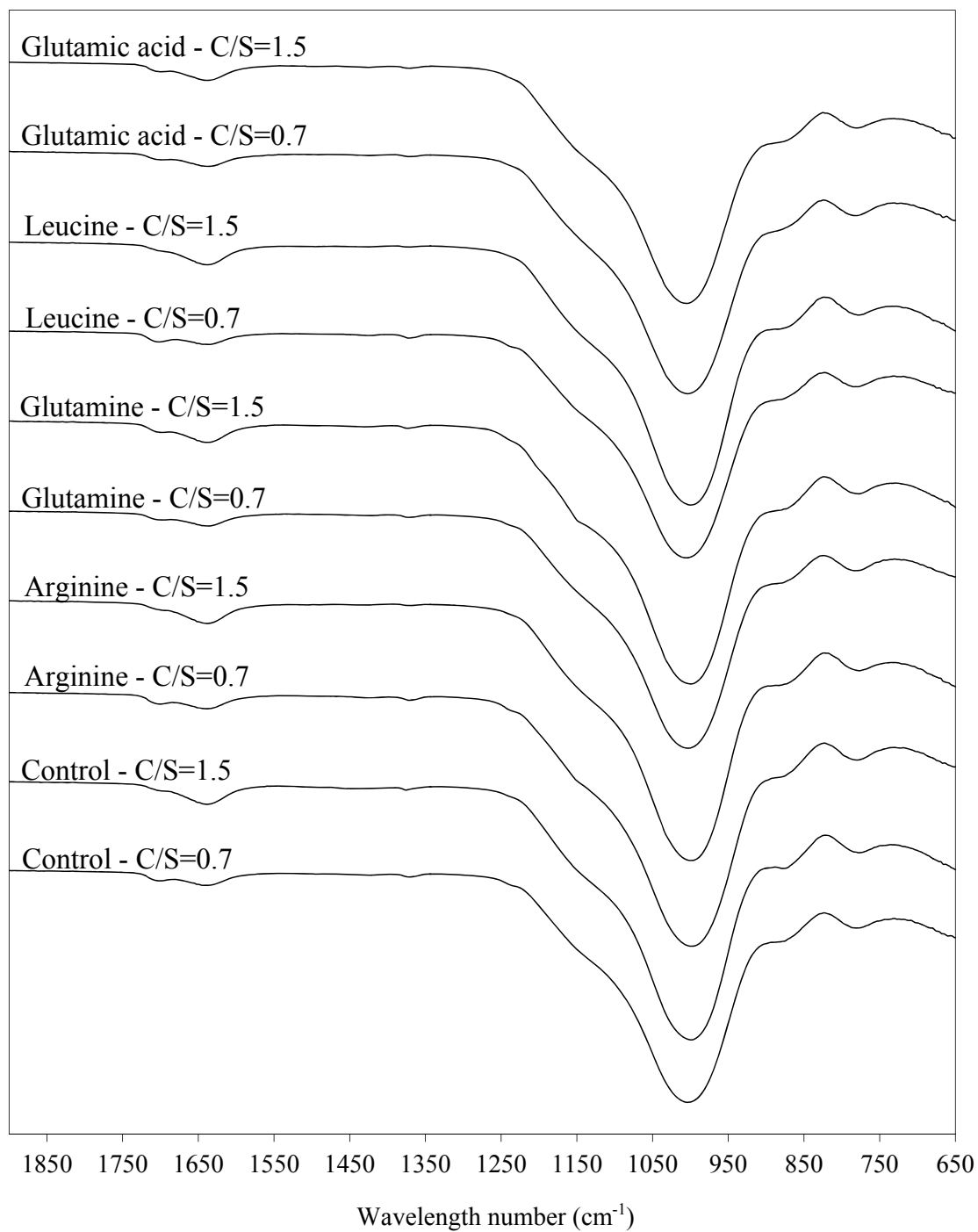
Figure 4.5 FTIR spectra of the C-S-H samples modified with amino acids.

Hemoglobin - C/S=1.5

Hemoglobin - C/S=0.7

Lysozyme - C/S=1.5

Lysozyme - C/S=0.7

Albumin - C/S=1.5

Albumin - C/S=0.7

Control - C/S=1.5

Control - C/S=0.7

1850 1750 1650 1550 1450 1350 1250 1150 1050 950 850 750 650

Wavelength number (cm^{-1})
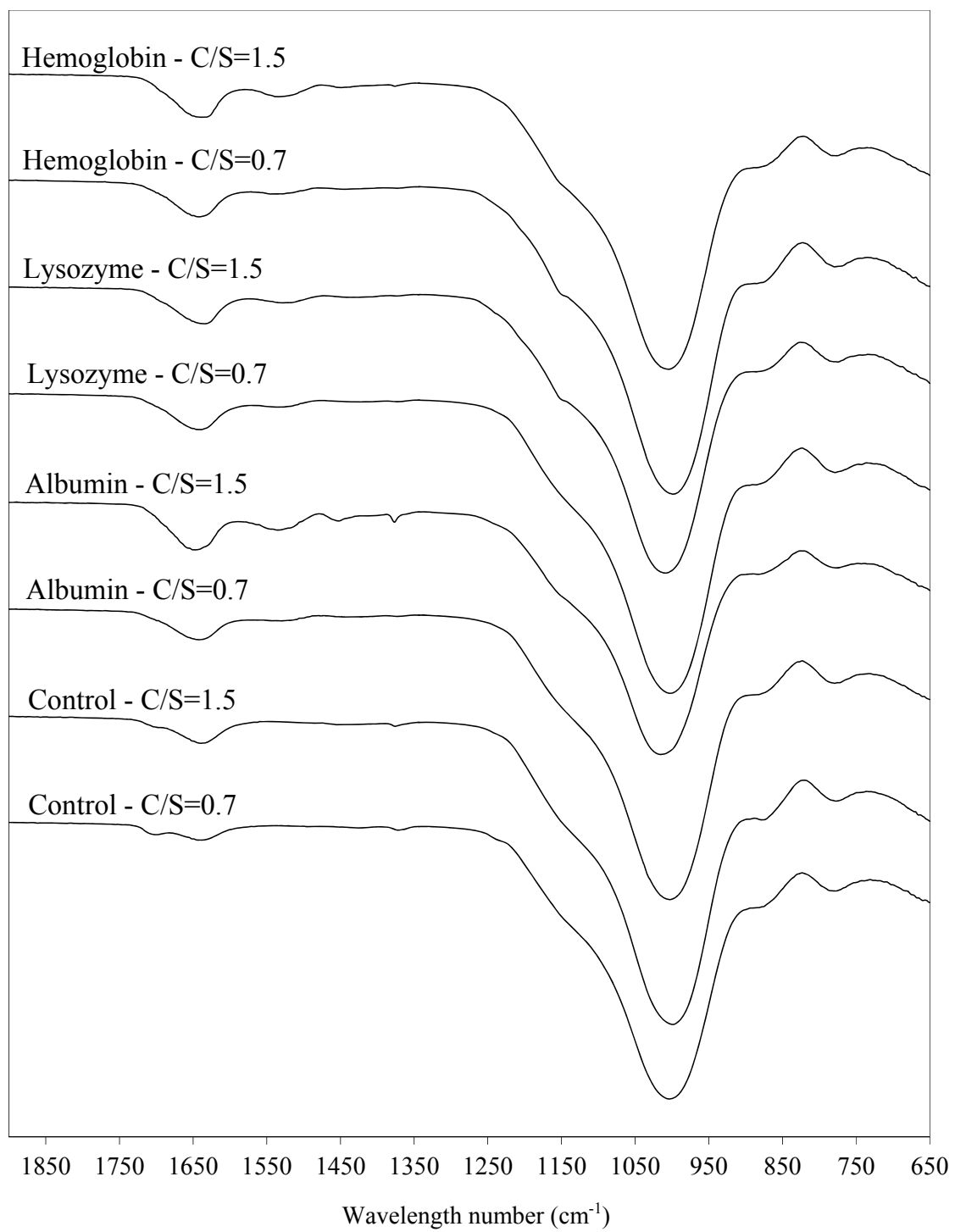
Figure 4.6 FTIR spectra of the C-S-H samples modified with proteins.

4.4. Morphology

The SEM images of the control C-S-H and C-S-H samples modified with arginine, glutamine, leucine and glutamic acid at C/S of 0.7 are shown in Figure 4.7. There is no noticeable difference in the morphology of the control sample and the C-S-H samples modified with amino acids as seen from SEM images. The globular morphology with a size of 20 nm to 100 nm can be observed in all C-S-H samples, which is in agreement with the previous studies [25,167].

The SEM images of the C-S-H samples modified with albumin, lysozyme and hemoglobin at C/S of 0.7 and 1.5 are shown in Figure 4.8. The morphology of the albumin and lysozyme modified C-S-H is comparable to the control sample. The C-S-H sample modified with hemoglobin at both C/S ratios showed a slightly different morphology. The C-S-H particles in these samples are observed to exhibit a platelet morphology. In this structure, the network is built of pores and building blocks of nano-platelets. This type of structure has been previously observed by researchers in hierarchically nanostructures mesoporous spheres of C-S-H [168]. An agglomerated C-S-H particle of the sample modified with hemoglobin at C/S of 0.7 is shown in Figure 4.9. The stacks of nanosheets constructing the C-S-H network are clearly observed in the agglomerated sample. Considering the fractal morphology and the arrangement of C-S-H structure in several hierarchical levels [169–173], the bird-nest structure of the agglomerated C-S-H particle can confirm the morphology of C-S-H particles in smaller scale.
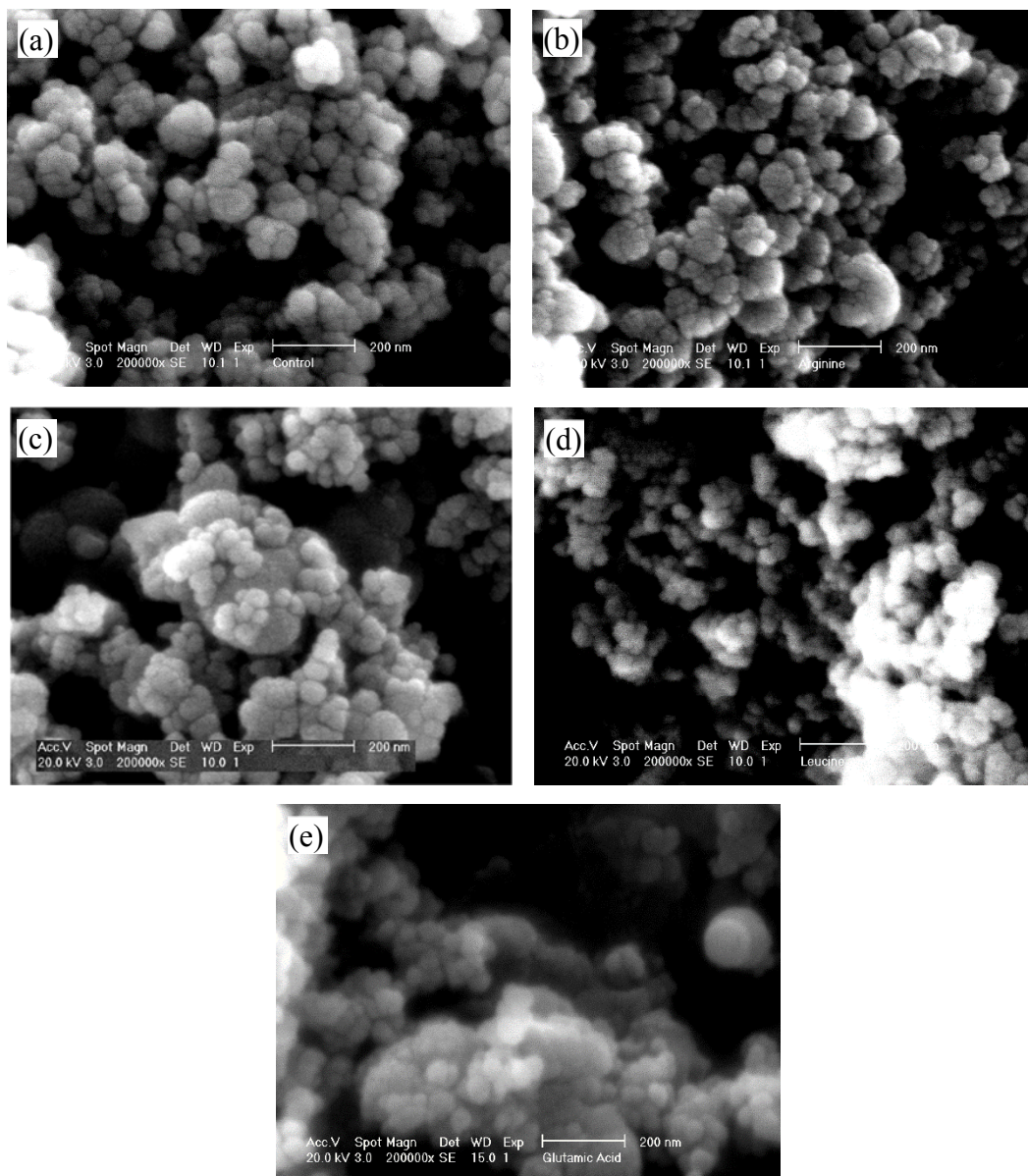
Figure 4.7 The morphology of the (a) control and modified C-S-H with (b) arginine, (c) glutamine, (d) leucine and (e) glutamic acid at C/S of 0.7.
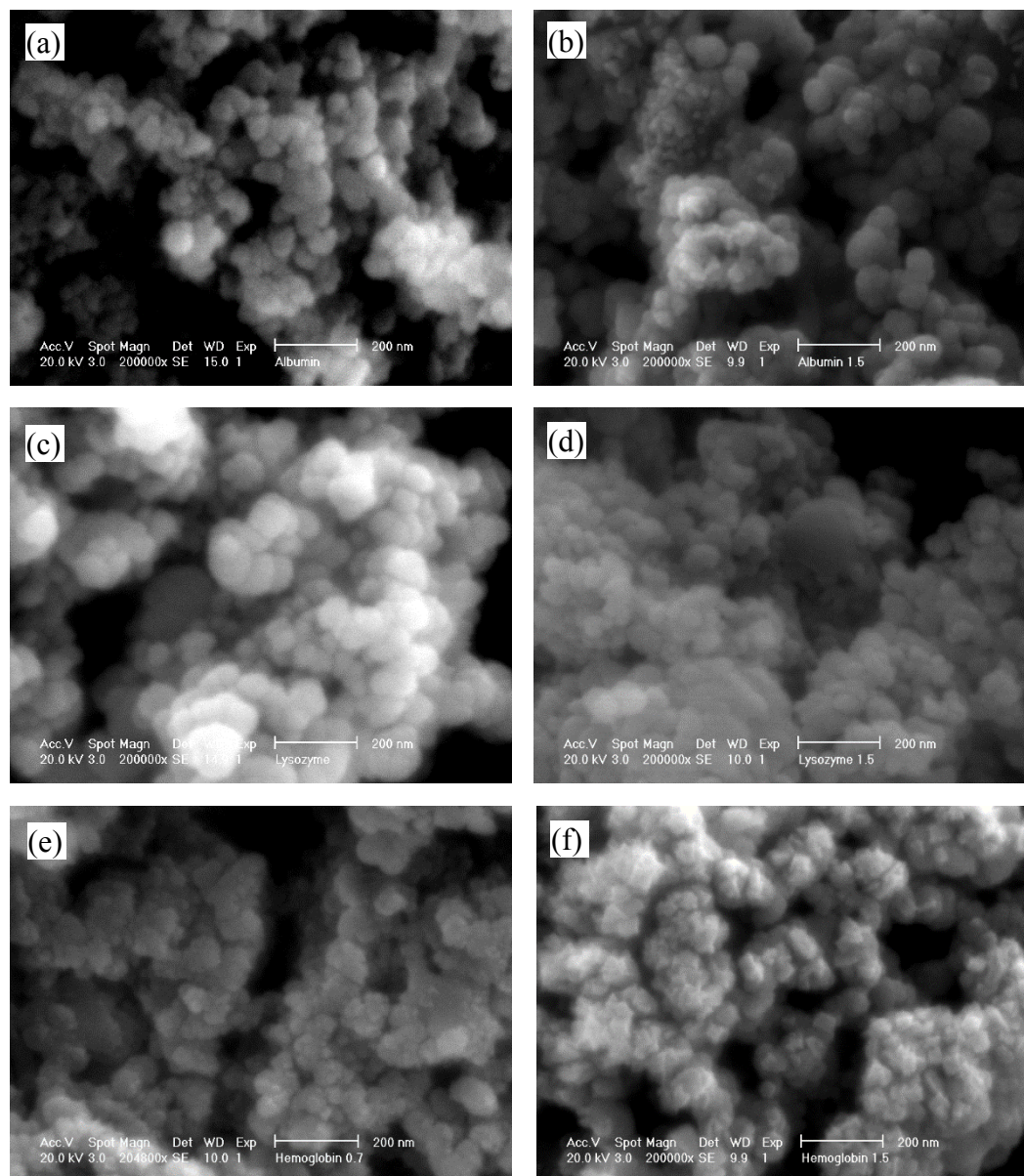
Figure 4.8 The morphology of the modified C-S-H with (a) albumin at C/S 0f 0.7, (b) albumin at C/S of 1.5, (c) lysozyme at C/S of 0.7, (d) lysozyme at C/S of 1.5, (e) hemoglobin at C/S of 0.7 and (f) hemoglobin at C/S of 1.5.
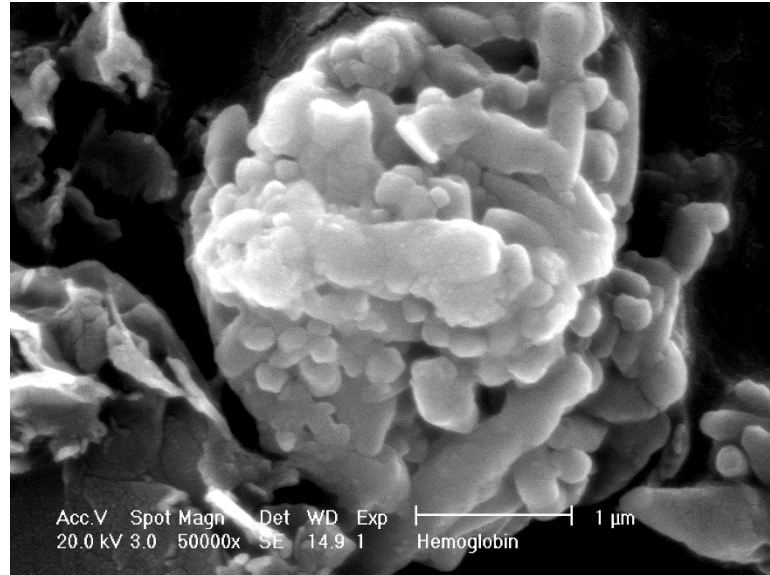
Figure 4.9 An agglomerated C-S-H particle in the C-S-H sample modified with hemoglobin at C/S of 0.7.

4.5. Mechanical Properties

The elastic modulus measurements of the control C-S-H and C-S-H samples modified with amino acids at C/S of 0.7 and 1.5 are shown in Figure 4.10a and Figure 4.10b. Comparing the elastic modulus value of the control samples with C/S of 0.7 and 1.5, it is noted that no significant difference can be observed. Excluding the values more than 45 GPa which is attributed to calcium hydroxide [44], an average Young's modulus of 24.9±1.9 GPa for the control C-S-H with C/S of 0.7 and 25.2±1.9 GPa for the control C-S-H samples with C/S of 1.5 was obtained. These values are consistent with the values obtained in previous studies [154,155,174]. It is shown by Beaudoin and Feldman [153] that the intrinsic elastic properties of C-S-H are not dependent on the C/S ratio. This indicates that the decrease in the Young's modulus of C-S-H, observed in nanoindentation test results, is because of an increase in the packing density of C-S-H [154].

At C/S of 0.7, the C-S-H modified with arginine, leucine and glutamic acid showed lower values of Young's modulus compared to that of the control sample. The decrease in the value of Young's modulus may be due to the presence of these amino acids adsorbed on the surface or in the voids between the C-S-H particles resulting in a lower packing of C-S-H sample compared to the control C-S-H sample [15,19]. However, no noticeable change was observed in the sample modified with glutamine. At C/S of 1.5, all the samples modified with amino acids have average values comparable to that of control sample. However, the arginine sample has its higher intensity peak at lower values compared to the other samples potentially related to a reduction in the packing density in C-S-H modified with arginine.

The elastic modulus values of the control C-S-H and C-S-H samples modified with proteins at C/S of 0.7 and 1.5 are shown in Figure 4.11a and Figure 4.11b. At C/S of 0.7, the C-S-H modified with lysozyme is comparable to the control sample. However, albumin and hemoglobin showed lower values of Young's modulus compared to that of the control sample.

At C/S of 1.5, all the C-S-H samples modified with proteins had lower values of Young's modulus compared to that of the control sample. In addition, the Young's modulus of C-S-H with proteins seems to be slightly lower at C/S of 1.5 than at C/S of 0.7. This can be related to a change in silicate polymerization of C-S-H, as seen from the FTIR results shown in Figure 4.6, as well as a change at the mesoscale in terms of increased occupation of gel pores by the proteins thereby reducing packing density of C-S-H. It is noted that the sample modified with lysozyme has still higher values of Young's modulus compared to samples modified with albumin and hemoglobin at C/S of 1.5.
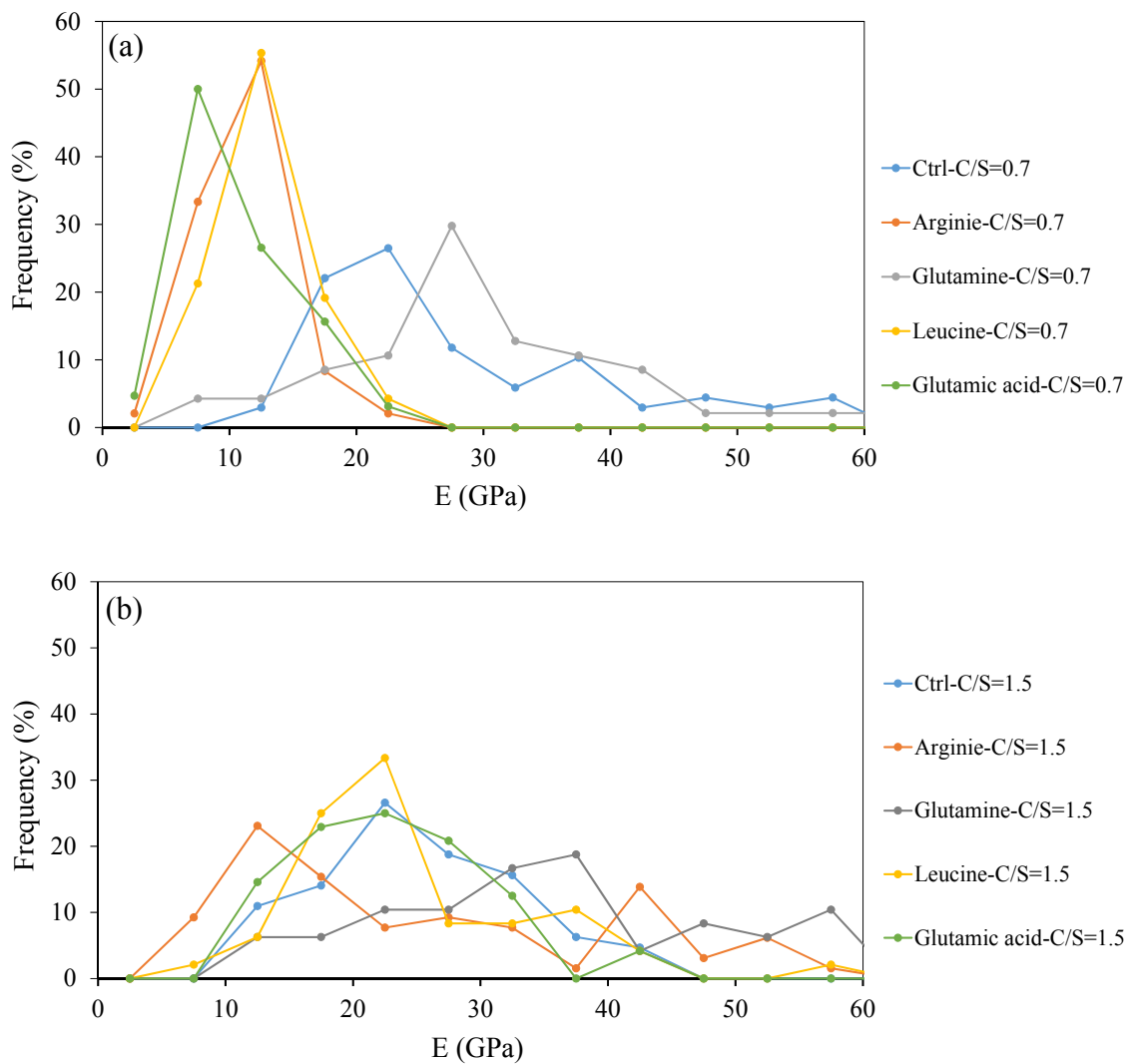
Figure 4.10 Elastic modulus values of the control C-S-H and C-S-H samples modified with amino acids at (a) C/S of 0.7 and (b) C/S of 1.5.
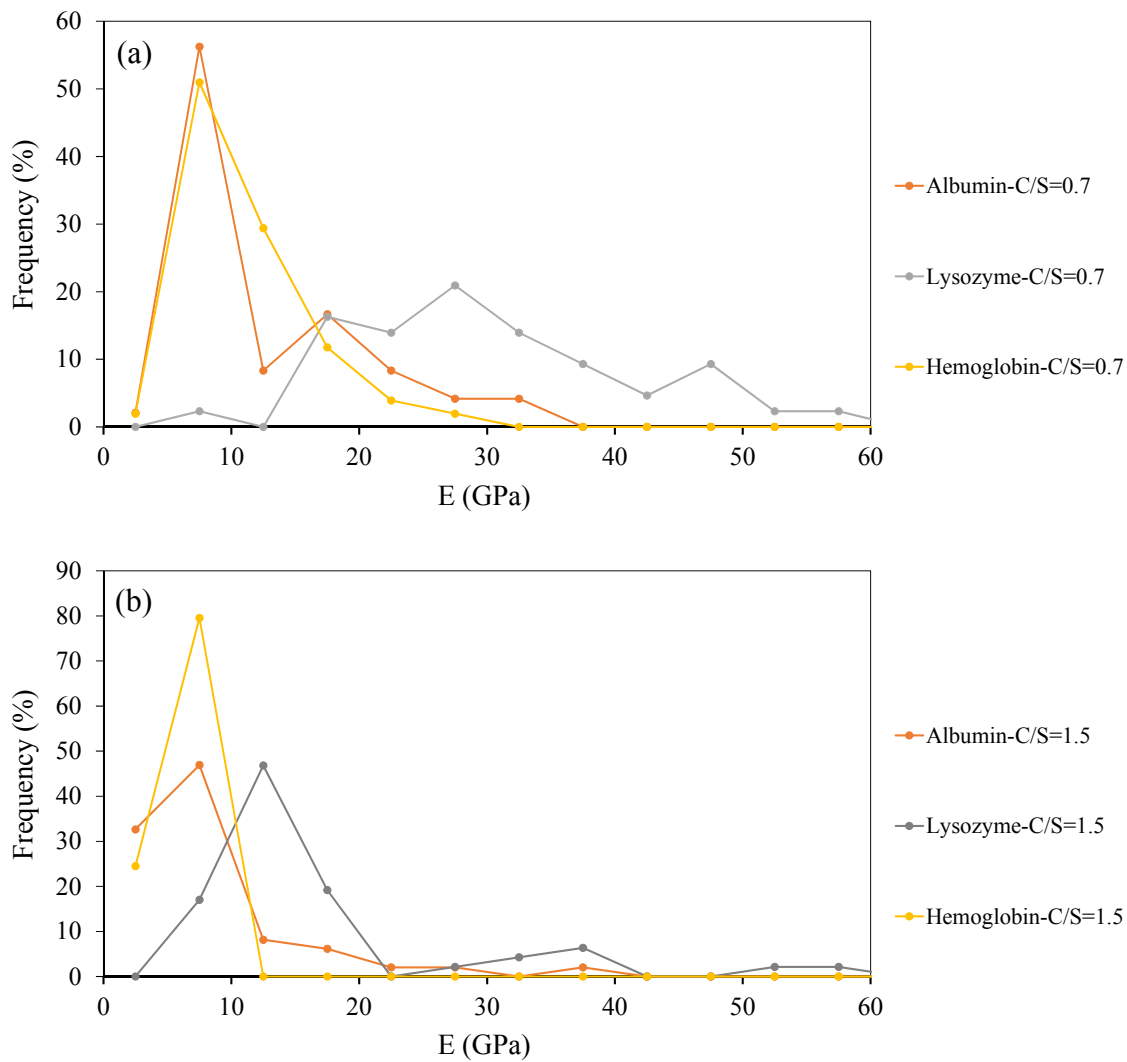
Figure 4.11 Elastic modulus values of the control C-S-H and C-S-H samples modified with proteins at (a) C/S of 0.7 and (b) C/S of 1.5.

Chapter 5

5. Layer By Layer Fabrication of C-S-H/Polymer Composites

In this chapter, C-S-H/polyelectrolyte nanocomposites were synthesized with the layer-by-layer (LBL) method and their morphology and mechanical properties were investigated using AFM imaging and AFM nanoindentation. Different sets of polymers were used to produce C-S-H/polyelectrolytes nanocomposites. Effect of different factors including dipping time, C to S ratio and pH on the properties and structure of the nanocomposite was also investigated. To further elucidate the possibility of improving nucleation of C-S-H and mechanical properties of the composite, GO nanosheets were used in the LBL assembly. The list of the samples and their consisting polymers, dipping time, C/S ratio and calcium salt concentration are included in Table 5.1.

5.1. Characterization

According to Guo et al. [99], during the LBL process, calcium and silicate ions in polymer solutions meet each other and form C-S-H. The C-S-H particles formed in each layer define the morphology of the surface [98,99]. The morphology obtained during LBL assembly is compared with C-S-H particles grown on a calcite substrate as is shown in Figure 5.1. A freshly cleaved calcite crystal was immersed in a sodium silicate solution for one week to obtain a surface covered with C-S-H particles [175,176]. The AFM scans of the calcite substrate at early stages of formation of C-S-H and after growth of C-S-H particles is shown in Figure 5.1a, Figure 5.1b, Figure 5.1c and Figure 5.1d, respectively. The AFM scan of the PEI/PSS-20 sample made of 3 bilayers is shown in Figure 5.1e and Figure 5.1f. In both samples C-S-H particles can be identified with their globular shape. In the sample grown on calcite, the aggregation has occurred during a longer period of time.

Thus, it is evident that the C-S-H particles in this system are larger in size compared to the

C-S-H particle formed during the short duration of LBL assembly. The size of the particles

in the LBL sample is about 20-50 nm which is in line with the previous studies [99].

Sample label	Positive polymer	Negative polymer	Positive (complex) solution dipping time (min)	Negative (complex) solution dipping time (min)	C/S	Calcium acetate concentration in positive complex solution (M)
PEI/PSS-Polymer	PEI	PSS	20	20	-	-
PEI/PSS-10	PEI	PSS	10	20	1	0.0514
PEI/PSS-20	PEI	PSS	20	20	1	0.0514
PEI/PSS-40	PEI	PSS	40	20	1	0.0514
PEI/PSS-Ca0.00514	PEI	PSS	20	20	1	0.00514
PEI/PSS-Ca0.1028	PEI	PSS	20	20	1	0.1028
PEI/PSS-0.7	PEI	PSS	20	20	0.7	0.0514
PEI/PSS-1.5	PEI	PSS	20	20	1.5	0.0514
PEI/PSS-2.3	PEI	PSS	20	20	2.3	0.0514
PDDA/PAA-Polymer	PDDA	PAA	20	20	-	-
PDDA/PAA-10	PDDA	PAA	10	20	1	0.0514
PDDA/PAA-20	PDDA	PAA	20	20	1	0.0514
PDDA/PAA-40	PDDA	PAA	40	20	1	0.0514
PDDA/PAA-HighpH	PDDA	PAA	20	20	1	0.0514
PEI/PAA-Polymer	PEI	PAA	20	20	-	-
PEI/PAA-20	PEI	PAA	20	20	1	0.0514
PEI/PSS-GO	PEI	PSS	20	20	1	0.0514

Table 5.1 List of the samples and their consisting polymers, dipping time, C/S and calcium salt concentration.
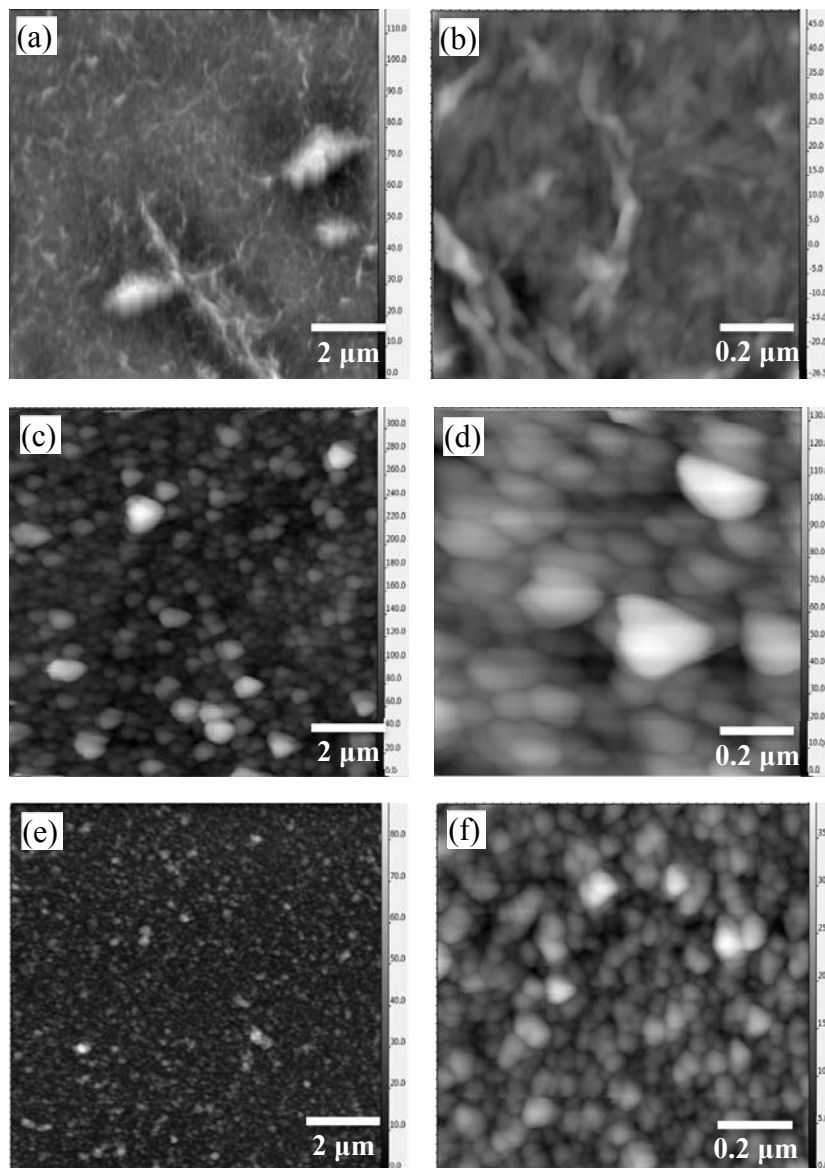
Figure 5.1 AFM scans of the (a), (b) calcite substrate in early stages of exposure to sodium silicate solution, (c), (d) C-S-H particles grown on the calcite substrate after a week of exposure to sodium silicate solution, (e) and (f) C-S-H particles formed on PEI/PSS-20 samples after assembling 3 bilayers using LBL method.

The formation of C-S-H particles during the LBL assembly was further confirmed using XRD as shown in Figure 5.2. Three bilayers of PEI/PSS-20 sample were assembled on a silicon wafer prepared with the same method explained for glass slide. Silicon wafer was used because of its smoother surface compared to glass slide so the amount of noise

was reduced significantly and the thin layer of C-S-H was detected by XRD. The peak

corresponding to C-S-H can be observed at 29.1° [115] indicating the formation of C-S-H

in the nanocomposite. It should be noted, according to available literature, the XRD

spectrum of C-S-H exhibits other peaks with the strongest peak typically occurring at 29.1°

[177]. Due to very thin layer of C-S-H/polymer, other peaks are not evident in the XRD

spectrum shown in Figure 5.2.
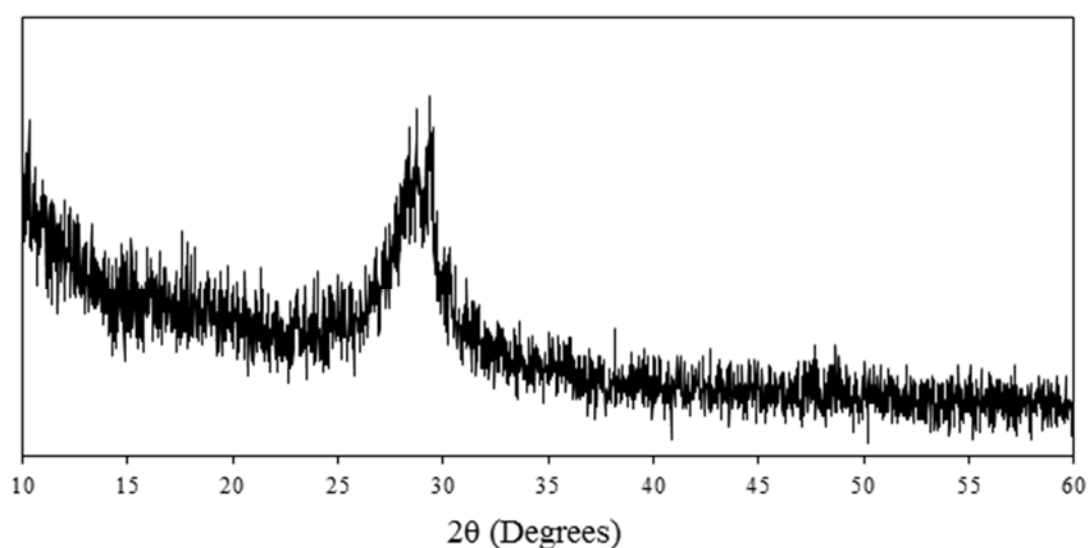
Figure 5.2 XRD spectrum of the PEI/PSS-20 sample with 3 bilayers assembled on a silicon wafer substrate.

The FTIR scans for the hydrolyzed PAN substrate and PEI/PSS-20 sample after

assembling each bilayer are shown in Figure 5.3. The O-H band at 3390 cm^{-1} and C=O

band at 1632 cm^{-1} in hydrolyzed PAN decreased in intensity as more layers were assembled

on the sample. The C-H band of polymers at 2980 cm^{-1} and the band at 1178 cm^{-1}

corresponding to sulfonate moiety of PSS [98] appeared after depositing the first bilayer

and increased in intensity as the number of layers increased. The peak at 968 cm^{-1} is

detectable after assembling the second bilayer and increased in intensity by assembling the

third bilayer. This peak corresponds to Si-O stretching band in C-S-H [119] and indicates

the increased formation of C-S-H particles as the number of bilayers increased. The peak at 1071 cm^{-1} in hydrolyzed PAN is attributed to the blending vibration of C-N group [178]. It is observed that the broad peak in 1000-1200 cm^{-1} region which is the characteristic absorption band of Si-O-Si asymmetric stretching [179] increased by increasing the number of layers which provides evidence for the formation of C-S-H in the sample.
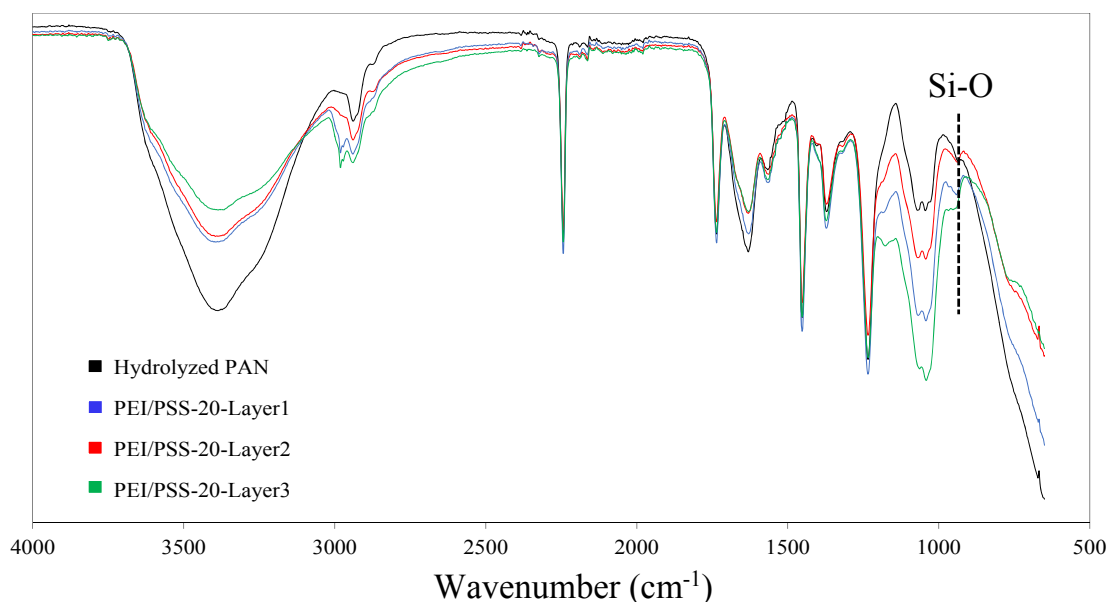
Figure 5.3 FTIR spectra of the PEI/PSS-20 samples with 3 bilayers assembled on a hydrolyzed PAN substrate after assembling of each bilayer.

The pH, zeta potential value and size of the polymers and polymer/ion solutions are shown in Table 5.2.The concentration of polymers and salts in these solutions was the same as that of the solutions used to prepare the PEI/PSS-20 and PDDA/PAA-20 samples. Solutions containing C-S-H nanoparticles were also made by mixing equal amount of positively charged and negatively charged polyelectrolyte complex solutions and their pH, zeta potential and size were measured. It is seen that the solution of PEI-Ca^{2+} and PSS-SiO$_3$$^{2-}$ have a zeta potential of 10 mV and -42.9 mV indicating the positive and negative

charge of the polymer solution after addition of salts, respectively. By mixing the PEI-Ca^{2+} and PSS-SO$_3^{2-}$ solutions, the size of the particles was increased to 205 nm which indicates the formation of C-S-H nanoparticles in the aqueous solution. The charge of PEI/PSS/CSH solution is seen to be negative and slightly lower than that of PSS- SO$_3^{2-}$ due to strong anionic character of PSS. The size of particles in PEI/PSS/CSH is also larger than that of PEI/PSS without Ca^{2+} or SO$_3^{2-}$, which provides evidence for agglomeration of C-S-H particles in this solution. The negative charge of the particles in PEI/PSS/CSH was measured to be higher than that of PEI/PSS; this indicates the negative charge of the silicate chains in C-S-H formed in-situ during LBL deposition.

	pH	Zeta potential (mV)	Size (nm)
PEI	10.1	19.1	96.8
PEI-Ca^{2+}	10.5	10	85.7
PSS	8.4	-34.8	110
PSS-SO$_3^{2-}$	11.7	-42.9	63.4
PEI/PSS	10.5	-28.3	60.9
PEI/PSS/CSH	10.8	-39.3	205
PDDA	9.8	51.8	431.4
PDDA-Ca^{2+}	8.7	44	482.7
PAA	3.8	-16.5	59.6
PAA- SO$_3^{2-}$	11.5	-53.5	20.1
PDDA/PAA	2.9	70.4	323.9
PDDA/PAA/CSH	10.1	-15.4	?

Table 5.2 pH, Zeta potential value and size of the polymers and polymer/ion solutions.

The device was not able to measure the size of particles after mixing the PDDA-Ca^{2+} and PAA-SO$_3^{2-}$ solutions. This might be because of formation of large agglomerated C-S-H particles. It is noted that the agglomerated particles were clearly observed in the mixed

solution. The large size of particles in PDDA/PAA/CSH could be partially due to the large

molecule size of PDDA. The charge of particles in PDDA/PAA/CSH is also negative.

5.2. Morphology Examination

The AFM images of PEI/PSS-Polymer, PDDA/PAA-Polymer and PEI/PAA-Polymer

samples are shown in Figure 5.4a, Figure 5.4b and Figure 5.4c, respectively. Figure 5.4d,

Figure 5.4e and Figure 5.4f show the AFM scans of the PEI/PSS-20, PDDA/PAA-20 and

PEI/PAA-20 samples. The LBL assembly of different sets of polymers revealed different

types of morphologies. However, when Ca^{2+} and SiO_3^{2-} ions were added to the different

polymer sets in order to facilitate C-S-H formation, globular features were detected in all

the samples. The size and density of these globules were different in the samples. The

roughness values of the samples are shown in Table 5.3. Globules in PDDA/PAA-20

sample were smaller and denser compared to the other samples and the roughness value

was also the smallest among the samples. Globules in the PEI/PAA-20 sample appeared

larger, which is also reflected in increased roughness value of the sample. These

observations indicate the important role of the different polyelectrolytes on the formation,

growth, and assembly of C-S-H globules. One explanation for this observation can be

related to the conformation of polymers molecules in the layered structure of the samples.

In PDDA/PAA-20, the polymer molecules adopt a flat conformation and provide a

template for growth and assembly of C-S-H particles. This can be attributed to the strong

cationic PDDA, which maintains high positive charge density even at pH of the solution,

which is measured to be 10 to 11. On the other hand, PEI is a weak cationic polymer and

is partially charged at the pH of the solutions and it adopts a coil like conformation. Thus,

it is expected that the growth and assembly of C-S-H in the coil like template results in a

larger C-S-H aggregate and increased porosity and less packing density of the nanocomposites, as demonstrated by increased roughness in PEI/PSS-20 and PEI/PAA-20 samples. It is seen that the roughness of PEI/PSS-Polymer and PEI/PAA-Polymer is lower than that of PEI/PSS-20 and PEI/PAA-20, respectively. It is interesting to note an opposite trend in the case of PDDA and PAA, where there is a reduction in roughness in PDDA/PAA-20. PAA is a weak electrolyte and is partially ionized below a pH of 6.5 [180]. Thus, at pH of 2.9, which corresponds to the solution of PDDA and PAA, its molecular structure consists of segmental population of loops and tails at this pH [180]. Thus, this promotes formation of large island like features on the surface of the PDDA/PAA-Polymer sample, which also leads to elevated roughness, as seen in Table 5.3.

Sample label	R_a (nm) 5 μm × 5 μm	R_a (nm) 1 μm × 1 μm
PEI/PSS-Polymer	1.47	1.18
PEI/PSS-20	4.77	4.1
PDDA/PAA-Polymer	7.95	6.85
PDDA/PAA-20	0.85	0.873
PEI/PAA-Polymer	8.12	9.75
PEI/PAA-20	23.2	19.7

Table 5.3 Roughness value of the samples made with just polymers and polymer complexes.
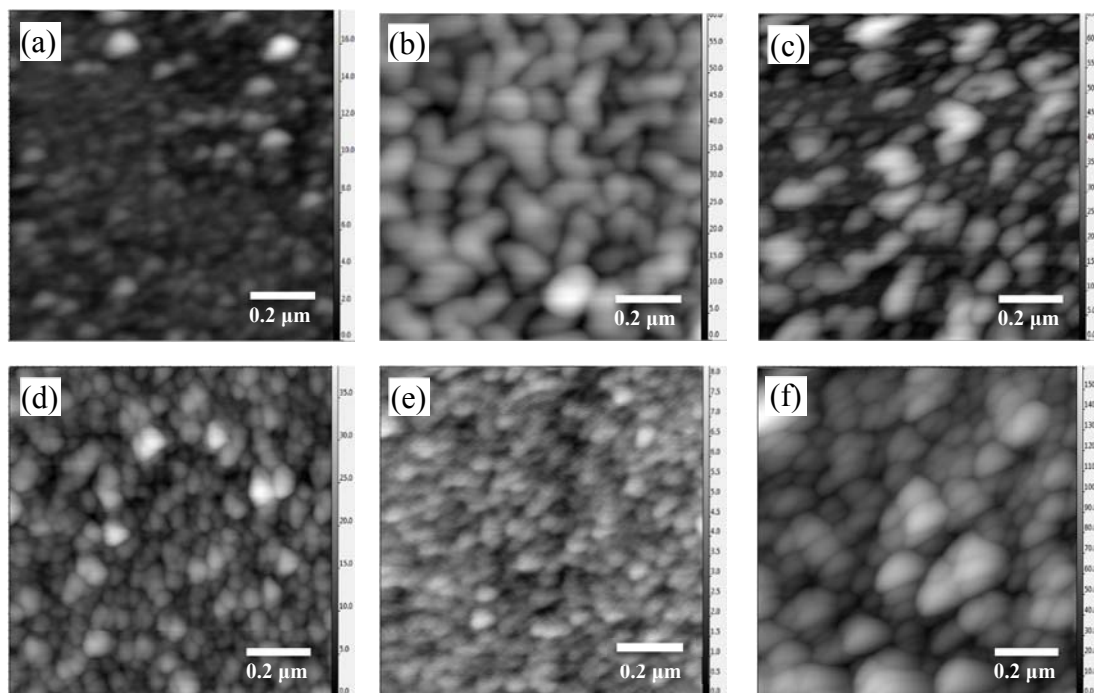
Figure 5.4 AFM scans of the (a) PEI/PSS-Polymer, (b) PDDA/PAA-Polymer, (c) PEI/PAA-Polymer, (d) PEI/PSS-20, (e) PDDA/PAA-20 and (f) PEI/PAA-20 samples made of 3 bilayers.

Gywddion software was used to apply watershed algorithm on AFM scans in order to locate the particles, and segment the images. The segmented image for one of the AFM scans is shown in Figure 5.5 Segmenting the AFM scan of PEI/PSS-10min sample using watershed algorithm.. The number of the particles as well as their mean area was obtained using this method. The AFM images of the PEI/PSS-10, PEI/PSS-20 and PEI/PSS-40 samples and their diagonal line profiles are shown in Figure 5.6. As mentioned previously, the last number in the sample designation corresponds to the duration of dipping during the fabrication of the samples. The roughness values of the samples and the number and mean area of globules in the 1 µm by 1 µm scan are shown in Table 5.4. By increasing the dipping time the number of globules slightly increased and the roughness value of the samples

decreased. The increase in dipping time, allowed more globules to form, and the denser

morphology of the layers decreased the roughness value.
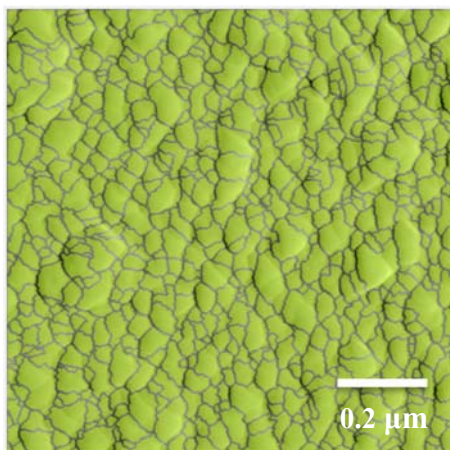
Figure 5.5 Segmenting the AFM scan of PEI/PSS-10min sample using watershed algorithm.

Sample label	R_a (nm) 5 μm × 5 μm	R_a (nm) 1 μm × 1 μm	Number of particles in 1 μm × 1 μm scan	Mean area of the particles (nm²)
PEI/PSS-10	7.5	6.13	720	1000
PEI/PSS-20	4.77	4.1	770	980
PEI/PSS-40	4.42	3.82	791	950
PDDA/PAA-10	1.03	1	640	1190
PDDA/PAA-20	0.85	0.873	678	1110
PDDA/PAA-40	0.91	0.99	709	1060

Table 5.4 Roughness values and number of the C-S-H particles of the PEI/PSS and PDDA/PAA samples with different dipping times made of 3 bilayers.

The AFM images of the PDDA/PAA-10, PDDA/PAA-20 and PDDA/PAA-40 samples

and their diagonal line profiles are shown in Figure 5.7. The roughness values of the

samples and the number and mean area of globules in the 1 μm by 1 μm scan are shown in

Table 5.4. A similar observation to PEI/PSS system can be made here. However, the height

of the particles in PDDA/PAA samples is an order of magnitude smaller than that of

PEI/PSS samples. This explains the smaller roughness value of the PDDA/PAA samples compared to that of PEI/PSS samples.

Figure 5.6 Morphology and diagonal cross section of the (a), (d) PEI/PSS-10, (b), (e) PEI/PSS-20 and (c), (f) PEI/PSS-40 samples made of 3 bilayers.
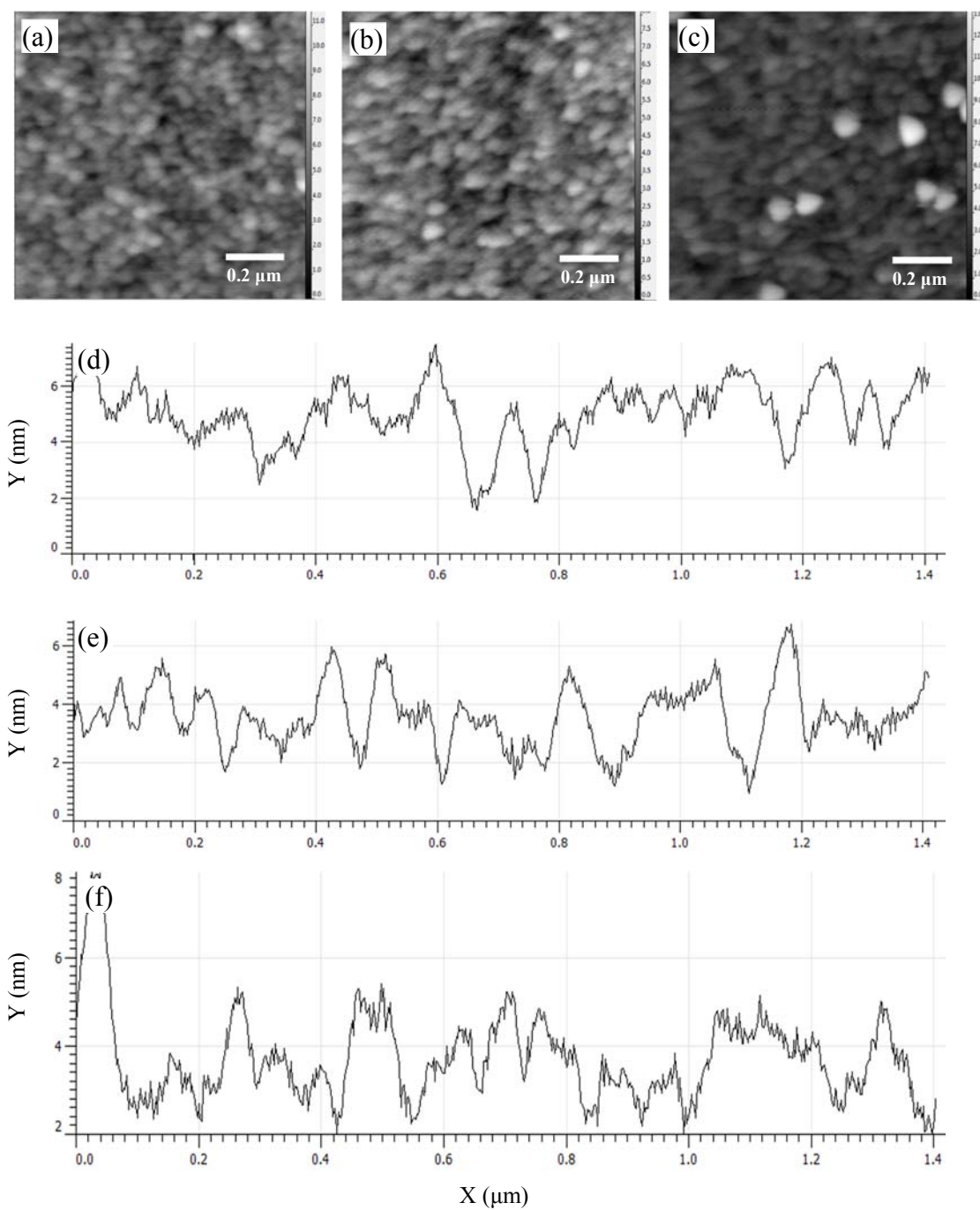
Figure 5.7 Morphology and diagonal cross section of the (a), (d) PDDA/PAA-10, (b), (e) PDDA/PAA and (c), (f) PDDA/PAA samples made of 3 bilayers.

PDDA/PAA-High pH sample was made same as the PDDA/PAA-20 sample. However,

in this sample the pH of the complex solutions was increased to 12.5 by addition of a 5 M

NaOH solution. PDDA has a high positive charge density which is reported to be unaffected by pH variation [124]. Its resistance to pH, makes PDDA a good candidate for preparing the C-S-H/Polymer nanocomposites at high pH. The AFM images of the PDDA/PAA-20 and PDDA/PAA-High pH samples and their diagonal line profiles are shown in Figure 5.8. The roughness values of the samples and the number and mean area of globules in the 1 μm by 1 μm scan are shown in Table 5.5. It is seen that the PDDA/PAA-High pH sample exhibits a noticeably higher roughness and larger globules compared to PDDA/PAA-20. The effect of pH increase on C-S-H precipitation from an aqueous solution was studied and shown to influence the structure and composition of C-S-H [181]. Prior work has also indicated the dependence of C-S-H nanoparticle aggregation on the pH of the solution [147][175]. The increase in pH influences the nucleation of C-S-H and also increases the negative charge density of C-S-H, which affects the interaction forces between the C-S-H nanoparticles and also between the C-S-H nanoparticles and polymer. These processes are expected to be responsible for increased roughness and almost two fold larger area of the globules in PDDA/PAA-High pH compared to PDDA/PAA-20. It should be noted that PAA is fully ionized above pH of 6.5 [180] and is not expected to undergo conformational changes when pH increases from about 10 to 12.5 as is the case in our study. In addition, as mentioned previously, PDDA is a strong polyelectrolyte and its charge density does not change with pH. Thus, it is unlikely that the conformational change of the polyelectrolyte contributes to the observed change in the roughness and globule area in the sample with increased pH.

Sample label	R_a (nm) 5 μm × 5 μm	R_a (nm) 1 μm × 1 μm	Number of particles in 1 μm × 1 μm scan	Mean area of the particles (nm²)
PDDA/PAA-20	0.85	0.873	678	1110
PDDA/PAA-High pH	1.46	1.39	394	2060

Table 5.5 Roughness values and number of the C-S-H the PDDA/PAA-20 and PDDA/PAA-HighpH samples made of 3 bilayers.
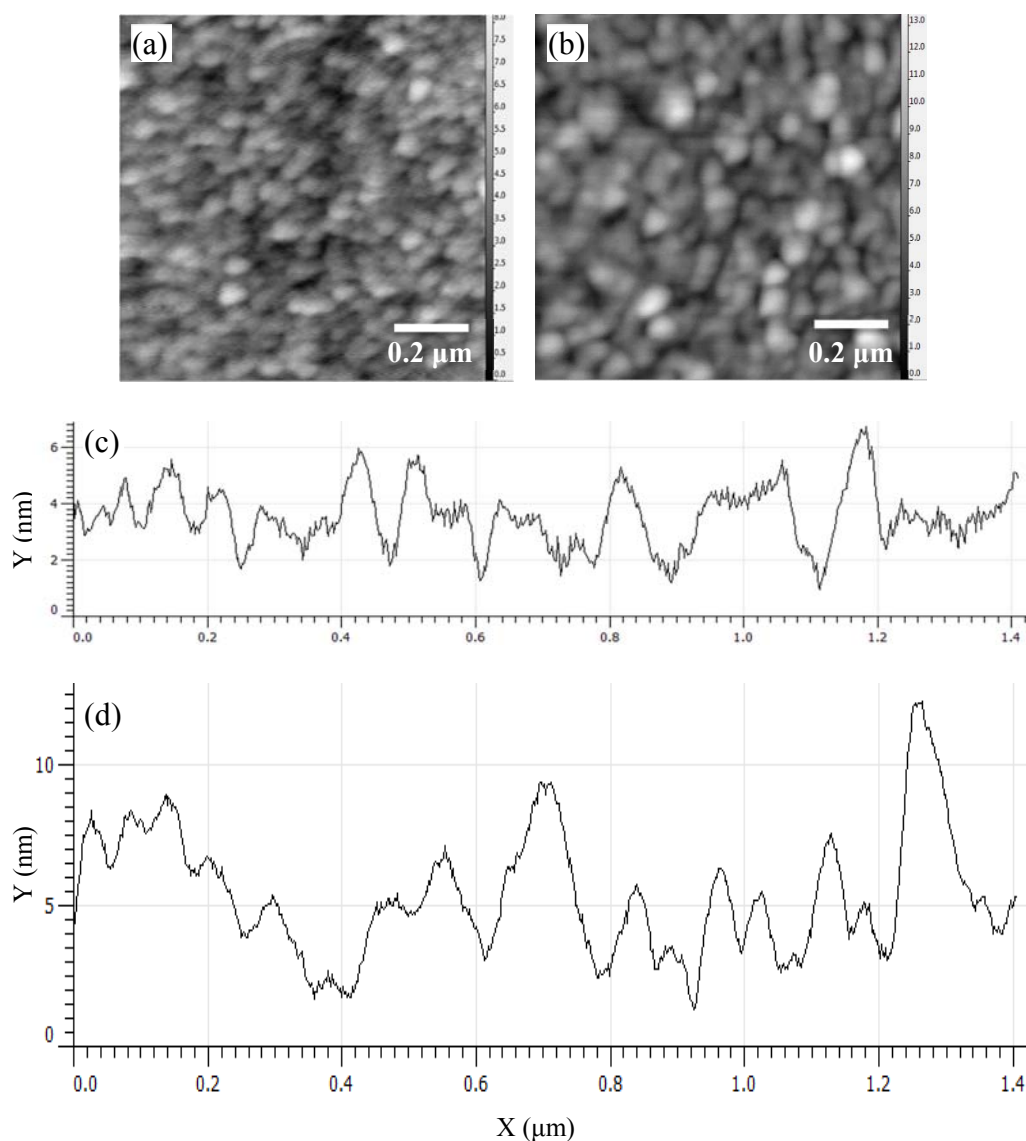
Figure 5.8 Morphology and diagonal section profile of the (a), (c) PDDA/PAA-20 and (b), (d) PDDA/PAA-High pH samples made of 3 bilayers.

PEI/PSS-Ca0.00514 and PEI/PSS-Ca0.1028 samples were made same as the PEI/PSS-20 sample. However, in these sample the concentrations of calcium acetate and sodium silicate were changed to one tenth and twice of that of the PEI/PSS-20 sample. The AFM images of the PEI/PSS-Ca0.00514, PEI/PSS-20 and PEI/PSS-Ca0.1028 samples and their diagonal line profiles are shown in Figure 5.9. The roughness values of the samples and the number and mean area of globules in the 1 μm by 1 μm scan are shown in Table 5.6. It can be observed that the morphology and the roughness value of the PEI/PSS-Ca0.00514 sample is comparable to those of the PEI/PSS-Polymer sample shown in Figure 5.4 and Table 5.3. This shows that the low concentration of the calcium salt did not form enough polymer complex to facilitate the nucleation of the C-S-H particles. On the other hand, larger and more agglomerated C-S-H particles were formed on the PEI/PSS-Ca0.1028 sample compared to the PEI/PSS-20 sample.

Sample label	R_a (nm) 5 μm × 5 μm	R_a (nm) 1 μm × 1 μm	Number of particles in 1 μm×1 μm scan	Mean area of the particles (nm^2)
PEI/PSS-Ca0.00514	1.14	1.01	980	760
PEI/PSS-20	4.77	4.1	770	980
PEI/PSS-Ca0.1028	4.4	4.05	576	1370

Table 5.6 Roughness values and number of the C-S-H particles the PEI/PSS samples with different calcium salt and sodium silicate concentrations made of 3 bilayers.
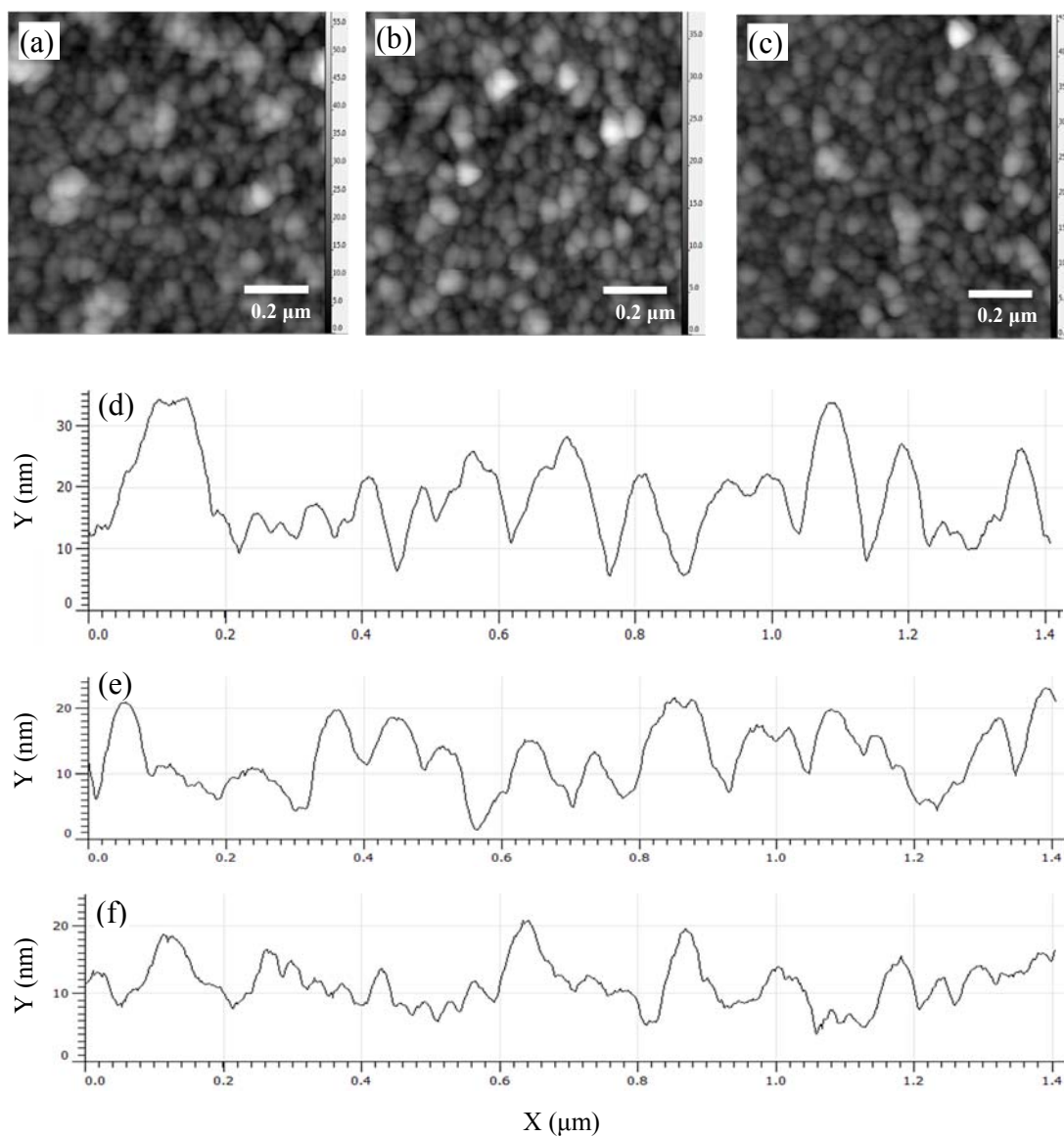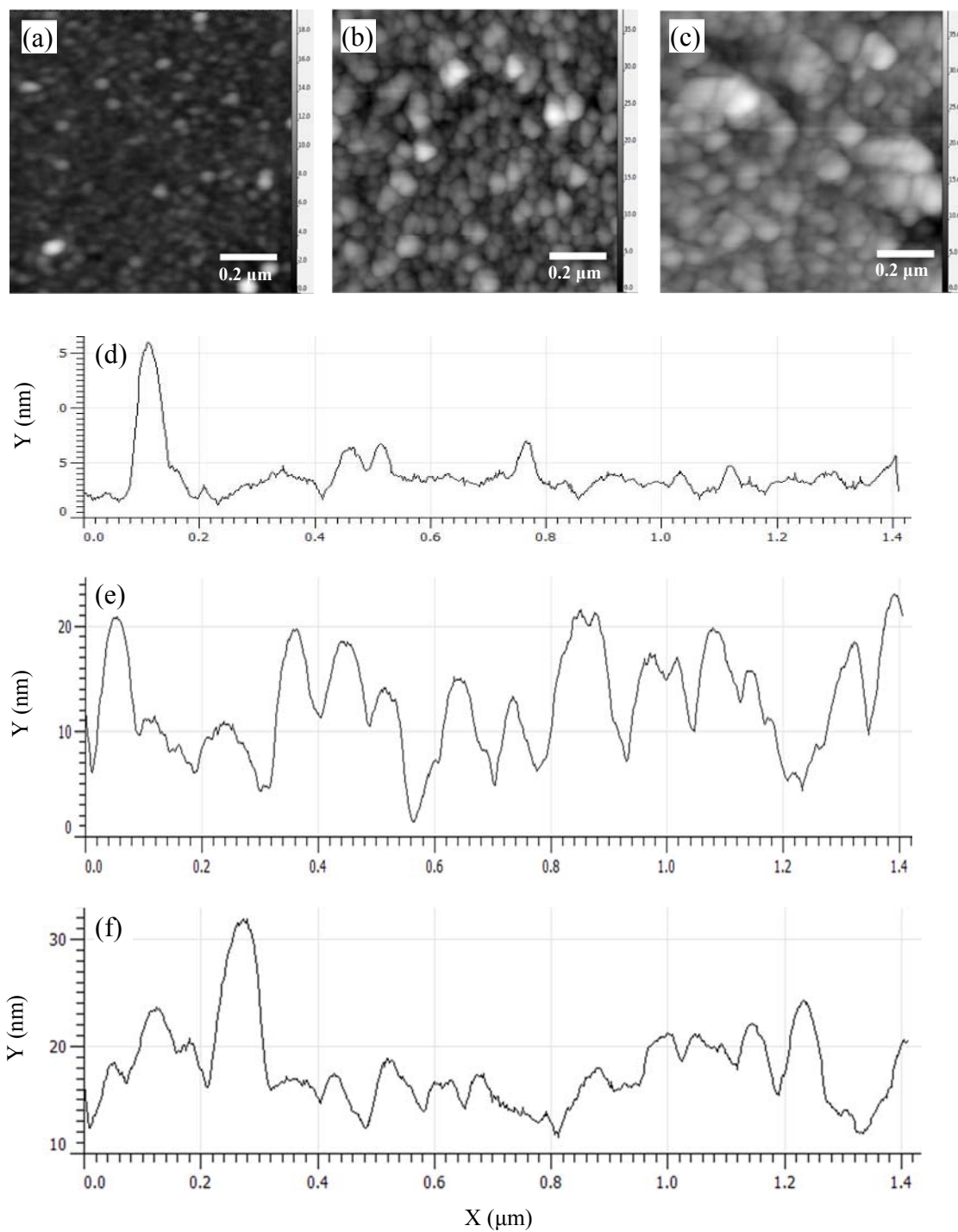
Figure 5.9 Morphology and diagonal section profile of the (a), (d) PEI/PSS-0.00514, (b), (e) PEI/PSS-20 and (c), (f) PEI/PSS-0.1028 samples made of 3 bilayers.

PEI/PSS-CS0.7, PEI/PSS-CS1.5 and PEI/PSS-CS2.3 samples were made same as PEI/PSS-20 sample. However, in these samples the concentration of sodium silicate was changed to provide calcium to silicate ratios of 0.7, 1.5 and 2.3, respectively. The AFM images of PEI/PSS-CS0.7, PEI/PSS-20, PEI/PSS-CS1.5 and PEI/PSS-CS2.3 samples and their diagonal line profiles are shown in Figure 5.10. The roughness values of the samples and the number and mean area of globules in the 1 μm by 1 μm scan are shown in Table 5.7. No significant difference in the size of the particles, roughness value and morphology of the samples can be observed. Statistical testing cannot be performed to confirm this statement because in roughness measurement just one data point for each sample was obtained. Also the raw data and standard deviation for the particle area measurement was not provided by the software. One possible explanation for not observing any difference is that the change in the concentration of the silicate ions in the PSS-SO$_3^{2-}$ solution does not lead to formation of more PSS-SO$_3^{2-}$ complex in the range of silicate concentrations used in the experiment. In this case, the formed C-S-H particles on the surface would have a similar chemical structure and calcium to silicate ratios regardless of the concentration of sodium silicate in the solution. The other possibility is that the samples have different calcium to silicate ratios but the morphology of the C-S-H particles is not dependent on the C/S ratio in the nanocomposite studied here. It should be mentioned that a morphology dependence on C/S ratio could exist in nanocomposites with other polymers and this needs further investigations. The effect of C/S ratio on the atomic structure and mechanical properties of synthetic pure C-S-H powder has been studied in the past and C/S ratio has been shown to influence these characteristics of C-S-H [182]. However, direct morphology studies of synthetic C-S-H with varied C/S ratios are currently scarce. Transmission

electron microscopy images of C-S-H powder with two different C/S ratios were presented

in [183]. However, no comparison in regard to the difference in morphology was made
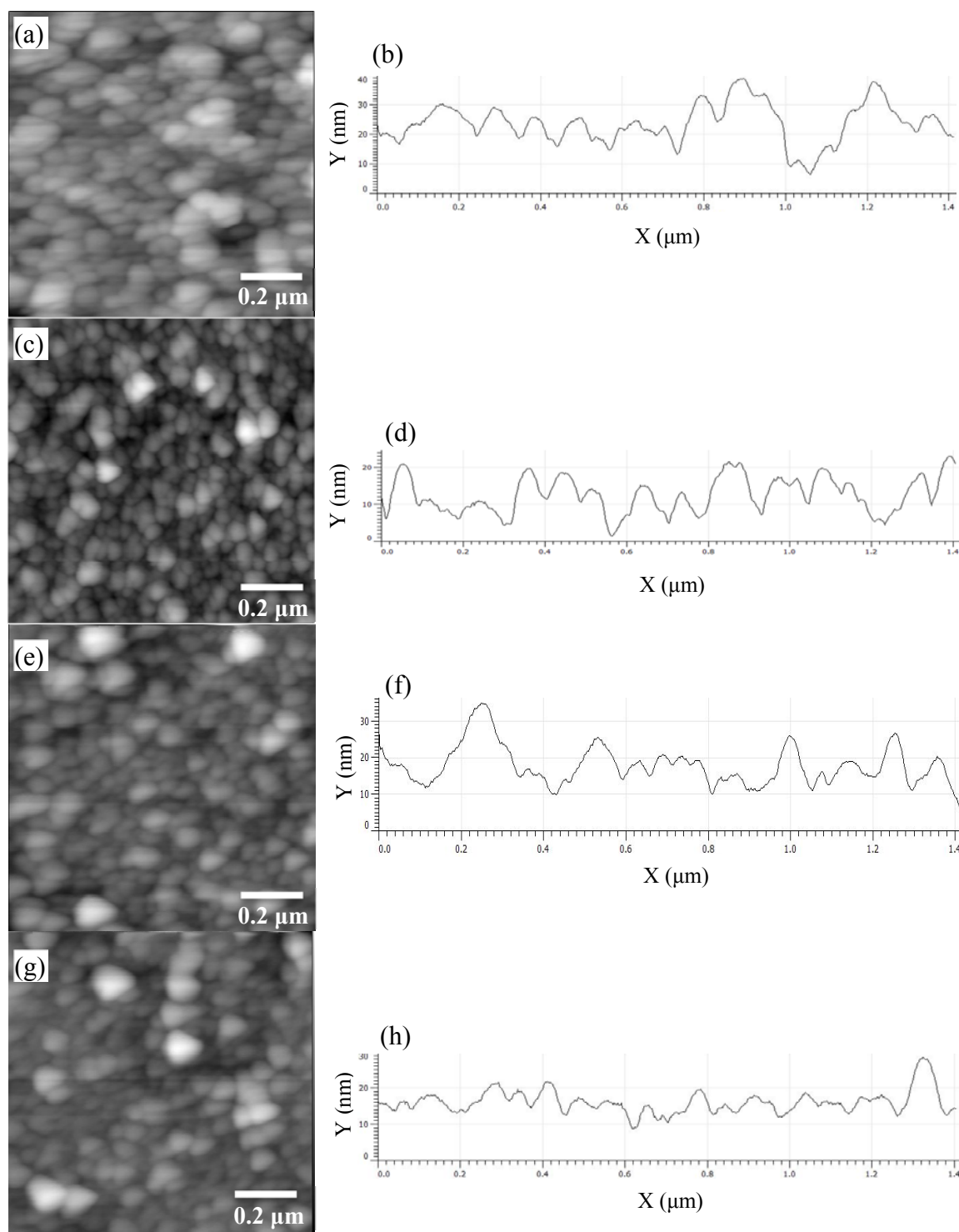
Figure 5.10 Morphology and diagonal cross section of the (a), (b) PEI/PSS-CS0.7, (c), (d) PEI/PSS-20 and (e), (f) PEI/PSS-CS1.5and (g), (h) PEI/PSS-CS2.3 samples made of 3 bilayers.

Sample label	R_a (nm) 5 μm × 5 μm	R_a (nm) 1 μm × 1 μm	Number of particles in 1 μm × 1 μm scan	Mean area of the particles (nm^2)
PEI/PSS-0.7	4.42	4.33	800	980
PEI/PSS-20	4.77	4.1	770	980
PEI/PSS-1.5	4.35	4.08	717	1060
PEI/PSS-2.3	4	4.03	711	1070

Table 5.7 Roughness values and number of the C-S-H particles of the PEI/PSS samples with different C/S values made of 3 bilayers.

5.3. AFM Nanoindentation

To perform nanoindentation, the PEI/PSS-20, PDDA/PAA-20 and PEI/PAA-20 samples were made with deposition of 25 bilayers to provide a sufficient thickness for indentation. To investigate the amount of C-S-H in the nanocomposites, a heat treatment at 350º C for 3 hours was performed on the samples. The polymer portion of the samples was burned out during the heat treatment and C-S-H particles were left on the substrate. The morphology of the PEI/PAA-20 sample before and after heat treatment is shown in Figure 5.11. The roughness value of the sample before and after heat treatment was 9 nm and 8.5 nm, respectively. No significant change was observed in the morphology of the samples before and after heat treatment. The thickness of the deposited layers was measured before and after heat treatment. A grove was made on the surface of the sample using the AFM probe to scratch the deposited layers. Then, the area around the grove was scanned by AFM and the thickness of the sample was measured. The AFM scan for the grove made on the PDDA/PAA-20 sample after the heat treatment is shown in Figure 5.12. The results of the nanoindentation and thickness measurement for the samples made with different polymer complex sets are shown in Table 5.8. The thickness has decreased to

about half of the initial value after performing the heat treatment for all the samples. However, the surface of the samples is mostly composed of C-S-H particles. The Young's modulus of the PEI/PSS-20 and PEI/PAA-20 samples increased modestly after heat treatment. The increase in the Young's modulus after removal of polymers can be explained from the mixing rule [184] as the phase fraction of hard C-S-H is increased. However, an increase of less than 8% was observed in the Young's modulus value of the PDDA/PAA-20 sample after performing the heat treatment. The value of Young's modulus of C-S-H/Polymer nanocomposite after removal of polymer is comparable to that of C-S-H/polymer nanocomposite powder reported in the literature [15,118,155]. It should be noted that it is possible for the polymers to be incorporated in the atomic structure of C-S-H stacks in the form of surface adsorption or intercalation in the interlayer space [11]. It is shown in the literatures that the removal of the polymer interacted with C-S-H happens at a temperature range of 250ºC to 550ºC [118]. Thus, the polymers incorporated in the atomic structure of C-S-H is not likely to be completely removed at the temperature used in the heat treatment. This is reflected from the lower values of Young's modulus of C-S-H after polymer removal compared to C-S-H powder without modification with polymer as reported in the literature [15,118].
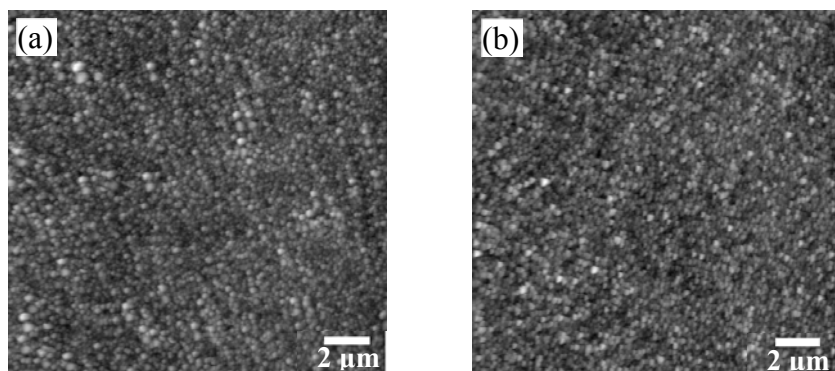
Figure 5.11 Morphology of the PEI/PAA-20 sample made of 25 bilayers (a) before and (b) after heat treatment.

Sample label	E (Gpa) before burning	Thickness (nm)	E (Gpa) after burning	Thickness (nm)
PEI/PSS-20	10.9	200	14.3	80
PDDA/PAA-20	11.9	180	11	80
PEI/PAA-20	10.4	190	15.3	100

Table 5.8 Average Young's modolus value and thickness of the samples made with different polymer complex sets and consisting of 25 bilayers.
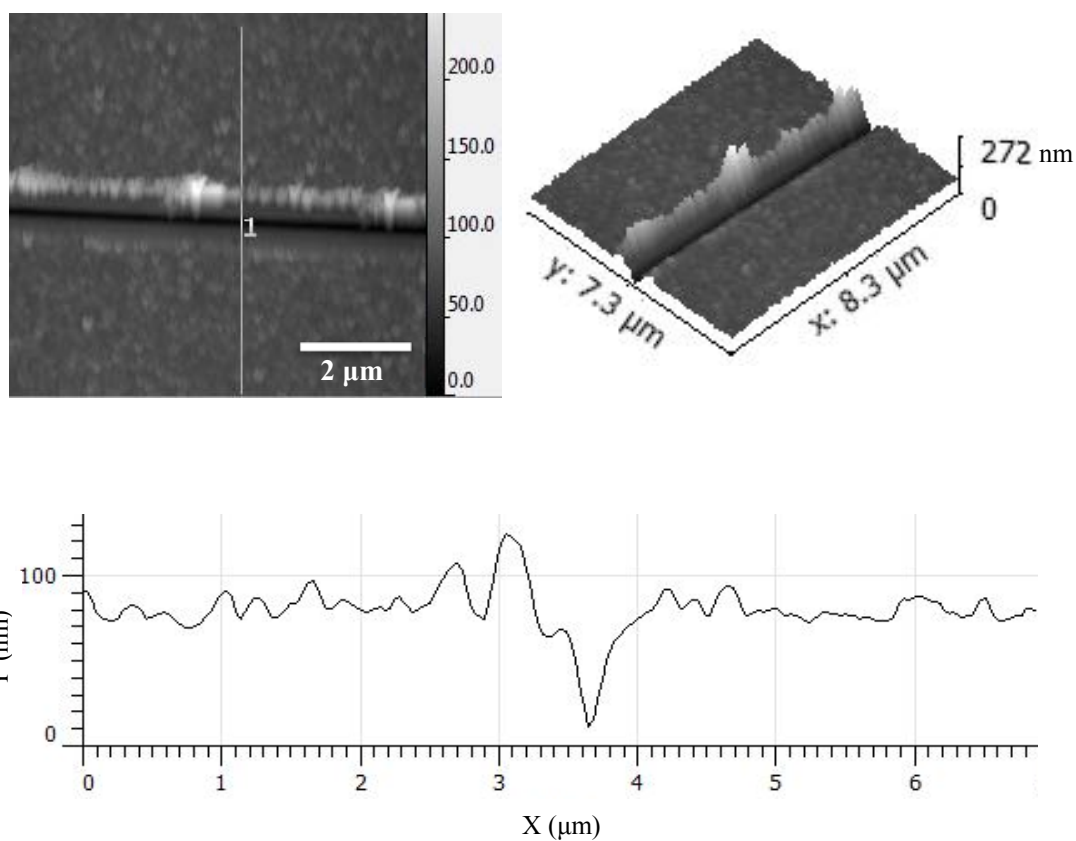
Figure 5.12 Thickness measurement of the PDDA/PAA-20 sample made of 25 bilayers after heat

5.4. GO/C-S-H/Polymer Nanocomposite

To elucidate the effects of GO on C-S-H/polymer systems, the PEI/PSS-GO sample containing 3 trilayers of PEI-Calcium acetate, GO and PSS-Sodium silicate was prepared. The surface of the sample was scanned by AFM. The AFM scans of a probed GO particle in the nanocomposite in shown in Figure 5.13. It can be observed that the concentration of the C-S-H globules on the surface of the GO nanosheet is higher than the other areas. This can be attributed to increased nucleation sites for the formation of C-S-H on the surface of GO. This observation can provide evidence for increased hydration in cementitious materials as a result of addition of GO. Care should be taken in the interpretation of this observation as the effect of polymers is not decoupled. An ideal situation would be to examine the nucleation of GO in LBL fabricated C-S-H/GO systems without the presence of polymers, which seems impractical as the polymers are needed for the LBL deposition method.

The morphology of the PEI/PSS-GO samples made of 25 trilayers of GO, PEI-Ca^{2+} and PSS-SiO_3^{2-} is shown in Figure 5.14. The surface of the sample appears to be rougher and irregular compared to that of the samples without GO. The surface roughness of the sample with GO is measured to be one order of magnitude higher than that of the sample without GO. The increase in roughness could be because the GO nanosheets are not deposited in a completely planar position and are folded or take a wavy form within the layers, as seen in Figure 5.14a. The C-S-H globules can be observed in the Figure 5.14b. It is observed that the GO nano sheets are folded in the composite and are not smoothly distributed as they did in the sample with 3 trilayers.

AFM nanoindentation was performed on the PEI-PSS/GO and the average value of the Young's modulus was calculated to be 5.7 GPa which is lower than the value corresponding to C-S-H/Polymer samples. A potential reason for this could be increased roughness of the sample with GO resulting in a reduction in the measured Young's modulus. The effect of surface roughness on measured Young's modulus using nanoindentation has been studied in the past [185]. It is also worth mentioning that although GO nanosheets seem to increase the nucleation of C-S-H particles, the adopted morphology of GO, such as folding and waviness, could result in a loosely packed structure of the nanocompsites contributing to a lower Young's modulus. More investigations are necessary to obtain more detailed insight in the CSH/Polymer/GO systems.
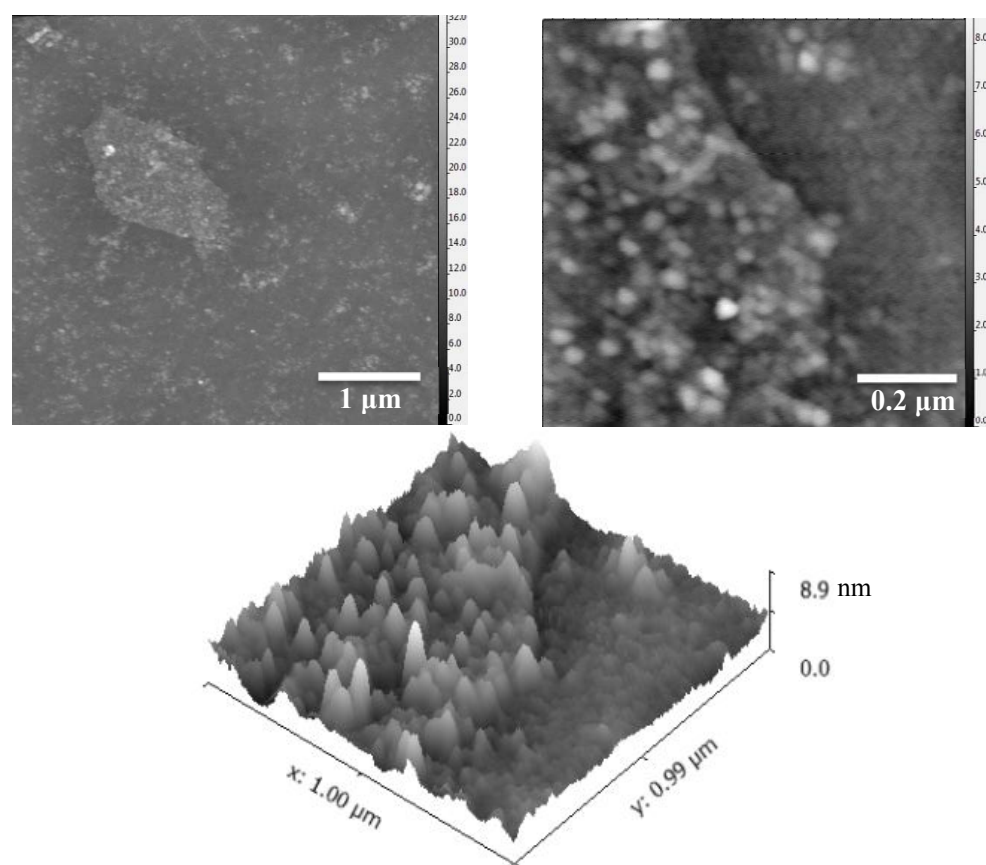
Figure 5.13 AFM scan of a GO nanosheet in the PEI/PSS-GO sample made of 3 trilayers.
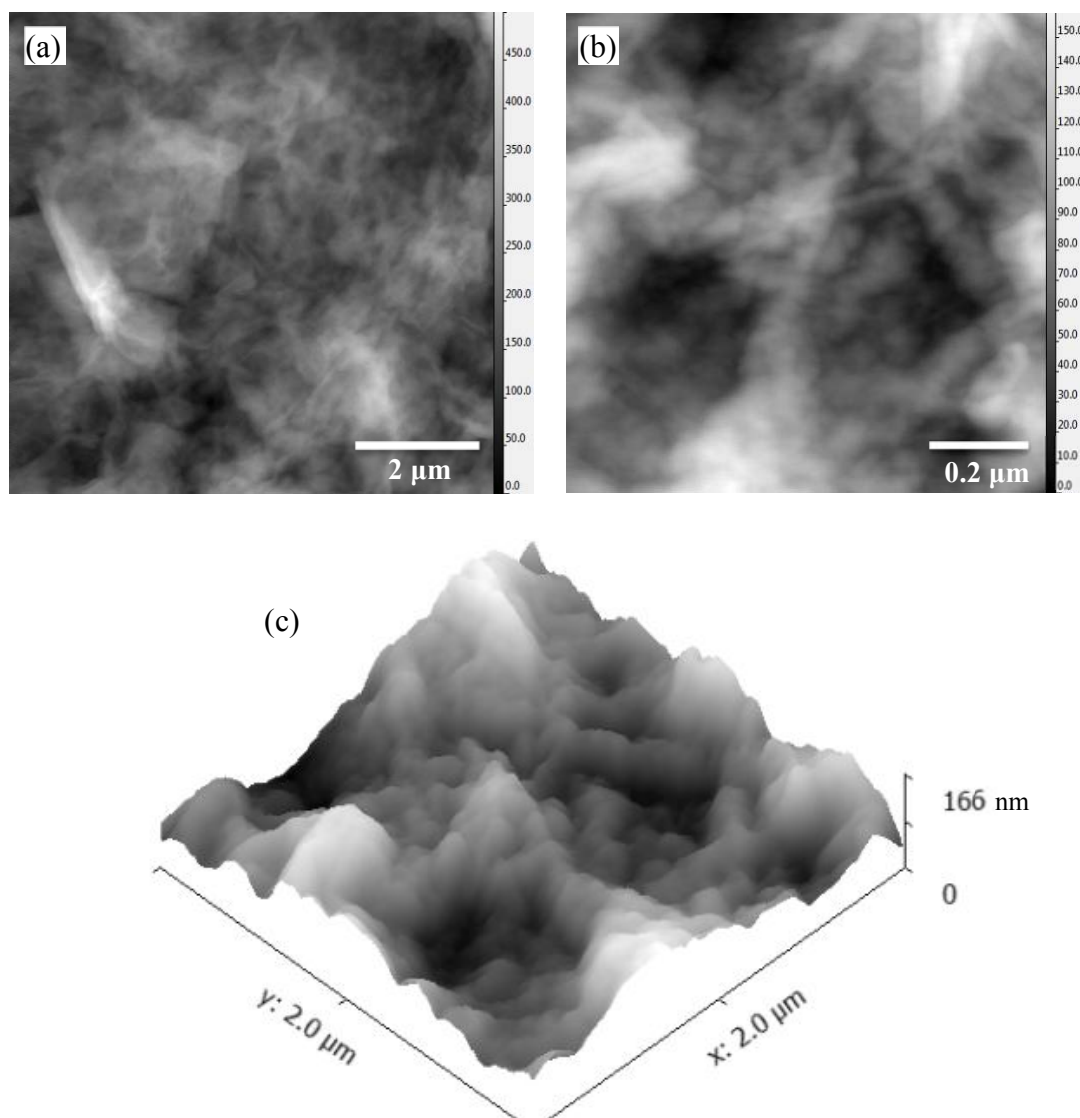
Figure 5.14 (a), (b) AFM scans and (c) topography of the PEI/PSS-GO sample made of 25 trilayers.

Chapter 6

6. Conclusions and Future Work

This project was designed to improve the current understanding about the interaction of polymers and biomolecules with C-S-H in order to discover the effect of polymers and biomolecules on the atomic structure and morphology of C-S-H, and to elucidate how polymers and biomolecules affect the Young's modulus of C-S-H. A comprehensive research study was planned in order to examine the key features of the C-S-H systems modified with polymers and biomolecules at the nano level. Several advanced analytical tools were used in order to corroborate the observations in each section. This study presented new evidence for the potential of biomolecules to manipulate the structure of bio-inspired materials. Biomolecules which are known to play a crucial role in the growth and microstructure formation of some biological nanocomposites that exhibit superior mechanical properties were studied in the structure of C-S-H and were shown to have the potential to manipulate the structure of C-S-H. The other fundamental achievements of the current work was to successfully incorporate C-S-H as the inorganic compound of biomimetic nanocomposites. For the first time a C-S-H/polymer nanocomposite with the aim of investigating the mechanical properties was fabricated using the bottom up LBL technique and its Young's modulus was measure using nanoindentation. The promising mechanical properties of the C-S-H modified systems such as more flexibility is highly desired in construction materials. The outcome of this study can be seen as a first step towards the formation of construction materials using bio-inspired approaches. The detailed observations in each chapter are described in this section.

In Chapter 3, the effect of cationic, anionic and polar polymers and amphiphilic copolymers on the nanostructure and nanomechanical properties of C-S-H was investigated. The findings of this section can be summarized as follows:

- At C/S of 0.8, the intercalation of the cationic PDDA between the negatively charged C-S-H layers was facilitated by electrostatic interactions. Hydrogen bonding to Ca-OH groups was the underlying mechanism of interaction between the polar PVA and C-S-H. At C/S of 1.5, no hint of interaction between PVA and PDDA, and C-S-H was observed.

- PAA has a retarding effect on the nucleation of C-S-H. This effect was confirmed by both XRD and FTIR results. The binding of Ca^{2+} ions present in the C-S-H solution due to the complex formation in presence of anionic PAA was responsible for the retardation in the C-S-H formation.

- The effect of amphiphilic PEG-PPG-PEG block copolymers on the structure of C-S-H was observed to be highly dependent on the molecular size of the copolymer.

- The interaction of the PEG-PPG-PEG copolymers with C-S-H was more pronounced at C/S ratio of 1.5, while PPG-PEG-PPG copolymers interacted with C-S-H at C/S of 0.7. The properties of the PEG-PPG-PEG copolymers are mainly governed by the polar PEG segment. However, in PEG-PPG-PEG copolymers the hydrophobic PPG segment is dominant.

In Chapter 4, the effect of biomolecules with distinct functional groups and various molecular sizes on the structure, morphology and Young's modulus of C-S-H was investigated. The finding of this chapter are as follows:

- The XRD analysis showed a change in the atomic structure, in the form of intercalation or surface adsorption, of C-S-H modified with the H-bond forming, hydrophobic and positively charged amino acids at both C/S=0.7 and 1.5. With increase in C/S ratio, the influence of negatively charged amino acid became more pronounced. Among the protein studied here, lysozyme appeared to show intercalation in C-S-H only at high C/S of 1.5. This could be related to the composition and conformation of this protein facilitating intercalation of this protein in C-S-H at this C/S ratio.

- The FTIR results indicated the effect of arginine on the silicate polymerization of C-S-H at low C/S ratio and increased influence of glutamic acid at higher C/S of 1.5. A noticeable increase in the silicate polymerization of samples modified with proteins at C/S of 1.5 was observed.

- The control C-S-H and the C-S-H modified with amino acids used in this study demonstrated a globular morphology of C-S-H nanoparticles. C-S-H modified with lysozyme and albumin also showed a globular morphology. The C-S-H samples modified with hemoglobin showed a platelet morphology in contrast to a globular morphology of the C-S-H modified with other proteins.

- A decrease in the Young's modulus of the C-S-H samples modified with amino acid was observed at lower C/S ratio. However, the effect of amino acid in altering the Young's modulus of C-S-H system was not significant at high C/S ratio.

- The Young's modulus of C-S-H with proteins was lower that of the control C-S-H at both C/S values. The reduction in the Young's modulus was slightly increased at

high C/S ratio. C-S-H modified with lysozyme was shown to exhibit a higher Young's modulus than C-S-H modified with albumin and hemoglobin.

In Chapter 5, C-S-H/polymer composites were synthesized with LBL method and their morphology and mechanical properties were investigated using AFM scanning and AFM nanoindentation. To further elucidate the possibility of improving the nucleation of C-S-H and mechanical properties of the composite, GO nano sheets were used in the LBL assembly. The findings of this chapter are as follows:

- Different sets of cationic and anionic polymers show different morphological shapes after LBL assembly. However, the C-S-H/Polymer composites made of different sets of polymers reveal the same globular shape attributed to C-S-H particles. The density and size of the globules were different in the samples.

- An increase in the pH level facilitate the nucleation of larger C-S-H particles.

- The surface of the C-S-H/Polymer composites is mainly consisted of the C-S-H particles which does not change in morphology after removing the polymers by heat treatment.

- The role of polymers in the elastic modulus of the C-S-H/Polymer composites obtained by AFM indentation method is negligible so that there is no significant difference in the value of their elastic modulus before and after heat treatment.

- The functionalized surface of the GO nano sheets helps with formation of C-S-H particles by providing a nucleation site for the particles.

- In the GO/C-S-H/Polymer composites made of 25 trilayers, the GO nano sheets are not placed in a well ordered structure and folded GOs can be probed in the sample.

Thus, the GO/C-S-H/Polymer composite showed a lower mechanical properties than the C-S-H/Polymer composite made of the same number of bilayers.

- The outcomes of this study show that C-S-H can be used as the inorganic part of organic/inorganic nanocomposites which is a promising approach in producing bio-inspired cementitious materials with superior mechanical properties.

The areas that deserve further investigations are suggested as follows:

- An investigation on the effect of polymer concentration as well as other C/S ratios will provide further information about the interaction between the polymeric compounds and C-S-H.

- Use of biological recombinant methods such as phage display permits identifying biomolecules with strong binding to C-S-H. Such studies have the potential to increase our understanding of the relation between biomolecule characteristics, such as composition and sequences, and C-S-H binding.

- Utilizing other analytical methods such as nuclear magnetic resonance (NMR), small angle X-ray scattering (SAXS) and transmission electron microscopy (TEM) will provide more valuable insights into the nanostructure of modified C-S-H.

- Future studies are needed to examine the time dependent mechanical response such as creep of C-S-H. This is particularly important as C-S-H is considered to play a direct role in the creep of cementitious materials [1,186].

References

[1]   M. Vandamme, F.J. Ulm, Nanogranular Origin of Concrete Creep., Proc. Natl. Acad. Sci. U. S. A. 106 (2009) 10552–10557.

[2]   B. Calder, Concrete and Culture: A Material History, J. Archit. 18 (2013) 744–756.

[3]   G.H. Brundtland, Our Common Future: Report of the World Commission on Environment and Development, 1987.

[4]   T.R. Naik, Sustainability of Concrete Construction, Pract. Period. Struct. Des. Constr. 13 (2008) 98–103.

[5]   A. Wiek, R.W. Foley, D.H. Guston, Nanotechnology for Sustainability: What Does Nanotechnology Offer to Address Complex Sustainability Problems?, in: Nanotechnol. Sustain. Dev. First Ed., 2014: pp. 371–390.

[6]   T. Rogers-Hayden, N. Pidgeon, Developments in Nanotechnology Public Engagement in the UK: "Upstream" towards Sustainability?, J. Clean. Prod. 16 (2008) 1010–1013.

[7]   A. Helland, H. Kastenholz, Development of Nanotechnology in Light of Sustainability, J. Clean. Prod. 16 (2008) 885–888.

[8]   M. Steinfeldt, U. Petschow, R. Haum, A. von Gleich, Nanotechnology and Sustainability, Schriftenr. Des IÖW. 167 (2004) 3.

[9]   S. Wong, B. Karn, Ensuring Sustainability with Green Nanotechnology, Nanotechnology. 23 (2012) 290201.

[10]   Mamadou Diallo and C. Jeffrey Brinker, Nanotechnology for Sustainability: Environment, Water, Food, Minerals, and Climate, Nanotechnol. Res. Dir. Soc. Needs 2020. 1 (2011) 221–259.

[11]   H. Matsuyama, J.F. Young, Intercalation of Polymers in Calcium Silicate Hydrate: A New Synthetic Approach to Biocomposites?, Chem. Mater. 11 (1999) 16–19.

[12]   F. Pelisser, P.J.P. Gleize, M. Peterson, Synthesis of Calcium Silicate Hydrate/Polymer Complexes: Part I. Anionic and Nonanionic Polymers, J. Mater. Res. 14 (1999) 3379–3388.

[13]   H. Matsuyama, J.F. Young, Synthesis of Calcium Silicate Hydrate/Polymer Complexes: Part II. Cationic Polymers and Complex Formation with Different Polymers, J. Mater. Res. 14 (1999) 3389–3396.

[14]   S.C. Mojumdar, L. Raki, Preparation and Properties of Calcium Silicate Hydrate-Poly(Vinyl Alcohol) Nanocomposite Materials, in: J. Therm. Anal. Calorim., 2005: pp. 89–95.

[15]   F. Pelisser, P.J.P. Gleize, A. Mikowski, Effect of Poly(Diallyldimethylammonium Chloride) on Nanostructure and Mechanical Properties of Calcium Silicate Hydrate, Mater. Sci. Eng. A. 527 (2010) 7045–7049.

[16]   R. Alizadeh, J.J. Beaudoin, L. Raki, V. Terskikh, C-S-H/Polyaniline Nanocomposites Prepared by In Situ Polymerization, J. Mater. Sci. 46 (2010) 460–467.

[17]   F. Merlin, H. Lombois, S. Joly, N. Lequeux, J.-L. Halary, H. Van Damme, Cement-Polymer and Clay-Polymer Nano- and Meso-Composites: Spotting the Difference, J. Mater. Chem. 12 (2002) 3308–3315.

[18]   R. Khoshnazar, J.J. Beaudoin, L. Raki, R. Alizadeh, Interaction of 2-, 3- and 4-Nitrobenzoic Acid with the Structure of Calcium-Silicate-Hydrate, Mater. Struct. Constr. (2014) 499–506.

[19]   F. Pelisser, P.J.P. Gleize, A. Mikowski, Structure and Micro-Nanomechanical Characterization of Synthetic Calcium-Silicate-Hydrate with Poly(Vinyl Alcohol), Cem. Concr. Compos. 48 (2014) 1–8.

[20]   T. Tong, Z. Fan, Q. Liu, S. Wang, S. Tan, Q. Yu, Investigation of the Effects of Graphene and Graphene Oxide Nanoplatelets on the Micro- and Macro-Properties of Cementitious Materials, Constr. Build. Mater. 106 (2016) 102–114.

[21]   L. Raki, J. Beaudoin, R. Alizadeh, J. Makar, T. Sato, Cement and Concrete Nanoscience and Nanotechnology, Materials (Basel). 3 (2010) 918–942.

[22]   R. Alizadeh, J.J. Beaudoin, L. Raki, Mechanical Properties of Calcium Silicate Hydrates, Mater. Struct. Constr. 44 (2011) 13–28.

[23]   R.J.M. Pellenq, N. Lequeux, H. van Damme, Engineering the Bonding Scheme in C-S-H: The Iono-Covalent Framework, Cem. Concr. Res. 38 (2008) 159–174.

[24]   C.A. Jones, Z.C. Grasley, J.A. Ohlhausen, Measurement of Elastic Properties of Calcium Silicate Hydrate with Atomic Force Microscopy, Cem. Concr. Compos. 34 (2012) 468–477.

[25]   A. Nonat, The Structure and Stoichiometry of C-S-H, Cem. Concr. Res. 34 (2004) 1521–1528.

[26]   F. Sanchez, K. Sobolev, Nanotechnology in Concrete - A Review, Constr. Build. Mater. 24 (2010) 2060–2071.

[27]   J. Chen, C.-S. Poon, Photocatalytic Activity of Titanium Dioxide Modified Concrete Materials - Influence of Utilizing Recycled Glass Cullets As Aggregates, J. Environ. Manage. 90 (2009) 3436–42.

[28]   J. Chen, S. Kou, C. Poon, Photocatalytic Cement-Based Materials: Comparison of Nitrogen Oxides and Toluene Removal Potentials and Evaluation of Self-Cleaning Performance, Build. Environ. 46 (2011) 1827–1833.

[29]   M. Aly, M.S.J. Hashmi, A.G. Olabi, M. Messeiry, A.I. Hussain, Effect of Nano Clay Particles on Mechanical, Thermal and Physical Behaviours of Waste-Glass Cement Mortars, Mater. Sci. Eng. A. 528 (2011) 7991–7998.

[30]   A. Popova, G. Geoffroy, M.F. Renou-Gonnord, P. Faucon, E. Gartner, Interactions between Polymeric Dispersants and Calcium Silicate Hydrates, J. Am. Ceram. Soc. 83 (2000) 2556–2560.

[31]   L. Ferrari, J. Kaufmann, F. Winnefeld, J. Plank, Multi-Method Approach for the Characterization of the Behavior of Superplasticizer in Cement Suspensions, in: 13th Int. Congr. Chem. Cem., 2011: pp. 1–7.

[32]   H.M. Jennings, J.J. Thomas, J.S. Gevrenov, G. Constantinides, F.J. Ulm, A Multi-Technique Investigation of the Nanoporosity of Cement Paste, Cem. Concr. Res. 37 (2007) 329–336.

[33]   J.J. Thomas, H.M. Jennings, A Colloidal Interpretation of Chemical Aging of the C-S-H Gel and Its Effects on the Properties of Cement Paste, Cem. Concr. Res. 36 (2006) 30–38.

[34]   H.F.W. Taylor, Nanostructure of CSH: Current Status, Adv. Cem. Based Mater. 1 (1993) 38–46.

[35]   C. Xiandong, R.J. Kirkpatrick, ^{29}Si MAS NMR Study of the Structure of Calcium Silicate Hydrate, Adv. Cem. Based Mater. 3 (1996) 144–156.

[36]   J. Sun, B. Bhushan, Hierarchical Structure and Mechanical Properties of Nacre: A Review, RSC Adv. 2 (2012) 7617.

[37]   P.J.M. Bartos, J.J. Hughes, P. Trtik, W. Zhu, Nanotechnology in Construction, 2009.

[38]   C. Giraudeau, J.B. D'Espinose De Lacaillerie, Z. Souguir, A. Nonat, R.J. Flatt, Surface and Intercalation Chemistry of Polycarboxylate Copolymers in Cementitious Systems, J. Am. Ceram. Soc. 92 (2009) 2471–2488.

[39]   J. Brandrup, E. Immergut, E.A. Grulke, Polymer Handbook, John Wiley Sons, Inc. 12 (1990) 265.

[40]   J.W. Nicholson, Chemistry of Polymers, R. Soc. Chem. (2006).

[41]   B.S. Förster, M. Antonietti, Amphiphilic Block Copolymers in Structure-Controlled Nanomaterial Hybrids, Adv. Mater. 10 (1998) 195–217.

[42]   A.G. Denkova, E. Mendes, M.O. Coppens, Effects of Salts and Ethanol on the Population and Morphology of Triblock Copolymer Micelles in Solution, J. Phys. Chem. B. 112 (2008) 793–801.

[43]   D. Zhao, Q. Huo, J. Feng, B.F. Chmelka, G.D. Stucky, Nonionic Triblock and Star Diblock Copolymer and Oligomeric Sufactant Syntheses of Highly Ordered, Hydrothermally Stable, Mesoporous Silica Structures, J. Am. Chem. Soc. 120 (1998) 6024–6036.

[44]   K. Flodström, V. Alfredsson, N. Källrot, Formation of a New Ia3⁻d Cubic Meso-Structured Silica via Triblock Copolymer-Assisted Synthesis, J. Am. Chem. Soc. 125 (2003) 4402–4403.

[45]   Y. Mai, A. Eisenberg, Self-Assembly of Block Copolymers, Chem. Soc. Rev. 41 (2012) 5969.

[46]   F.S. Bates, G.H. Fredrickson, Block Copolymers-Designer Soft Materials, Phys. Today. 52 (1999) 32–38.

[47]   L. Zhang, A. Eisenberg, Multiple Morphologies of "Crew-Cut" Aggregates of Polystyrene-b-poly(acrylic acid) Block Copolymers, Science (80-.). 268 (1995) 1728–1731.

[48]   J. Rodríguez-Hernández, F. Chécot, Y. Gnanou, S. Lecommandoux, Toward "Smart" Nano-Objects by Self-Assembly of Block Copolymers in Solution, Prog. Polym. Sci. 30 (2005) 691–724.

[49]   B.K. Lau, Q. Wang, W. Sun, L. Li, Micellization to Gelation of a Triblock Copolymer in Water: Thermoreversibility and Scaling, J. Polym. Sci. Part B Polym. Phys. 42 (2004) 2014–2025.

[50]   H. Ma, Y. Tian, Z. Li, Interactions between Organic and Inorganic Phases in PA- and PU/PA-Modified-Cement-Based Materials, ASCE J. Mater. Civ. Eng. 23 (2011) 1412–1421.

[51]   I. Pochard, C. Labbez, A. Nonat, H. Vija, B. Jönsson, The Effect of Polycations on Early Cement Paste, Cem. Concr. Res. 40 (2010) 1488–1494.

[52]   P. Das, A. Walther, Ionic Supramolecular Bonds Preserve Mechanical Properties and Enable Synergetic Performance at High Humidity in Water-Borne, Self-Assembled Nacre-Mimetics, Nanoscale. 5 (2013) 9348.

[53]   A. Arakaki, K. Shimizu, M. Oda, T. Sakamoto, T. Nishimura, T. Kato, Biomineralization-Inspired Synthesis of Functional Organic/Inorganic Hybrid Materials: Organic Molecular Control of Self-Organization of Hybrids, Org. Biomol. Chem. 13 (2015) 974–989.

[54]   Y. Razvag, V. Gutkin, M. Reches, Probing the Interaction of Individual Amino Acids with Inorganic Surfaces Using Atomic Force Spectroscopy, (2013) 1–14.

[55]   T. Verho, M. Karesoja, P. Das, L. Martikainen, R. Lund, A. Alegría, A. Walther, O. Ikkala, Hydration and Dynamic State of Nanoconfined Polymer Layers Govern Toughness in Nacre-Mimetic Nanocomposites, Adv. Mater. 25 (2013) 5055–5059.

[56]   K.M.S. Juhl, N. Bovet, T. Hassenkam, K. Dideriksen, C.S. Pedersen, C.M. Jensen, D. V. Okhrimenko, S.L.S. Stipp, Change in Organic Molecule Adhesion on α-alumina (Sapphire) with Change in NaCl and $CaCl_2$ Solution Salinity, Langmuir. 30 (2014) 8741–8750.

[57]   Z. Wang, T.J. Pinnavaia, Nanolayer Reinforcement of Elastomeric Polyurethane, Chem. Mater. 10 (1998) 3769–3771.

[58]   Z. Wang, T.J. Pinnavaia, Hybrid Organic−Inorganic Nanocomposites: Exfoliation of Magadiite Nanolayers in an Elastomeric Epoxy Polymer, Chem. Mater. 10 (1998) 1820–1826.

[59]   J.C. Rodríguez Hernández, M. Salmerón Sánchez, J.L. Gómez Ribelles, M. Monleón Pradas, Polymer-Silica Nanocomposites Prepared by Sol-Gel Technique: Nanoindentation and Tapping Mode AFM Studies, Eur. Polym. J. 43 (2007) 2775–2783.

[60]   J. Minet, S. Abramson, B. Bresson, A. Franceschini, H. Van Damme, N. Lequeux, Organic Calcium Silicate Hydrate Hybrids: A New Approach to Cement Based Nanocomposites, J. Mater. Chem. 16 (2006) 1379.

[61]   J. Minet, S. Abramson, B. Bresson, C. Sanchez, V. Montouillout, N. Lequeux, New Layered Calcium Organosilicate Hybrids with Covalently Linked Organic Functionalities, Chem. Mater. 16 (2004) 3955–3962.

[62]   L. Addadi, D. Joester, F. Nudelman, S. Weiner, Mollusk Shell Formation: A Source of New Concepts for Understanding Biomineralization Processes, Chemistry. 12 (2006) 980–987.

[63]   S. Simmonds, Biochemistry of the Amino Acids, Yale J. Biol. Med. 38 (1966) 383–384.

[64]   A. Ellington, J.M. Cherry, Characteristics of Amino Acids, Curr. Protoc. Mol. Biol. Appendix 1 (2001).

[65]   L.G.J. Wade, Amino Acids, Peptides, and Proteins, Org. Chem. 2 (2009) 1320.

[66]   A. Picker, L. Nicoleau, A. Nonat, C. Labbez, H. Cölfen, Identification of Binding Peptides on Calcium Silicate Hydrate: A Novel View on Cement Additives, Adv. Mater. 26 (2014) 1135–1140.

[67]   G.P. Smith, V. a Petrenko, Phage Display, Chem. Rev. 97 (1997) 391–410.

[68]   B. Birgisson, A.K. Mukhopadhyay, G. Geary, M. Khan, K. Sobolev, Nanotechnology in Concrete Materials, 2012.

[69]   J. Björnström, A. Martinelli, A. Matic, L. Börjesson, I. Panas, Accelerating Effects of Colloidal Nano-Silica for Beneficial Calcium-Silicate-Hydrate Formation in Cement, Chem. Phys. Lett. 392 (2004) 242–248.

[70]   K.L. Lin, W.C. Chang, D.F. Lin, H.L. Luo, M.C. Tsai, Effects of nano-SiO2 and different ash particle sizes on sludge ash-cement mortar, J. Environ. Manage. 88 (2008) 708–714.

[71]   B.M. Tyson, R.K. Abu Al-Rub, A. Yazdanbakhsh, Z. Grasley, Carbon Nanotubes and Carbon Nanofibers for Enhancing the Mechanical Properties of Nanocomposite Cementitious Materials., J. Mater. Civ. Eng. 23 (2011) 1028–1035.

[72]   Hosseini P., Booshehrian A., F. S., Influence of Nano-SiO$_2$ Addition on Microstructure and Mechanical Properties of Cement Mortars for Ferrocement, Transp. Res. Rec. (2010) 15–20.

[73]   I. Flores, K. Sobolev, L.M. Torres-Martinez, E.L. Cuellar, P.L. Valdez, E. Zarazua, Performance of Cement Systems with Nano-SiO$_2$ Particles Produced by Using the Sol-Gel Method, J. Transp. Res. Board. (2010) 10–14.

[74]   B.W. Jo, C.H. Kim, G. h. Tae, J.B. Park, Characteristics of Cement Mortar with Nano-SiO2 Particles, Constr. Build. Mater. 21 (2007) 1351–1355.

[75]   L. Senff, J.A. Labrincha, V.M. Ferreira, D. Hotza, W.L. Repette, Effect of Nano-Silica on Rheology and Fresh Properties of Cement Pastes and Mortars, Constr. Build. Mater. 23 (2009) 2487–2491.

[76]   K. Gao, K.L. Lin, D. Wang, C.L. Hwang, B. Le Anh Tuan, H.S. Shiu, T.W. Cheng, Effect of Nano-SiO2 on the Alkali-Activated Characteristics of Metakaolin-Based Geopolymers, Constr. Build. Mater. 48 (2013) 441–447.

[77]   P.K. Hou, S. Kawashima, K.J. Wang, D.J. Corr, J.S. Qian, S.P. Shah, Effects of Colloidal Nanosilica on Rheological and Mechanical Properties of Fly Ash-Cement Mortar, Cem. Concr. Compos. 35 (2013) 12–22.

[78]   G.Y. Li, P.M. Wang, X. Zhao, Mechanical Behavior and Microstructure of Cement Composites Incorporating Surface-Treated Multi-Walled Carbon Nanotubes, Carbon N. Y. 43 (2005) 1239–1245.

[79]   M.S. Konsta-Gdoutos, Z.S. Metaxa, S.P. Shah, Multi-Scale Mechanical and Fracture Characteristics and Early-Age Strain Capacity of High Performance Carbon Nanotube/Cement Nanocomposites, Cem. Concr. Compos. 32 (2010) 110–115.

[80]   Y. Sáez de Ibarra, J.J. Gaitero, E. Erkizia, I. Campillo, Atomic Force Microscopy and Nanoindentation of Cement Pastes with Nanotube Dispersions, Phys. Status Solidi. 203 (2006) 1076–1081.

[81]   M. Lackhoff, X. Prieto, N. Nestle, F. Dehn, R. Niessner, Photocatalytic Activity of Semiconductor-Modified Cement - Influence of Semiconductor Type and Cement Ageing, Appl. Catal. B Environ. 43 (2003) 205–216.

[82]   A.R. Jayapalan, B.Y. Lee, S.M. Fredrich, K.E. Kurtis, Influence of Additions of Anatase TiO$_2$ Nanoparticles on Early-Age Properties of Cement-Based Materials, Transp. Res. Rec. J. Transp. Res. Board. 2141 (2010) 41–46.

[83]   B.Y. Lee, K.E. Kurtis, Influence of TiO$_2$ Nanoparticles on Early C$_3$S Hydration, J. Am. Ceram. Soc. 93 (2010) 3399–3405.

[84]   J. Chen, S.C. Kou, C.S. Poon, Hydration and Properties of Nano-TiO$_2$ Blended Cement Composites, Cem. Concr. Compos. 34 (2012) 642–649.

[85]   B.Y. Lee, K.E. Kurtis, Effects of Nano-TiO2 on Properties of Cement-Based Materials, 65 (2013).

[86]   R. Zhang, X. Cheng, P. Hou, Z. Ye, Influences of Nano-TiO$_2$ on the Properties of Cement-Based Materials: Hydration and Drying Shrinkage, Constr. Build. Mater. 81 (2015) 35–41.

[87]   B. Ma, H. Li, J. Mei, X. Li, F. Chen, Effects of Nano-TiO$_2$ on the Toughness and Durability of Cement-Based Material, 2015 (2015).

[88]   K.E. Strawhecker, E. Manias, Structure and Properties of Poly(Vinyl Alcohol)/Na$^+$ Montmorillonite Nanocomposites, (2000) 2943–2949.

[89]   P. Podsiadlo, A.K. Kaushik, E.M. Arruda, A.M. Waas, B.S. Shim, J. Xu, H. Nandivada, B.G. Pumplin, J. Lahann, A. Ramamoorthy, N.A. Kotov, Ultrastrong and Stiff Layered Polymer Nanocomposites, Science. 318 (2007) 1–4.

[90]   R. Prasanth, N. Shubha, H.H. Hng, M. Srinivasan, Effect of Nano-Clay on Ionic Conductivity and Electrochemical Properties of Poly(Vinylidene Fluoride) Based Nanocomposite Porous Polymer Membranes and Their Application as Polymer Electrolyte in Lithium Ion Batteries, Eur. Polym. J. 49 (2013) 307–318.

[91]   A. Hakamy, F.U.A. Shaikh, I.M. Low, Effect of Calcined Nanoclay on the Durability of NaOH Treated Hemp Fabric-Reinforced Cement Nanocomposites, Mater. Des. 92 (2016) 659–666.

[92]   S. Lv, Y. Ma, C. Qiu, T. Sun, J. Liu, Q. Zhou, Effect of Graphene Oxide Nanosheets of Microstructure and Mechanical Properties of Cement Composites., 49 (2013) 121–127.

[93]   H. Alkhateb, A. Al-Ostaz, A.H.-D. Cheng, X. Li, Materials Genome for Graphene-Cement Nanocomposites, J. Nanomechanics Micromechanics. 3 (2013) 67–77.

[94]   A. Sedaghat, M.K. Ram, A. Zayed, R. Kamal, N. Shanahan, Investigation of Physical Properties of Graphene-Cement Composite for Structural Applications, Open J. Compos. Mater. 4 (2014) 12–21.

[95]   Y. Li, F. Liu, J. Sun, A Facile Layer-by-Layer Deposition Process for the Fabrication of Highly Transparent Superhydrophobic Coatings., Chem. Commun. (Camb). (2009) 2730–2732.

[96]   J. Xu, Z. Wang, L. Wen, X. Zhou, J. Xu, S. Yang, Dynamics of the Layer-by-Layer Assembly of a Poly(Acrylic Acid)-Lanthanide Complex Colloid and Poly(DiallylDimethyl Ammonium), Soft Matter. 12 (2016) 867–875.

[97]   L. Zhang, Y. Li, J. Sun, J. Shen, Mechanically Stable Antireflection and Antifogging Coatings Fabricated by the Layer-by-Layer Deposition Process and Postcalcination, Langmuir. 24 (2008) 10851–10857.

[98]   H. Guo, Y. Ma, P. Sun, S. Cui, Z. Qin, Y. Liang, Self-Cleaning and Antifouling Nanofiltration Membranes-Superhydrophilic Multilayered Polyelectrolyte/CSH Composite Films Towards Rejection of Dyes, RSC Adv. 5 (2015) 63429–63438.

[99]   H. Guo, P. Sun, Y. Liang, Y. Ma, Z. Qin, S. Cui, In-Situ Fabrication of Polyelectrolyte-CSH Superhydrophilic Coatings via Layer-by-Layer Assembly, Chem. Eng. J. 253 (2014) 198–206.

[100] Z. Tang, Y. Wang, P. Podsiadlo, N.A. Kotov, Biomedical Applications of Layer-by-Layer Assembly: From Biomimetics to Tissue Engineering, Adv. Mater. 18 (2006) 3203–3224.

[101] K. Ariga, J.P. Hill, Q. Ji, Layer-by-Layer Assembly as a Versatile Bottom-Up Nanofabrication Technique for Exploratory Research and Realistic Application, Phys. Chem. Chem. Phys. 9 (2007) 2319–2340.

[102] F.-X. Xiao, M. Pagliaro, Y.-J. Xu, B. Liu, Layer-by-Layer Assembly of Versatile Nanoarchitectures with Diverse Dimensionality: A New Perspective for Rational Construction of Multilayer Assemblies., Chem. Soc. Rev. 45 (2016).

[103]   a. C. Fou, O. Onitsuka, M. Ferreira, M.F. Rubner, B.R. Hsieh, Fabrication and Properties of Light-Emitting Diodes Based on Self-Assembled Multilayers of Poly(Phenylene Vinylene), J. Appl. Phys. 79 (1996) 7501.

[104] J.H. Cheung, W.B. Stockton, M.F. Rubner, Molecular-Level Processing of Conjugated Polymers. 3. Layer-by-Layer Manipulation of Polyaniline via Electrostatic Interactions, Macromolecules. 30 (1997) 2712–2716.

[105] Y. Lvov, S. Yamada, T. Kunitake, Non-Linear Optical Effects in Layer-by-Layer Alternate Films of Polycations and an Azobenzene-Containing Polyanion, Thin Solid Films. 300 (1997) 107–112.

[106] S. Liu, R. Montazami, Y. Liu, V. Jain, M. Lin, J.R. Heflin, Q.M. Zhang, Layer-by-Layer Self-Assembled Conductor Network Composites in Ionic Polymer Metal Composite Actuators with High Strain Response, Appl. Phys. Lett. 95 (2009).

[107] A.J. Khopade, F. Caruso, Surface-Modification of Polyelectrolyte Multilayer-Coated Particles for Biological Applications, Langmuir. 19 (2003) 6219–6225.

[108]   W. Tong, X. Song, C. Gao, Layer-by-Layer Assembly of Microcapsules and Their Biomedical Applications, Chem. Soc. Rev. 41 (2012) 6103–6124.

[109]   B.S. Kim, J.W. Choi, Polyelectrolyte Multilayer Microcapsules: Self-Assembly and Toward Biomedical Applications, Biotechnol. Bioprocess Eng. 12 (2007) 323–332.

[110]   A. Shukla, B. Almeida, Advances in Cellular and Tissue Engineering Using Layer-by-Layer Assembly, Wiley Interdiscip. Rev. Nanomedicine Nanobiotechnology. 6 (2014) 411–421.

[111]   V. Guduric, C. Metz, R. Siadous, R. Bareille, R. Levato, E. Engel, J.C. Fricain, R. Devillard, O. Luzanin, S. Catros, Layer-by-Layer Bioassembly of Cellularized Polylactic Acid Porous Membranes for Bone Tissue Engineering, J. Mater. Sci. Mater. Med. 28 (2017).

[112]   T. Lee, S.H. Min, M. Gu, Y.K. Jung, W. Lee, J.U. Lee, D.G. Seong, B. Kim, Layer-by-Layer Assembly for Graphene-Based Multilayer Nanocomposites: Synthesis and Applications, Chem. Mater. 27 (2015) 3785–3796.

[113]   F. Babak, H. Abolfazl, R. Alimorad, G. Parviz, Preparation and Mechanical Properties of Graphene Oxide: Cement Nanocomposites, Sci. World J. 2014 (2014).

[114]   D.M. Jarvie, Total Organic Carbon (TOC) Analysis, in: Source Migr. Process. Eval. Tech., 1991: pp. 113–118.

[115]   S. Grangeon, F. Claret, Y. Linard, C. Chiaberge, X-ray Diffraction: A powerful Tool to Probe and Understand the Structure of Nanocrystalline Calcium Silicate Hydrates, Acta Crystallogr. Sect. B Struct. Sci. Cryst. Eng. Mater. 69 (2013) 465–473.

[116]   J. Němeček, Creep Effects in Nanoindentation of Hydrated Phases of Cement Pastes, Mater. Charact. 60 (2009) 1028–1034.

[117]   C. Berthomieu, R. Hienerwadel, Fourier Transform Infrared (FTIR) Spectroscopy, Photosynth. Res. 101 (2009) 157–170.

[118]   F. Pelisser, P.J.P. Gleize, A. Mikowski, Structure and Micro-Nanomechanical Characterization of Synthetic Calcium–Silicate–Hydrate with Poly(Vinyl Alcohol), Cem. Concr. Compos. 48 (2014) 1–8.

[119]   P. Yu, R.J. Kirkpatrick, B. Poe, P.F. McMillan, X. Cong, Structure of Calcium Silicate Hydrate (C-S-H): Near-, Mid-, and Far-Infrared Spectroscopy, J. Am. Ceram. Soc. 82 (1999) 742–748.

[120]   Zeta Potential Theory, in: Zetasizer Nano User Man., 2013.

[121] R.S. Gates, M.G. Reitsma, J. a. Kramar, J.R. Pratt, Atomic Force Microscope Cantilever Flexural Stiffness Calibration: Toward a Standard Traceable Method, J. Res. Natl. Inst. Stand. Technol. 116 (2011) 703.

[122] M. a. Monclus, T.J. Young, D. Di Maio, AFM Indentation Method Used for Elastic Modulus Characterization of Interfaces and Thin Layers, J. Mater. Sci. 45 (2010) 3190–3197.

[123] H. Hertz, On the Contact of Elastic Solids, J Reine Angew Math. 92 (1881) 156–171.

[124] Wilson John, Synthesis, Properties and Analysis of PolyDADMAC for Water Purification, 2008.

[125] A. Massoud, S.A. Waly, Preparation and Characterization of Poly (Acrylic Acid-Dimethylaminoethylmethacrylate) as Amphoteric Exchange Resin and Its Adsorption Properties, Colloid Polym. Sci. 292 (2014) 3077–3083.

[126] X.X. Chen, G.G. Shan, J. Huang, Z.Z. Huang, Z.Z. Weng, Synthesis and Properties of Acrylic-Based Superabsorbent, J. Appl. Polym. Sci. 92 (2004) 619–624.

[127] S. Kobayashi, K. Müllen, Encyclopedia of Polymeric Nanomaterials, 2015.

[128] J. Israelachvili, The Different Faces of Poly(Ethylene Glycol), Proc. Natl. Acad. Sci. U. S. A. 94 (1997) 8378–8379.

[129] Q. Wang, L. Li, S. Jiang, Effects of a PPO-PEO-PPO Triblock Copolymer on Micellization and Gelation of a PEO-PPO-PEO Triblock Copolymer in Aqueous Solution, Langmuir. 21 (2005) 9068–9075.

[130] R. Kunii, H. Onishi, Y. Machida, Preparation and Antitumor Characteristics of PLA/(PEG-PPG-PEG) Nanoparticles Loaded with Camptothecin, Eur. J. Pharm. Biopharm. 67 (2007) 9–17.

[131] J.W. Gallaway, A.C. West, PEG, PPG, and Their Triblock Copolymers as Suppressors in Copper Electroplating, J. Electrochem. Soc. 155 (2008) D632.

[132] M.D.M. Castro López, S. Dopico García, A. Ares Pernas, J.M. López Vilariño, M.V. González Rodríguez, Effect of PPG-PEG-PPG on the Tocopherol-Controlled Release from Films Intended for Food-Packaging Applications, J. Agric. Food Chem. 60 (2012) 8163–8170.

[133] Nature Structural Biology, www.wwpdb.org, (2003).

[134] Protein Data Bank, www.rcsb.org.

[135] E.J. Sundberg, M. Urrutia, B.C. Braden, J. Isern, R.A. Mariuzza, Estimation of the Hydrophobic Effect in an Antigen-Antibody Protein-Protein Interface, Biochemistry. 39 (2000) 15375–15387.

[136] A. Bujacz, K. Zielinski, B. Sekula, Structural Studies of Bovine, Equine, and Leporine Serum Albumin Complexes with Naproxen, Proteins. 82 (2014) 2199–2208.

[137] J. Soman, J.S. Olson, Structure of the Human Hemoglobin Mutant Hb Providence (A-Gly-C:V1M; B,D:V1M,K82D; Ferrous, carbonmonoxy bound), Doi.org.

[138] A.S. Rose, P.W. Hildebrand, NGL Viewer: A Web Application for Molecular Visualization, Nucleic Acids Res. 43 (2015) W576–W579.

[139] A.S. Rose, A.R. Bradley, Y. Valasatava, J.M. Duarte, A. Prlić, P.W. Rose, Web-Based Molecular Graphics for Large Complexes, Proc. 21st Int. Conf. Web3D Technol. - Web3D '16. (2016) 185–186.

[140] P.W. Rose, A. Prlić, A. Altunkaya, C. Bi, A.R. Bradley, C.H. Christie, et al., The RCSB protein data bank: integrative view of protein, gene and 3D structural information., Nucleic Acids Res. (2016).

[141] H.M. Berman, J. Westbrook, Z. Feng, G. Gilliland, T.N. Bhat, H. Weissig, I.N. Shindyalov, P.E. Bourne, The Protein Data Bank Nucleic Acids Research, Nucleic Acids Res. (2000).

[142] http://biophysics.cs.vt.edu/H++.

[143] R. Anandakrishnan, B. Aguilar, A. V. Onufriev, H++ 3.0: Automating pK Prediction and the Preparation of Biomolecular Structures for Atomistic Molecular Modeling and Simulations, Nucleic Acids Res. 40 (2012) 537–541.

[144] P. Rezácová, D. Borek, S.F. Moy, A. Joachimiak, Z. Otwinowski, Crystal Structure and Putative Function of Small Toprim Domain-Containing Protein from Bacillus Stearothermophilus., Proteins. 70 (2008) 311–319.

[145] J.C. Gordon, J.B. Myers, T. Folta, V. Shoja, L.S. Heath, A. Onufriev, H++: A Server for Estimating pK_as and Adding Missing Hydrogens to Macromolecules, Nucleic Acids Res. 33 (2005) 368–371.

[146] Y. Cheng, C. Xu, P.K. Shen, S.P. Jiang, Effect of Nitrogen-Containing Functionalization on the Electrocatalytic Activity of PtRu Nanoparticles Supported on Carbon Nanotubes for Direct Methanol Fuel Cells, Appl. Catal. B Environ. 158–159 (2014) 140–149.

[147] A. Picker, Influence of Polymers on Nucleation and Assembly of Calcium Silicate Hydrates, (2013).

[148] X. Xu, Y. Zhao, Q. Lai, Y. Hao, Effect of Polyethylene Glycol on Phase and Morphology of Calcium Carbonate, J. Appl. Polym. Sci. 119 (2011) 319–324.

[149] S.C. Moldoveanu, V. David, Sample Preparation in Chromatography, 2002.

[150] L.C. Bonkovoski, A.F. Martins, I.C. Bellettini, F.P. Garcia, C. V. Nakamura, A.F. Rubira, E.C. Muniz, Polyelectrolyte Complexes of Poly[(2-Dimethylamino) Ethyl Methacrylate]/Chondroitin Sulfate Obtained at Different pHs: I. Preparation, Characterization, Cytotoxicity and Controlled Release of Chondroitin Sulfate, Int. J. Pharm. 477 (2014) 197–207.

[151] L.J. Kirwan, P.D. Fawell, W. Van Bronswijk, In Situ FTIR-ATR Examination of Poly(Acrylic Acid) Adsorbed onto Hematite at Low pH, Langmuir. 19 (2003) 5802–5807.

[152] L.T. Boni, T.P. Stewart, J.L. Alderfer, S.W. Hui, Lipid-Polyethylene Glycol Interactions: I. Induction of Fusion Between Liposomes, J. Membr. Biol. 62 (1981) 65–70.

[153] J.J. Beaudoin, R. Feldman, Dependence of Degree of Silica Polymerization and Intrinsic Mechanical Properties of C-S-H on C/S, in: 8th Int. Congr. Chem. Cem., Rio de Janeiro, 1986.

[154] G. Constantinides, F.J. Ulm, The Effect of Two Types of C-S-H on the Elasticity of Cement-Based Materials: Results from Nanoindentation and Micromechanical Modeling, Cem. Concr. Res. 34 (2004) 67–80.

[155] J.J. Kim, E.M. Foley, M.M. Reda Taha, Nano-Mechanical Characterization of Synthetic Calcium-Silicate-Hydrate (C-S-H) with Varying CaO/SiO$_2$ Mixture Ratios, in: Cem. Concr. Compos., 2013: pp. 65–70.

[156] T.E. Creighton, Protein Folding, Biochem. J. 270 (1990) 1–16.

[157] A. Brüning, J. Jückstock, Misfolded Proteins: From Little Villains to Little Helpers in the Fight Against Cancer, Front. Oncol. 5 (2015).

[158] C. Nick Pace, J. Martin Scholtz, G.R. Grimsley, Forces Stabilizing Proteins, FEBS Lett. 588 (2014) 2177–2184.

[159] G.J. Lesser, G.D. Rose, Hydrophobicity of Amino Acid Subgroups in Proteins, Proteins Struct. Funct. Bioinforma. 8 (1990) 6–13.

[160] Y. Yan, D. Seeman, B. Zheng, E. Kizilay, Y. Xu, P.L. Dubin, PH-Dependent Aggregation and Disaggregation of Native β-Lactoglobulin in Low Salt, Langmuir. 29 (2013) 4584–4593.

[161] E. Pinho Melo, M.R. Aires-Barros, S.M.B. Costa, J.M.S. Cabral, Thermal Unfolding of Proteins at High pH Range Studied by UV Absorbance, J. Biochem. Biophys. Methods. 34 (1997) 45–59.

[162] S. V Patwardhan, G. Patwardhan, C.C. Perry, Interactions of Biomolecules with Inorganic Materials: Principles, Applications and Future Prospects, J. Mater. Chem. 17 (2007) 2875–2884.

[163] S.K. Ramakrishnan, J. Zhu, C. Gergely, Organic-Inorganic Interface Simulation for New Material Discoveries, Wiley Interdiscip. Rev. Comput. Mol. Sci. 7 (2017).

[164] M. Yáñez, J. Gil-Longo, M. Campos-Toimil, Calcium Binding Proteins, Adv. Exp. Med. Biol. 740 (2012) 461–482.

[165] S. Venkataramani, J. Truntzer, D.R. Coleman, Thermal Stability of High Concentration Lysozyme across Varying pH: A Fourier Transform Infrared Study, J. Pharm. BioAllied Sci. 5.2 (2013) 148–153.

[166] E. Calabrò, S. Magazù, Unfolding-Induced in Haemoglobin by Exposure to Electromagnetic Fields: A FTIR Spectroscopy Study, Orient. J. Chem. 30 (2014) 31–35.

[167] P. Mondai, S.R. Shah, L.D. Marks, Nanoscale Characterization of Cementitious Materials, ACI Mater. J. 105 (2008) 174–179.

[168] J. Wu, Y.J. Zhu, S.W. Cao, F. Chen, Hierachically Nanostructured Mesoporous Spheres of Calcium Silicate Hydrate: Surfactant-Free Sonochemical Synthesis and Drug-Delivery System with Ultrahigh Drug-Loading Capacity, Adv. Mater. 22 (2010) 749–753.

[169] V. Morales-Florez, N. De La Rosa-Fox, Structure of Supercritically Dried Calcium Silicate Hydrates (C-S-H) and Structural Changes Induced by Weathering, J. Mater. Sci. 48 (2013) 5022–5028.

[170] V. Morales-Florez, F. Brunet, Structural Models of Random Packing of Spheres Extended to Bricks: Simulation of the Nanoporous Calcium Silicate Hydrates, Mol. Simul. 35 (2009) 1001–1006.

[171] S. Mazumder, D. Sen, R. Loidl, H. Rauch, Dynamical Scaling and Isotope Effect in Temporal Evolution of Mesoscopic Structure During Hydration of Cement, Phys. Rev. B - Condens. Matter Mater. Phys. 84 (2011) 1–10.

[172] H. Manzano, A. Ayuela, J.S. Dolado, On the Formation of Cementitious C-S-H Nanoparticles, in: J. Comput. Mater. Des., 2007: pp. 45–51.

[173] R. Blinc, G. Lahajnar, S. Umer, M.M. Pintar, NMR Study of the Time Evolution of the Fractal Geometry of Cement Gels, Phys. Rev. B. 38 (1988) 2873–2875.

[174] E.M. Foley, J.J. Kim, M.M. Reda Taha, Synthesis and Nano-Mechanical Characterization of Calcium-Silicate-Hydrate (C-S-H) Made with 1.5 CaO/SiO_2 Mixture, Cem. Concr. Res. 42 (2012) 1225–1232.

[175] M. Delhorme, C. Labbez, M. Turesson, E. Lesniewska, C.E. Woodward, B. Jönsson, Aggregation of Calcium Silicate Hydrate Nanoplatelets, Langmuir. 32 (2016) 2058–2066.

[176] C. Plassard, E. Lesniewska, I. Pochard, A. Nonat, Investigation of the Surface Structure and Elastic Properties of Calcium Silicate Hydrates at the Nanoscale, Ultramicroscopy. 100 (2004) 331–338.

[177] S. Grangeon, F. Claret, C. Roosz, T. Sato, S. Gaboreau, Y. Linard, Structure of Nanocrystalline Calcium Silicate Hydrates: Insights from X-Ray Diffraction, Synchrotron X-Ray Absorption and Nuclear Magnetic Resonance, J. Appl. Crystallogr. 49 (2016) 771–783.

[178] V.R.G. Dev, J.R. Venugopal, M. Senthilkumar, D. Gupta, S. Ramakrishna, Prediction of Water Retention Capacity of Hydrolysed Electrospun Polyacrylonitrile Fibers Using Statistical Model and Artificial Neural Network, J. Appl. Polym. Sci. 113 (2013) 3397–3405.

[179] J. Zhang, Z. Lu, M. Wu, Q. Wu, J. Yang, Facile Fabrication of Poly(Acrylic Acid) Hollow Nanogels via In Situ Pickering Miniemulsion Polymerization, Polym. Chem. 6 (2015) 6125–6128.

[180] S.S. Shiratori, M.F. Rubner, PH-Dependent Thickness Behavior of Sequentially Adsorbed Layers of Weak Polyelectrolytes, Macromolecules. 33 (2000) 4213–4219.

[181] H. Matsuyama, J.F. Young, Effects of pH on Precipitation of Quasi-Crystalline Calcium Silicate Hydrate in Aqueous Solution, Adv. Cem. Res. 12 (2000) 29–33.

[182] A. Nonat, The structure and stoichiometry of C-S-H, Cem. Concr. Res. 34 (2004) 1521–1528.

[183] F. Pelisser, P. Jean, P. Gleize, A. Mikowski, Effect of the Ca/Si Molar Ratio on the Micro/Nanomechanical Properties of Synthetic C-S-H Measured by Nanoindentation, J. Phys. Chem. C. 116 (2012) 17219–17227.

[184] G.W. Milton, The Theory of Composites, 2002.

[185] W.G. Jiang, J.J. Su, X.Q. Feng, Effect of Surface Roughness on Nanoindentation Test of Thin Films, Eng. Fract. Mech. 75 (2008) 4965–4972.

[186] C. Pichler, R. Lackner, Identification of logarithmic-type creep of calcium-silicate-hydrates by means of nanoindentation, Strain. 45 (2009) 17–25.

Appendix

Statistical testing

The mean and standard deviation of the control samples including two replicates were measured. A confidence interval of 95% was chosen to detect the values significantly different with the control measurement.

Significantly different values are highlighted:

	C/S = 0.7	C/S = 1.5
	d (Å)	d (Å)
PEG-PPG-PEG1900	13.8	14.8
PEG-PPG-PEG8000	13.6	14.3
PEG-PPG-PEG16000	13.6	13.6
PPG-PEG-PPG	14.1	13.6
Aminopropyl PPG-PEG-PPG	14.8	13.6
PVP-DMEMA	14.1	14.5
Arginine	13.8	14.3
Glutamine	14.1	13.8
Leucine	13.6	14.1
Glutamic acid	13.4	13.8
Lysozyme	13.8	14.3
Albumin	13.8	13.6
Hemoglobin	13.4	13.6

Table A.1 Significantly different values compared to the control sample determined by statistical testing on the XRD results.

	C/S = 0.7	C/S = 1.5
	Q^2/Q^1	Q^2/Q^1
PEG-PPG-PEG1900	3.86	3.83
PEG-PPG-PEG8000	3.99	3.86
PEG-PPG-PEG16000	3.83	3.78
PPG-PEG-PPG	3.91	3.89
Aminopropyl PPG-PEG-PPG	3.85	3.78
PVP-DMEMA	3.98	3.73
Arginine	3.55	3.51
Glutamine	3.77	3.42
Leucine	3.85	3.41
Glutamic acid	3.57	3.46
Lysozyme	3.59	3.62
Albumin	3.7	3.68
Hemoglobin	3.41	3.44

Table A.2 Significantly different values compared to the control sample determined by statistical testing on the FTIR results.